Bone Marrow Aspirate Concentrate in Bone Healing: An Analysis of Basic Science Evidence

A Gianakos, A Ni, L Zambrana, J Moya-Angeler, JG Kennedy, JM Lane

Hospital for Special Surgery, New York, NY 10021

INTRODUCTION: Long bone fractures that fail to heal or show a delay in healing can lead to increased morbidity [1]. Bone marrow aspirate concentrate (BMAC) and bone mesenchymal stem cells (BMSCs) have been suggested as an autologous biologic to use to aid long bone healing. The purpose of this study was to systematically review the basic science in vivo evidence for the use of BMAC and BMSCs in the treatment of pathologic processes of bone.

METHODS: PubMed/MEDLINE and EMBASE databases were screened in July 2014 using the following search criteria: (("bmac" OR "bone marrow aspirate concentrate" OR "bmc" OR "bone marrow concentrate" OR "mesenchymal stem cells") AND ("bone" OR "osteogenesis" OR "fracture healing" OR "nonunion" OR "delayed union")). Only basic science in vivo studies examining the effects of BMAC/BMSCs on long bone were included. Data was then extracted and studies were analyzed for trends.

RESULTS: The search yielded 35 articles for inclusion. 88% reported cell concentrations. 100% showed significant increase in bone formation in the BMAC/BMSC group on radiograph. 90% reported significant improvement in earlier bone healing on histologic / histomorphometric assessment. 81% reported a significant increase in bone area on micro-computed tomography. 78% showed a higher torsional stiffness for the BMAC/BMSC treated defects.

Fig. 2: Histologic/Histomorphometric Outcomes

DISCUSSION & CONCLUSION: In the in vivo studies evaluated, BMAC/BMSCs confer beneficial effects on the healing of long bone models when compared with a control. Radiograph, micro-computed tomography, histologic, histomorphometric, and biomechanical analysis have all demonstrated improved bone regeneration in groups treated with BMAC/BMSCs. Proof of concept has been established for BMAC/BMSCs in the treatment of bone defects as both a primary treatment strategy and an adjunct. Randomized clinical trials are warranted to establish this beneficial effect in a clinical setting. Further standardization of the composition of BMAC is encouraged in order to allow for more accurate reporting of results.

Fig. 1: Radiographic Outcomes

Percutaneous Bone Marrow Aspirate, Scaffolds, and Autografts for Spinal Arthrodesis: a Review of Current Research

AY Ni[1], A Ambrosino[1], A Gianakos[1], L Zambrana[2], J Lane[1, 2]

[1]Hospital for Special Surgery, New York, NY. [2] Weill Cornell Medical School, New York, NY

INTRODUCTION: In 2012 spinal fusion was one of the five most common procedures performed in the operating room [1]. With over 450,900 spinal fusions performed annually, efforts to cut costs and minimize co-morbidities must be found[1]. While the autologous iliac crest bone graft (ICBG) is considered the "gold standard" graft material, new and safer therapies are emerging. ICBGs have been associated with site morbidity and chronic pain, increased operative time, and blood loss [2]. Up to 5.8% of donor sites experience major complications, such as deep infections and nerve injuries, and 10% experience minor complications [2]. Previous studies have proposed that an osteoconductive substitute with either osteoinductive or osteogenic properties can provide equivalent or better rates of fusion compared with ICBG [3]. Bone marrow aspirate concentrate (BMAC) contains mesenchymal stem cells that have demonstrated osteoblast proliferation potential. This systematic review of the literature compares the outcomes of using BMAC, ICBG, BMAC with scaffolds, or only scaffold to enhance the rate of spine fusion. We posed 2 questions: 1) Is BMAC comparable in efficacy to ICBG? 2) Does BMAC enhance the efficacy of scaffolds during spine fusion?

METHODS: Two authors independently conducted systematic searches in both PubMed/Medline and EMBASE using the following search terms in October 2014: (("bmac" OR "bone marrow aspirate concentrate" OR "bmc" OR "bone marrow concentrate" OR "msc" OR "mesenchymal stem cell" OR "bone mesenchymal stem cell" OR "bmsc") AND ("spine" OR "spine fusion" OR "vertebra" OR "lumbar" OR "thoracolumbar" OR "thoracic" OR "cervical")). Inclusion criteria included animal studies with randomized controls written in the English language and published in peer reviewed journals. Statistics were calculated using StatView and reviewed by four different authors.

RESULTS: After database search and full text review, 30 studies were identified which fit inclusion and exclusion criteria. We examined spine fusion rates determined by radiograph or manual palpation. Other methods of determining fusion, such as CT or histology, were not consistent across the 30 studies, as randomized animal trials using BMAC for spine fusions are rare and not uniform in their methodology.

Table 1. Results of the spine fusion rates.

N-total Articles included for analysis	BMAC vs. ICBG	Scaffold+BMAC vs. Scaffold
Radiographic	5	6
Manual Palpation	8	10

Percutaneous BMAC and ICBG demonstrated comparable spine fusion rate efficacy, with both radiographic and manual palpation analysis (p>0.05). Both radiographic and manual palpation analysis for fusion demonstrated improved spine fusion rates when BMAC was used adjunctively with a scaffold when compared to scaffold alone (p<0.001). By radiograph, BMAC with scaffolds demonstrated a rate of fusion of 62.5%, while scaffold alone was 15.0% (p<0.001). Manual palpation analysis showed a fusion rate of 68.7% for scaffold plus BMAC while scaffold alone showed a 16.7% fusion rate (p<0.001)

DISCUSSION & CONCLUSIONS: Our systematic review suggests that using BMAC as an ICBG alternative can yield comparable fusion rates. Our findings also demonstrate that utilizing BMAC with a scaffold will significantly enhance the rate of fusion, regardless of the scaffold type. Further high-quality comparative controlled human trials should be conducted, as well as comparing the rates of fusion between BMAC with scaffolds to ICBG.

Injectable, cohesive and toughened blood composite calcium phosphate cement for spine fusion: an *in vivo* model developed in sheep

C Mellier[1, 3], H Gonçalves[2], M Dutilleul[2], P Pilet[2], P Janvier[1], B Bujoli[1], O Gauthier[2], J-M Bouler[1]

[1]*CEISAM, Université de Nantes CNRS UMR 6230, BP 92208, 44322 Nantes Cedex 3, France*
[2]*LIOAD, Université de Nantes, INSERM UMR 791, BP 84215, 44042 Nantes Cedex 1, France*
[3]*Graftys SA, 415 rue Claude Nicolas Ledoux, 13854 Aix en Provence Cedex 3, France*

INTRODUCTION: Conventional calcium phosphate cements (CPCs) are stiff and fragile materials and most of them do not present a porous microstructure able to stimulate volume cell colonization significantly [1]. These drawbacks limit surgical use of CPCs to small volume and non-load bearing applications. In order to decrease its stiffness, fibrin, obtained from blood clot, has been considered as a resorbable polymer that could be added to an apatitic CPC formulation. The purpose of this study was to compare both handling and mechanical properties of a given CPC formulation with another one where the liquid component was replaced by fresh blood. As a recent study has shown that blood clot could also improve bioactivity of calcium phosphates [2], in vivo resorption and osteoconduction of the resulting cements were also studied in a spinal application.

MATERIALS & METHODS: CPC powder formulation containing mainly α-TCP was studied. The used liquid phases were either a 0.5% Na2HPO4 solution or blood freshly taken from sheep with a unique L/P ratio of 0.45. Three different parameters were compared: setting time (using Gilmore's needle apparatus), injectability and compressive strength. Eventually, an in vivo study was conducted in sheep to evaluate the capacity of the two cements in promoting spine fusion (intersomatic cages). Both osteoconduction and material resorption were quantified through 2D-SEM and 3D-μ-CT image analyses.

RESULTS: For blood composite cement, both adhesion properties and time of workability were significantly increased. Compressive strength tests showed a typical ductile material behaviour (Fig. 1). After 12 weeks of implantation the blood composite cement (i) showed a better resorption rate (+22%); (ii) conducted a larger amount of new bone formation (+18%) as illustrated on Fig. 2. Quality of newly formed bone is very similar for both tested CPCs with an excellent bone/implant osteocoalescent interface.
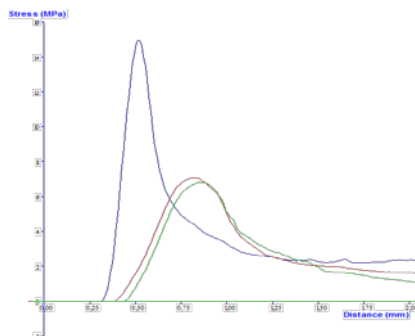
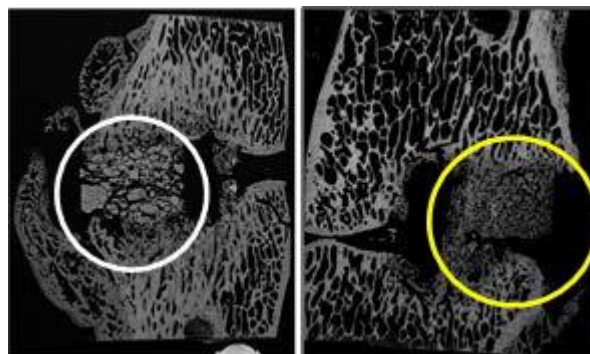*Fig.1: Comparative compressive strength for control CPC (blue) and blood/CPC(red and green)*

Fig.2: SEM micrographs comparing evolution of spine fusion rate at 3 month p.o. (CPC on the left, blood composite on the right).

DISCUSSION & CONCLUSIONS: This study showed that replacing the liquid component by blood in this specific apatitic CPC can modulate handling (workability, adhesion), mechanical (stiffness, plasticity) and biological (resorption rate) properties. These modifications, useful for the targeted spinal application, are mainly due to the blood clot formation that interacts with the setting reaction and modifies the cement apatitic microcrystalline structure.

Sr-HA Injectable Cement for Spinal Fracture: The development and clinical applications

W Lu

Dept. of Orthopaedics, The University of Hong Kong & SIAT, Chinese Academy of Sciences, PR China

INTRODUCTION: No matter what the source, injectable biomaterials must meet several criteria to perform successfully in clinical applications. They must be biocompatible, or able to function *in vivo* without eliciting an intolerable response in the body either locally or systemically. Adequate mechanical properties are also an important criterion for biomaterials, especially those used in devices intended to replace or reinforce load-bearing skeletal structures. The aim of this study was to clinically compare the properties of strontium-containing bioactive bone cement with those of polymethylmethacrylate (PMMA) bone cement [1, 2].

METHODS: Strontium-containing hydroxyapatite (Sr-HA) bioactive bone cement consists of a filler blend of strontium- containing hydroxyapatite and a resin blend of bisphenol A diglycidylether methacrylate, triethylene glycol dimethacrylate, poly(ethylene glycol) methacrylate, and N, N-dimethyl-p-toluidine [1]. Its properties, including setting temperature, mechanical strength, biocompatibility as well as osseoinduction, were compared with other cements *in vitro* and *in vivo*, followed with a pilot study of clinical trial.

RESULTS: The Sr-HA cement had a setting time of 15 to 18 minutes and a maximum setting temperature of 58 °C. Results from a cell biocompatibility test indicated that the new bioactive bone cement was favorable for cell growth. Sr-HA cement promoted osteoblast attachment and mineralization *in vitro* and bone growth and osseointegration *in vivo*. Spinal stiffness significantly decreased after fracture (47.5% of intact condition). Instant stiffness of the spine recovered to 107.8% of the intact condition after bone cement injection. After 3,000 and 20,000 cycles of fatigue loading, stiffness of the cemented spine was found to be 93.5% and 94.4% of intact stiffness, respectively. The Sr-HA cement had a compressive strength of 40.9 MPa, and a bending strength of 31.3 MPa. The bending strength and modulus were closer to the one of human cancellous bone. The clinical pilot study (Fig 1) was conducted in two hospitals in PR China, 23 cases of osteoporotic fractures treated with this cement with a mean follow-up of 18 months. Results suggested that Sr-HA cement was as effective as PMMA in relieving pain.
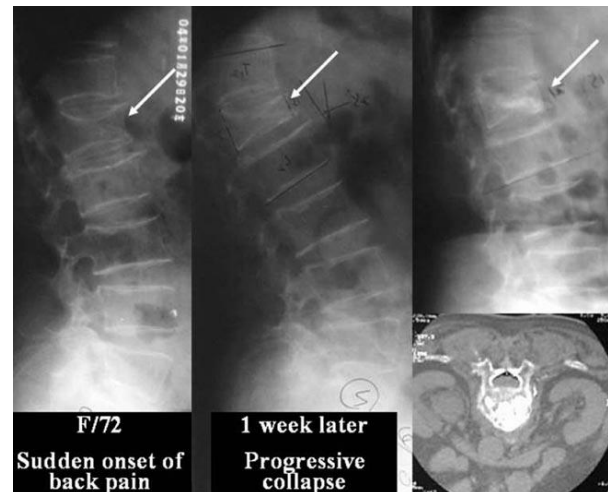

Fig. 1: Lat radiographs of an old woman with an osteoporotic fracture of Spine (left), with progressive collapse over one week (middle), and pain. Vertebroplasty was performed and X-ray of 6 months postsurgery showing maintenance of disc height and good placement of the cement (right)

DISCUSSION & CONCLUSIONS: Oral strontium has shown to induce new bone formation and seems effective in reducing fracture risk in osteoporosis. This study suggests that strontium delivered locally has the same effect; thus, the combination of strontium with HA in a biomaterial or cement with a low setting temperature, adequate stiffness, and low viscosity makes this a good bioactive cement for vertebroplasty. The Cement may be used in other clinical applications such as hip fractures, plastic surgery and dentistry.

Radiological Research disc behavior after fracture of the thoracolumbar junction compression treated by kyphoplasty: about a series of 52 cases

S Teyssédou[1], M Saget[1], C Brèque[2], LE Gayet[1], P Rigoard[3], P Pries[1], T Vendeuvre[1]

[1] *Department of Orthopaedic Surgery and Traumatology, CHU of Poitiers, France.*
[2] *Laboratory of Anatomy, Faculty of Medicine and Pharmacy, University of Poitiers, France.*
[3] *N3Lab, CHU of Poitiers, France.*

INTRODUCTION: The advantage of kyphoplasty for sustainable correction of traumatic spinal deformity after a fracture type A Magerl is now proved. However, the behavior of adjacent discs to the fractured vertebra after this procedure is little known. The aim of our work is to analyze their evolution according to various parameters, including the importance of the initial comminution and the quality of the reduction of traumatic deformity.

METHODS: We conducted a prospective, single-center study. The primary inclusion criterion is a single fracture and compression of the thoracolumbar junction treated with kyphoplasty balloons (Kyphon) with acrylic cement. We measured on radiographs [1] the traumatic spinal kyphosis (CV) [2] and then the angle disc (AD) and height index (DHI) of adjacent discs (Fig. 1). A linear regression was performed to examine the link IHD between the upper disk (IHDsup), postoperative CV and its correction gain. The various parameters were compared using the Wilcoxon test Man Whitney paired.

RESULTS: 52 patients were included. The average follow-up was 18.6 months and the mean age at surgery was 44.8 years. Of all the series, traumatic spinal kyphosis decreased from 13.9° before treatment to 8.2 ° at final follow. The study of IHD found significant subsidence upper disc ($p = 0.0004$) and non-significant lower disc ($p = 0.116$). Angulation disc had a significant decrease in the lordosis of the upper disc ($p = 4 \times 10^{-5}$). There is a correlation between the loss of height of the upper disk (IHDsup) and the quality of the reduction of traumatic spinal deformity. Preoperative CV does not affect the degeneration of adjacent discs.

DISCUSSION & CONCLUSIONS: This study highlights the need for a good correction of traumatic spinal deformity to prevent sagging and loss of mechanical function of the upper disc. The underlying disk fracture offsets the residual spinal deformity. Our work confirms that balloon kyphoplasty is of interest [3] in the treatment of compression fractures. It allows a significant and sustainable reduction of traumatic spinal deformity while leaving the healthy adjacent discs free.
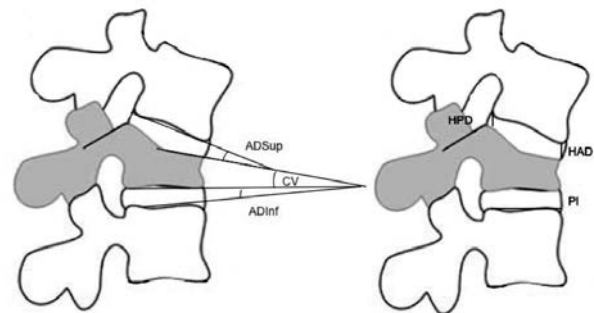

Fig. 1: Every measure pre and post surgery.

Platelet-Rich Plasma in the Long Bone Model: An Analysis of Basic Science Evidence

A Gianakos, L Zambrana, I Savage-Elliott, JM Lane, JG Kennedy

Hospital for Special Surgery, New York, NY 10021

INTRODUCTION: Long bone fractures that fail to heal can lead to increased patient morbidity. There has been a need to develop therapeutic strategies to improve bone healing to prevent nonunion and delayed union [1]. Platelet-rich plasma (PRP) is an autologous biologic that has been suggested as an adjunct to aid long bone healing. The purpose of this study was to systematically review the basic science in vivo evidence for the use of platelet-rich plasma (PRP) in the treatment of pathologic processes of bone. This will determine whether a proof of concept for its use has been established to facilitate further investigation at a clinical level.

METHODS: The PubMed/MEDLINE and EMBASE databases were screened in June 2014 using the following search criteria: "(Platelet-rich plasma OR prp OR autologous conditioned plasma OR acp) AND (bone OR osteocytes OR osteogenesis OR nonunion OR delayed union)". Only basic science in vivo studies examining the effects of PRP on long bone were included. Data was then extracted with a standardized table that included PRP preparation and cytology, type of species, number of animals, type of bone used, size of bone defect, groups compared, time periods analysed, type of evaluation, and results. Studies were analysed for trends.

RESULTS: The search yielded 29 articles for inclusion. 72% of the studies reported platelet concentrations. 89% of studies reported significant improvement in earlier bone healing on histologic/histomorphometric assessment. 100% showed significant increase in bone formation in the PRP group on radiograph. 80% of studies reported a significant increase in bone area on micro-computed tomography. 100% of studies showed a higher torsional stiffness for the PRP-treated defects.

Fig. 1: Histologic/Histomorphometric Outcomes

Fig. 2: Radiographic Outcomes

DISCUSSION & CONCLUSIONS: In the in vivo studies evaluated, PRP confers several potential beneficial effects on long bone models when compared with a control. The literature is inconsistent with regard to reporting the methods of preparation of PRP and the platelet concentration. The literature also lacks standardization in the analysis of bone healing between different modalities as well as within each modality.Proof of concept for PRP as a biologic adjunct in long bone models has been determined. Further clinical trials will be required to determine whether this effect can be translated to a beneficial clinical outcome.

Table 1. Evaluation of Outcomes

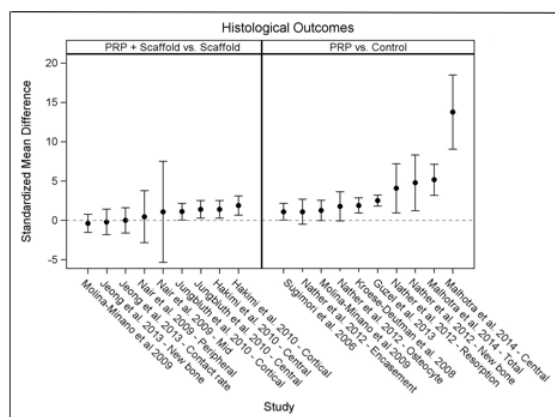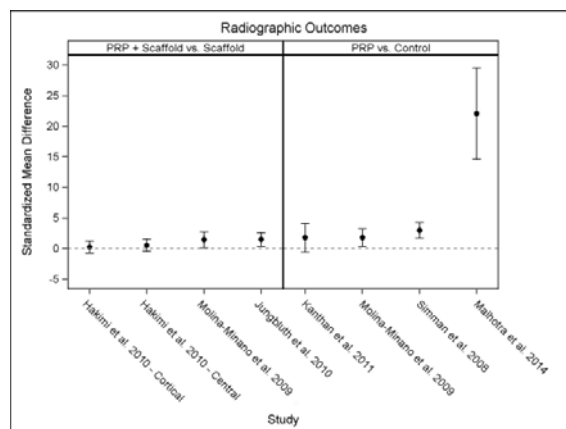| Outcome	Significant Increase (No.)	Improvement with no statistics (No.)	No Significant Change (No.)
Radiographic	6	6	2
MCT	4	1	1
Histologic/Histomorphometric	16	9	4
Biomechanical	5	1	0
Bone Mineral Density	3	0	1
Gross	1	2	0
Scintigraphy	1	0	0
Radionuclide	1	0	0
Bone Ingrowth Depth	1	0	0
Osteoblast shape/density	1	0	0

Percutaneous Interventional Radiologic Management of Large Bone Metastases to the pelvis

PI Mallinson, TJ Tan, TM Coupal, HA Ouellette, PW Clarkson, PL Munk

University of British Columbia and Vancouver General Hospital, Vancouver, British Columbia, Canada (PIM, PLM, HO, TJT, TMC – Radiology, PWC – Orthopedic Surgery)

INTRODUCTION: Management of pelvic metastases can be extremely difficult, as once lesions become large (greater than 5 cm), patients become markedly symptomatic, yet surgical excision carries significant morbidity. Although radiotherapy is sometimes helpful in alleviation of pain at rest, lack of structural integrity caused by tumour destruction makes weight bearing difficult in most circumstances [1, 2].

METHODS: We reviewed our experience in treating patients with large pelvic metastases in 2011-14. A total of 28 patients were identified who were treated with cementation and/or thermal ablation. Of these, 23 patients received both cementation and thermal ablation, (usually cryoablation), 3 patients were treated with cementation alone, and 2 with cryoablation alone. Patients were scored on a scale of ten for pain 1 week before, immediately after and one week to 1 month after the procedure.

RESULTS: In most instances, it was not possible to ablate the entire lesion; however, particular attention was paid to the weight bearing portions of the lesion usually the acetabulum. In spite of the fact that large portions of tumour were left untreated, 82% of patients had demonstrated marked improvement in pain at rest and 75% of patients noted marked improvement in pain (minimum of three point improvement in pain score) on ambulation and improvement in mobility. No complications were encountered.

DISCUSION & CONCLUSIONS: Our experience would indicate that even patients with large lesions (in our series, measuring up to 15 cm in largest dimension) can benefit from percutaneous palliative procedures, thereby significantly improving quality of life. These patients should not be dismissed as having disease too advanced to benefit from this type of interventional radiologic technique.

Pre- and post-implantation alignment of µCT data of β-TCP scaffolds

A Sweedy[1], M Bohner[2], GH van Lenthe[3], S Becker[4], G Baroud[1]

[1]*Laboratoire de Biomécanique, Université de Sherbrooke, Canada.*[2]*RMS Foundation, Switzerland,*
[3]*Division of Biomechanics, Mechanical Engineering, K.U. Leuven, Belgium.* [4]*IMSART, Austria.*

INTRODUCTION: The better understanding of the biological processes and interactions inside resorbable CaP scaffolds can lead to better design of the scaffolds. Pre-implantation characterizing the resorbable CaP scaffolds using µCT provides 3D quantitative description of the scaffolds. These global characterization information provided a base for evaluation of in vivo explanted samples [1, 2]. The alignment of pre- and post-implantation µCT data can provide extensive localized information about the biological processes interactions. Such information can help explaining the interactions between scaffold morphological properties, bone deposition and scaffold resorption. However, the alignment is a challenging process due to the fast and non-uniform nature of resorption in β-TCP scaffolds. Therefore, the aim of this study is to develop a method to align pre- and post-implantation 3D µCT data of β-TCP scaffolds.

METHODS: The alignment algorithm is applied to the segmented pre- and post-implantation µCT images stacks. Specifically, the algorithm aligns the pre-implantation scaffold (white in Fig. 1 (a)) with scaffold remains (red in Fig. 1 (b)) in post-implantation µCT. The algorithm comprises the following steps. First, we manually determine the 6 degrees of freedom of 3D transform for aligning the pre- and post-implantation data. This 3D transform is applied to the pre-implantation images stack to have approximately aligned stacks of images. Second, we use speed up robust feature (SURF) algorithm [3] to find the matching features in both pre- and post-implantation corresponding images (Fig.1 (c)) marked by (+) and (o) respectively. Third, the features in corresponding images are matched and sorted based on the strongest match. Fourth, the strongest features are used for calculation of the 2D geometrical transform (Eq. 1). The 2D geometrical transform of this step includes fine calculation of rotation angle around implant axis θ_z and displacement in x and y directions, Δx and Δy respectively.

$$\begin{bmatrix} x' \\ y' \\ 1 \end{bmatrix} = \begin{bmatrix} \cos(\theta_z) & -\sin(\theta_z) & \Delta x \\ \sin(\theta_z) & \cos(\theta_z) & \Delta y \\ 0 & 0 & 1 \end{bmatrix} \begin{bmatrix} x \\ y \\ 1 \end{bmatrix} \quad (1)$$

RESULTS: The improved segmented post-implantation data by aligning process is shown in Fig. 1 (d). Specifically, soft tissue is indicated in blue, bone in green, scaffold remains in red, resorbed scaffold in yellow and scaffold replaced by bone in black.
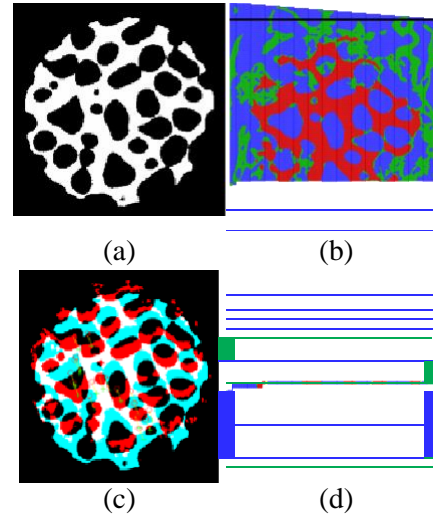

(a) (b)

(c) (d)

Fig. 1: Aligned pre- and post-implantation scans

DISCUSSION & CONCLUSIONS: The presented new method uses SURF features which are invariant of neither scale nor rotation. Therefore, it provides accurate alignment of pre- and post-implantation µCT data. This novel method provides more accurate 3D morphometric analyses of the in vivo explanted resorbable scaffolds. It adds new classification details to the classical ones: bone, scaffold remains and soft tissue. In particular, this is achieved by labelling the pre-implantation voxels in the µCT that was occupied by scaffold material at the implantation time and changed at explantation time. Such a change could be either resorbed or occupied by new bone deposition. By labelling the resorption in 3D µCT data, the novel method opens new door to study local biological interactions in resorbable scaffolds.

Injectable, settable, and space-maintaining composite bone grafts for posterolateral fusion

AD Talley[1], S Shiels[2], KJ Zienkiewicz[1], JC Wenke[2], SA Guelcher[1]

[1] *Department of Chemical and Biomolecular Engineering, Vanderbilt University, Nashville, TN, USA.* [2] *Orthopaedic Task Area, U.S. Army Institute of Surgical Research, San Antonio, TX, USA*

INTRODUCTION: Posterolateral fusion (PLF) is a common procedure for degenerative disc disease. However, PLF presents a number of environmental challenges, including the size of the gap that must be bridged, a limited amount of bony surface area, and graft compression by posterolateral muscle. Consequently, autograft (the current standard of care) can heal unpredictably and inadequately, resulting in unsuccessful fusion. While rhBMP-2 delivered from an absorbable collagen sponge (ACS) has been approved for anterior lumbar interbody fusion, the ACS carrier is not suitable for PLF due to compression by the musculature. Low-viscosity (LV) injectable polyurethane grafts have been reported to be effective carriers for rhBMP-2 and support new bone growth [1]. By reinforcing LV with ceramic particles, its space maintenance properties can be enhanced. Mastergraft (MG) is a biocompatible, biphasic ceramic composed of 85% β-tricalcium phosphate and 15% hydroxyapatite that is similar in mineral content to natural bone [2]. 45S5 Bioglass (BG) is a bioactive, resorbable glass that has been used effectively in a variety of bone regeneration applications [3]. In the present study, we investigated the ability of injectable LV-MG and LV-BG composites to promote new bone formation and fusion in a rabbit PLF model.

METHODS: LV was synthesized from a lysine triisocyanate (LTI)-polyethylene glycol (PEG) prepolymer, a polyester triol 450 (g/mol), and triethylene diamine catalyst. Treatment groups included the LV-45% MG or LV-45% BG with 400 µg/mL (n=3/group). Lyophilized rhBMP-2 was mixed into the graft, and a single-level PLF was performed bilaterally at L5-L6 [4]. The grafts expanded to ~50% porosity and hardened within 7-9 min, at which point the soft tissue was sutured over the defect sites. Animals were sacrificed at 8 weeks, at which time fusion was assessed by palpation, and new bone formation evaluated by radiography, µCT, and histology.

RESULTS: The spines in all animals in each group were fused at 8 weeks. Representative CT images of rabbit spines at 0, 4, and 8 weeks show increasing new bone formation with time (Fig. 1). A representative 3D µCT reconstruction shows a 3–4 mm layer of new bone (yellow arrows) adjacent to the vertebral body, which was more uniform for the MG group. The region far from the vertebral body primarily contained residual MG or BG. As anticipated, MG particles resorbed more slowly than BG particles. Compression of the graft was not observed, and it retained its original thickness after grafting. Histology and histomorphometry are ongoing.
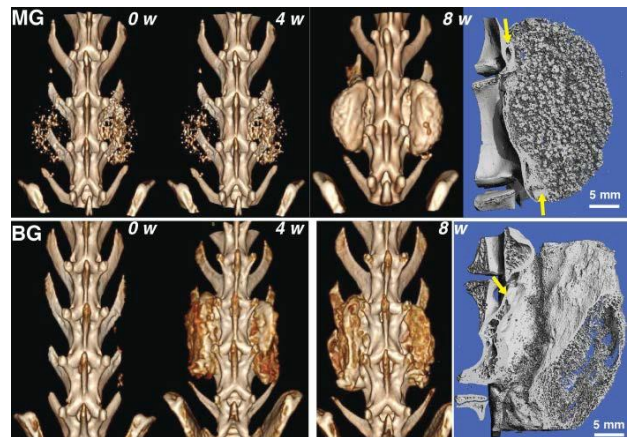

Fig. 1: CT images (left) and 3D µCT reconstructions (right) of a single level PLF performed bilaterally at L5-L6 using MG (top row) or BG (bottom row) LV composites. 3D µCT reconstructions show new bone (yellow arrows) bridging the vertebral processes.

DISCUSSION & CONCLUSIONS: Injectable, settable LV-MG and LV-BG composite bone grafts augmented with rhBMP-2 supported new bone formation and fusion in a rabbit PLF model. The grafts maintained space and resisted compression. In future studies, the grafts will be modified to undergo less volumetric expansion, which is anticipated to improve handling and enhance healing.

Study of the primary load holding on tibial after balloon brings PMMA cement advantage

C Brèque[1], F Khiami[2], LE Gayet[3], JP Faure[1], JP Richer[1], T Vendeuvre[1,3]

[1] *Laboratory of Anatomy, Faculty of Medicine and Pharmacy, University of Poitiers, France.*
[2] *Department of Orthopaedic Surgery and Traumatology, La Salpêtrière, Paris, France.*
[3] *Department of Orthopaedic Surgery and Traumatology, CHU of Poitiers, France.*

INTRODUCTION: In the case of a fractured tibial plateau (Schatzker 2: compression / separation) a new technique based on kyphoplasty, reduces the fracture in a minimally invasive manner [1]. A balloon is used to bring the fractured tibial plateau piece to its anatomical position. The synthesis of the assembly is then carried out with two screws or plate. Our aim is to quantify the mechanical effect of cement injected into the cavity onto the holding of the primary load.

METHODS: With 12 tibial plateau from fresh cadaveric, we formed two groups. Each consisting of 3 men and 3 women (3 left / 3 right). The average age was 78.8 ± 6.2 years for the no cement group and 74.6 ± 11.4 years for the cement group. After having conducted a Schatzker type 2 simulated fracture, we realized the tuberoplasty's technique with a synthesis by screws. Only the cement group received a filling for PMMA. For the samples, we used a compression machine and a knee PUC. The separation space and the pressing-in of the tibial plateau were measured by a stereo system to 3D (Fig. 1). The load on the plate was measured by a load cell.
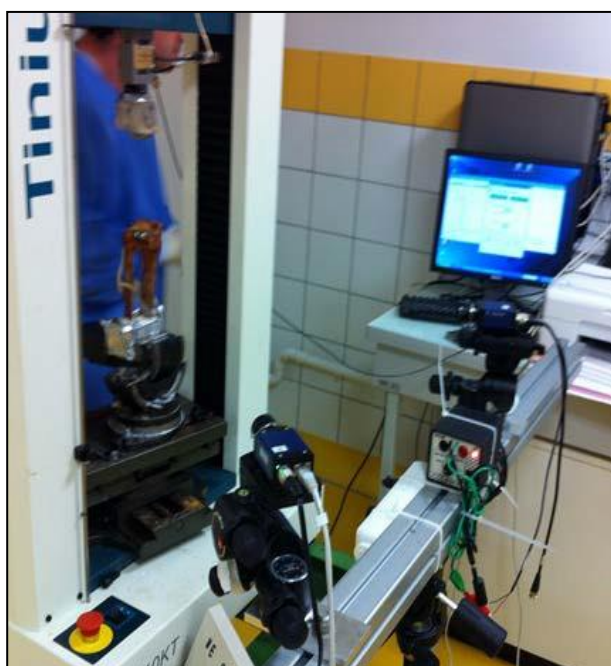
Fig. 1. Compression test.

RESULTS: Using the Wilcoxon matched Man Whitney (Table 1) for the two groups, we compared the maximum load of complete rupture, the force required for the separation distance of 2 mm and the force required for insertion of the plate of 2 mm.

Table 1. Measured loads (N) and Wilcoxon Man Whitney

Force type	Gr. cement	Gr. No cement	p<0.05
Maximal	1695 ± 202	1476 ± 336	0.201
Separation	1518 ± 290	1012 ± 488	0.054
Insertion	364 ± 108	224 ± 113	0.054

DISCUSSION & CONCLUSIONS: There is no significant difference between the two groups. Thus the interest of the cement has not been proved in the case of tuberoplasty, this matches the results of Spies et al. [2] showing that when the cavity is less than 0.47 mm 3, the use of cement is not justified. It's also noted that the mean age of our subjects is older than of patients with a fractured tibial plateau. Using a bone substitute bovine type or phosphate kind, could be considered to promote bone growth, especially among younger subjects.

In vivo response to low-modulus PMMA bone cements in a rodent model

C Persson[1], E Carlsson[2], K Treerattrakoon[2], A López[1], M Nilsson[1], S Larsson[2]

[1] *Div. of Applied Materials Science, Dept. Engineering Sciences, Uppsala University, Uppsala, SE.*
[2] *Dept. of Surgical Sciences-Orthopaedics, Uppsala University Hospital, Uppsala, SE*

INTRODUCTION: Low-modulus bone cements based on PMMA have been developed as a response to the increased amount of adjacent fractures reported upon vertebroplasty [1]. It has been hypothesized that one contributor to these additional fractures may be the high stiffness of the cement. Acrylic bone cements commonly have an elastic modulus between 1.7-3.7GPa, while the modulus of the surrounding trabecular bone is 10-750MPa, depending on site, age and presence and degree of pathology. While a substantial amount of research has been performed on the bench properties of low-modulus cements, there is no data on their biological response in an in vivo model. The aim of this study was to evaluate the in vivo response to some of the previously proposed low-modulus cements, namely PMMA modified with castor oil or linoleic acid [2].

METHODS: Osteopal®V (OP, Heraeus Medical GmbH) was used as the base cement. 12.3wt% (of total cement weight) castor oil (CO, 259853, Sigma Aldrich) or 1.5wt% 9-cis,12-cis-linoleic acid (LA, W338001, Sigma-Aldrich) were incorporated into the cements. Disc-shaped samples ($\varnothing = 6mm$, $h = 2$ mm) were prepared and allowed to set for 1h at room temperature, and then for another 24h in PBS at 37°C. The local ethical committee approved the study (Approval No. C208/12). 19 male Sprague-Dawley rats (Taconic Farms Inc.) were randomly distributed into three groups/time points (TP): 1, 4 and 12 weeks, and all individuals received implants of all three material compositions (OP, OP-CO and OP-LA). Each animal received eight implants, with the materials distributed equally within each group. At the TPs, the implantation sites were assessed by macroscopical observation as well as histology (hematoxylin and eosin staining) [3]. Flow cytometry analysis (BD LSR II, BD Bioscience) was performed on enzymatically-digested tissue surrounding the implants up to a 5mm distance [4].

RESULTS: All animals tolerated the surgery and the post-operative period well, and macroscopic and histological assessment of the implant sites showed no signs of tissue irritation or prolonged immune reactions throughout the study. No statistically significant effect of material type was found in terms of amount of specific immune cells around the implantation sites, as assessed by flow cytometry (Table 1). For macrophages there was no statistically significant effect of time on the cell amount, and for the leukocyte and granulocyte populations there were only cases of decrease over time (between 1 and 12 weeks for the leukocytes, and between 4 and 12 weeks for the the granulocytes).

Table 1. Amount (in %) of immune cells surrounding the implants. Average (standard deviation).

	TP (w)	Leuko-cytes	Macro-phages	Granulo-cytes
OP	1	12.1 (4.7)	6.3 (3.2)	3.8 (2.5)
	4	9.3 (2.6)	7.9 (4.2)	5.6 (2.9)
	12	10.6 (3.9)	7.1 (3.5)	3.9 (2.5)
OP-CO	1	9.9 (4.3)	5.9 (2.9)	3.8 (2.3)
	4	10.3 (3.9)	8.2 (3.6)	7.2 (4.2)
	12	8.4 (1.8)	6.0 (3.0)	3.1 (1.2)
OP-LA	1	13.7 (5.1)	8.8 (3.6)	5.5 (3.0)
	4	9.1 (3.6)	6.1 (2.9)	4.6 (3.0)
	12	7.5 (3.3)	5.0 (2.7)	2.7 (1.8)

DISCUSSION & CONCLUSIONS: In all materials, a normal inflammation reaction of the non-specific immune response appeared to take place, since a vast majority of leukocytes present at the implant sites were macrophages and granulocytes. No significant difference in the immune response was found for the modified PMMA cements (OP-CO and OP-LA) compared to the base cement (OP) and no delayed immune response appeared to be triggered in any of the cases. This is the first time that low-modulus acrylic bone cements have been evaluated in an in vivo model. While the results are promising, the mechanical functionality of these types of cements remains to be evaluated in vivo.

New apatitic calcium phosphate cements associated with local analgesic: Preliminary *in vitro* and *in vivo* experimental results

E Verron[2], O Gauthier[2,3], J-M. Bouler[1], P Janvier[1]

University of Nantes, CNRS UMR 6230, CEISAM[1], 2 rue de la Houssiniere, 44322, Nantes, France

University of Nantes, INSERM U791, LIOAD[2], 1, Place Alexis Ricordeau, 44042 Nantes, France

Preclinical Investigation and Research Center, ONIRIS College of Veterinary Medicine, Nantes, France

INTRODUCTION: We have been working for years on the development of new calcium phosphate cements (CPC) incorporating either bone resorption inhibitors (bisphosphonates and Gallium) or blood, in order to promote bone reconstruction in bone disease sites. While continuing this work, our interest is also focused on the association of analgesic with CPC. In fact postoperative pain following bone reconstruction is considered as one of the major undesirable complications largely described in literature especially in bone iliac crest procedure. In this clinical context we are interested in developing new injectable combined calcium phosphate cements that deliver "in situ" local anaesthetics such as Bupivacaine and Ropivacaine. This study follows previous promising experiments related to the association of bupivacaine with calcium deficient apatite (CDA) [1].

METHODS: Different formulations of commercial apatitic cements were loaded with different rates of bupivacaine and ropivacaine according to a process of ethanolic impregnation [2] or a simple mix with the components of these apatitic cements mainly constituted by α-TCP (78%). The cement paste is prepared by mixing the obtained powder with an aqueous solution of Na_2HPO_4 with a liquid/solid ratio adapted to each combined cement. The final product obtained after the setting process is in all cases CDA loaded with a local anaesthetic. Twelve rabbits were implanted for eight weeks with cement loaded with 0, 8% and 16% of bupivacaine in both proximal femurs (contralateral vs combined cement). A bone defect was created on the iliac wing of twelve adult female beagle dogs mimicking a unicortical posterior iliac bone graft, according to European Community guides for the care and use of laboratory animals (2010/63/UE) after approval of the local animal welfare committee. Each dog was implanted unilaterally with the bupivacaine-loaded (8%) cement or the unloaded control one. Eighteen Wister female rats were unilaterally implanted for eight weeks with 0%, 8% of bupivacaine and 8%

ropivacaine, in critical cylindric defect in distal femur.

RESULTS: Incorporation of bupivacaine and ropivacaine into the solid phase of a cement affect its setting reaction and therefore its intrinsic properties in a dose dependant manner. However differences appear in the behaviour of ropivacaine-loaded cement vs bupivacaine-loaded cement. In vivo study on rabbits indicates an excellent tissue tolerance of bupivacaine-loaded cement once implanted. The final rate of 8% of bupivacaine seems to be more appropriate in terms of bone reconstruction and analgesia. In the case of dogs, bupivacaine-loaded (8%) CPC provided very local and better short-term pain relief compared to the unloaded cement.
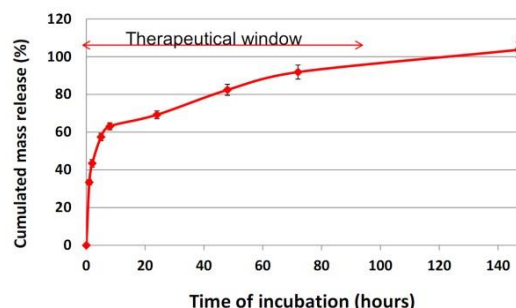

Fig. 1: Release profile of bupivacaine-loaded (8%) CPC.

DISCUSSION & CONCLUSIONS: These injectable combined CPCs are well tolerated and provide a controlled release of local anaesthetics that could be a part of the global management of pain following bone reconstructive surgery.

Micro-strain measurement of PMMA bone cement using Digital Image Correlation (DIC) method

J Zhang[1], G Baroud[1]

[1]*Laboratoire de Biomécanique, Faculté de Génie, Université de Sherbrooke, Canada*

INTRODUCTION: Extensometer and strain gauge are two conventional methods used in the measurement of stress-strain curves of PMMA bone cement. However, they have certain disadvantages. For example, extensometer is destructive to the specimen surface, limited region monitored and single time measurement. For the strain gauge, complicated installation is also another disadvantage. The DIC was proposed in 1989 by Sutton et al [1] for non-invasive measurement of displacement and micro-strains. It uses only one reference image before deformation and the other image after the deformation. By using correlation function and Newton-Raphson iteration, DIC method can calculate the full-field displacements and strains at sub-pixel level. This study measures the strain of PMMA specimens in uniaxial tensile experiment using the DIC method and compares the results to measurements by strain gauges for validation of the in-house DIC code.

METHODS: Four PMMA (DP-Pour, DentPlus, QC) tensile specimens are fabricated according to the ASTM standard 638. Firstly, one side of the specimen is sprayed with paints to generate the speckle pattern. Secondly, a gauge rosette is bonded on each side of the specimen at the same location (front and back of the specimen). Thirdly, the specimen is installed in the MTS machine (858 Mini Bionix II). The setup is shown in Fig. 1 for the DIC measurement. Both the strain gauge and DIC measurements were synchronized. After the test, 19 time points of recorded images are used to compute the strains using the in-house developed DIC algorithm. The force data is generated from the MTS machine. The principal strains and axial stress-strain curves obtained by DIC and gauge data are compared.
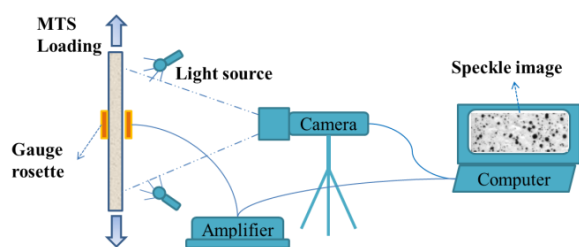
Fig. 1: DIC setup during axial tensile experiments.

RESULTS: Fig. 2 representatively shows the principal strains of two methods over time until the failure of the specimen. Fig. 3 shows the axial stress-strain curves of the two methods. The strain gauge measurements are on average stiffer than the DIC measurements.
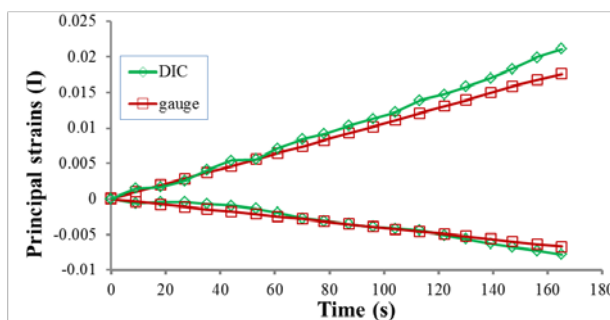

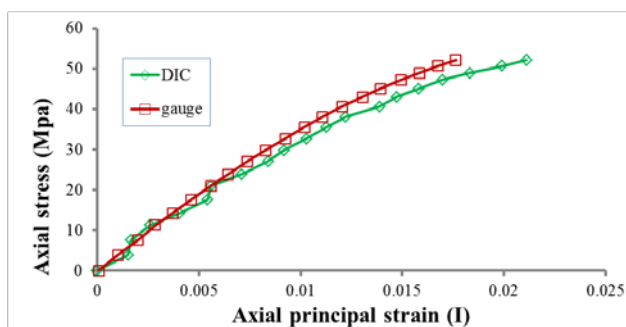*Fig. 2: The curves of axial and transversal strains.*

Fig. 3: The curves of principal stress versus strain.

DISCUSSION & CONCLUSIONS: The strains from the DIC algorithm were sufficiently close to what the strain gauge measured. Specifically, strains in the DIC group are 15.8% higher than those in the gauge group. It appears that the strain gauge measurements are stiffer which may be caused by the added local stiffness of the two gauges to the front and the back of the specimen. Also, variations in the same range between the front and back strain gauges were observed which may result from air bubbles in the specimens. Further investigation will follow with specimen made from stiffer material to avoid the added stiffness by the strain gauges to further validate the algorithm.

Injectability of calcium-phosphate pastes following prolonged milling

M Habib[1], M Bohner[2], G Baroud[3]

[1]*Mechanical Engineering Department, Al-Azhar University, Cairo, Egypt.* [2]*RMS Foundation, Switzerland,* [3]*Laboratoire de Biomécanique, Université de* Sherbrooke, *Canada.*

INTRODUCTION: Calcium-phosphate (CaP) ceramics are used for the bone repair and regeneration. However, these materials have a limited injectability in percutaneous applications [1, 2]. This study focuses on a physical approach in that it attempts to improve injectability by milling, which is assumed to render the particle more spherical. Mechanical energy applied to the particulates in the milling process will also change the particle size and distribution, particle shape, density and flowability. The Carr's index is an indication of the flowability of the powder. As the index decreases, the powder flowability increases. This study will correlate this index with the injectability of CaP paste.

METHODS: β-tricalcium phosphate (β-TCP; $Ca_3(PO_4)_2$; Fluka No. 21218, Buchs, Switzerland) was used as a feed powder. Milling was performed under isothermal conditions using a single-component Hosokawa grinder (Mechano Fusion System (AMS), Hosokawa Micron Powder Systems, NJ). Three batches of one kg each were processed for 30, 60 and 90 minutes, respectively. The feed and milled powders were investigated by scanning electron microscopy, the laser diffraction and X-ray diffraction. In addition, the plastic limit as described in earlier studies [1] was measured as an indicator for the wettabilty. Carr's index is calculated by the formula,

$$C = 100(1 - \frac{\rho_B}{\rho_T})$$

Where ρ_B is the aerated bulk density and ρ_T is the tapped density of the powder. The injectability test was performed using an 858 Mini Bionix II testing system (MTS Systems Corporation, Eden Prairie, MN). The injectability results were then correlated to Carr's index.

RESULTS: Milling reduces the median particle size (Table 1) which is consistent with the SEM and PSD measurements (Fig. 1 and 2). SEM results shows that particles less than 1 μm are agglomerated on the large particle surfaces with erosion of particle edge that makes it more spherical (Fig.1). Initially, the tap density deceases by milling for 60 min, and then it increases (Table 1). The same trend was observed for the powder permeability. Accordingly, Carr's index reduces indicating the milling reduces compaction and increase powder flowabillity. Injectability significantly increased from 69 to 84% (Table 1).
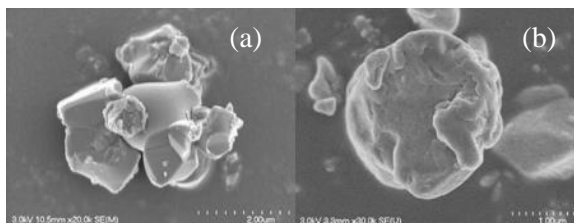

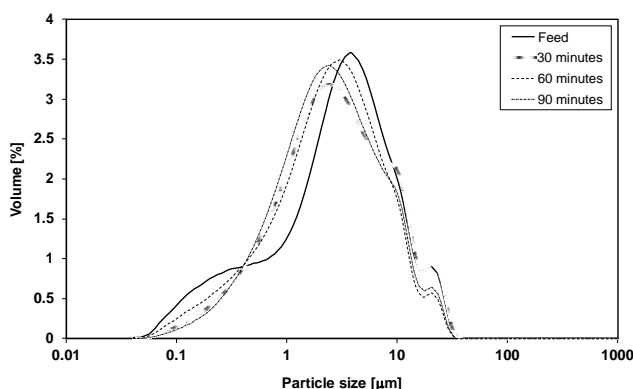*Fig.1: SEM of (a) Feed (b) milled for 60 minutes.*

Fig.2: PSD of feed and milled powders.

Table 1. Median PSD in μm, plastic limit in ml/g, densities in g/cm³, Carr's index and injectability of feed and milled powders

	Me d.	PL	Tap	Aerated	Inde x	Inj [%]
Feed	3.16	0.31	1.22	0.728	40.33	69.37±0.39
30-min	2.72	0.31	1.22	0.762	37.75	81.61±1.49
60-min	2.66	0.29	1.24	0.76	38.51	84.28±1.01
90-min	2.53	0.29	1.26	0.8	37.53	83.36±0.96

DISCUSSION & CONCLUSIONS: Milling c decreases the particle size and changes its distribution. However, prolonged milling may fuse particles, potentially will result in reducing the amount of fine powder species, which is consistent with permeability and tap density results. More compacted fused powders are likely causing reduction in both PL, and Carr's index which help with extruded fraction.

Calcium phosphate cement reinforced with natural cellulosic fibers

P Leuret[1,2,4], F Tancret[3], P Pilet[2], P Janvier[1], J-M Bouler[1], B Bujoli[1]

[1]*CNRS UNR 6230, Chimie Et Interdisciplinarité : Synthèse Analyse Modélisation, Université de Nantes, France.* [2]*INSERM UMRS 791, Laboratoire d'Ingénierie Ostéo-Articulaire et Dentaire, Université de Nantes, France.* [3]*Polytech Nantes, Institut des Matériaux Jean Rouxel, Université de Nantes, France .*[4]*Graftys SA, Aix en Provence, France*

INTRODUCTION: Calcium phosphate cements (CPC) are well-established materials for the repair of bone defects with excellent biocompatibility and bioactivity. However, brittleness and low flexural strength restrict their application to non-load bearing areas. Reinforcement of CPC with fibers can substantially improve its strength and toughness, and has been one major strategy to overcome the present mechanical limitations of CPC [1, 2]. We investigated the potential of a novel system based on natural cellulosic fibers while studying the relation between the material design and its mechanical and handling properties.

METHODS: CPC were provided by Graftys. Fibers come from different sources -cotton, linen, hemp-. Fibers were included by simple mixing in the cement paste. Cement compressive strength was first measured. Then chevron notched specimen were tested by 3-point bending to evaluate their fracture toughness. We investigated the effect of fiber type, fiber length, fiber volume fraction on the mechanical performances of the fiber reinforced calcium phosphate cements (FRCPC). We also studied the effect of a simple surface treatment by cleaning linen fibers with NaOH at 80°C. Cement structure was controlled by infrared and X-ray diffraction. Cement and fibers microstructure, and their interface, were observed by scanning electronic microscopy.

RESULTS: FRCPC with cellulosic fibers have significantly increased mechanical properties compare to unreinforced cement. In compression, fibers maintain up to 60% of cement compressive strength after the matrix breakup. In flexion, fibers increase cement's flexural strength and fracture toughness. In Fig. 1, we can see that mass fraction of fibers have a strong impact on the flexural strength. The large area below the curve indicates a good reinforcement. At 5 % fiber, a pseudo ductile behaviour is observed [1]. Fibers mechanical properties, surface state, size distribution and mixing process in the cement paste were shown to have a strong impact on the composite performances.
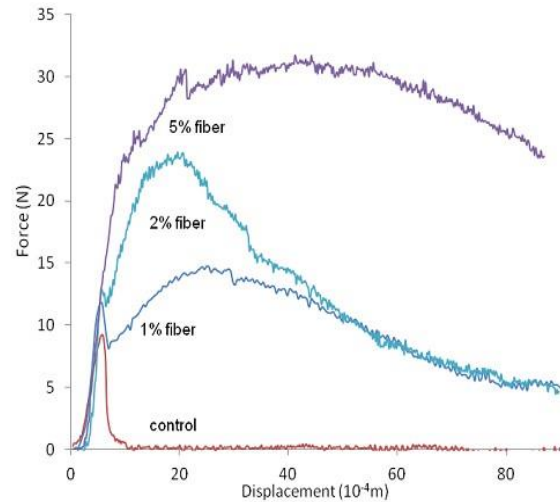

Fig1: 3-point bending tests on chevron notched specimens (8 x 8 x 36 mm) of cotton FRCPC

DISCUSSION & CONCLUSIONS: We hope this study concur with reviewers [1] that underline that more focus is needed on curves, and on the mechanical mechanism of fiber reinforcement rather than only strength values. Also, while cellulose fibers are well integrated by bone, they are not degradable [3]. However functionalized cellulose is developing and shows better degradation and even improved osteo-integration [4]. Natural fibers showed interesting performances for CPC reinforcement. We underline that fibers mechanical properties, surface state, size distribution and mixing process in the cement paste have a strong impact on the composite performances. Pure cellulose in not an optimal biomaterial but the mechanical properties of our system may increase the interest in modified cellulose fiber reinforced CPC.

Seepage effect to control cement filling in the bone augmentation procedure

S Alenezi[1], F Benyahia[2], S Becker[3], M Bohner[4], G Baroud[1]

[1]*Laboratoire de Biomécanique, Université de Sherbrooke, Canada.* [2]*King Saud University, Kingdom of Saudi Arabia.* [3]*IMSART, Austria.* [4]*RMS Foundation, Switzerland.*

INTRODUCTION: Treating osteoporotic fractures often fails because of the inherent difficulty to anchor orthopedic screws in the weakened bone. Augmenting the bone with a biomaterial is an effective approach to instrument the bone structure [1-3].The bone cement, as per example, is injected into the osteoporotic bone by different delivery tools to control the in-situ distribution. We present a novel delivery cannula to improve the distribution of the biomaterial and therefore the effectiveness of the treatment. Such a cannula is designed to have a sufficiently large conduit and relatively small slots at its distal end. The slots are sufficiently small for the conduit to represent a path of least resistance. Specifically, the cement fills the conduit first until it reaches the distal end of the cannula, and once the cannula is completely filled, the inside pressure increases and allows for the cement to seep uniformly through the distal slots. This study examines computationally a novel design of perforated cannula with variable slot diameter to investigate the cement uniformity.

METHODS: A 2D model of the bone domain including the tip of the perforated cannula is generated and discretized with 20400 elements. Mesh is refined at the vicinity of the slots to capture locally the complex physics and produce an accurate flow profile. The cement flows from the inlet (top side of the cannula), and enters the bone domain from the lateral slots (Fig.1). Two sets of boundary conditions (BCs) are applied to simulate the physical process: the flow and the volume-of-fraction boundary conditions. The top side of the cannula (entrance) has the inlet BC with a constant flow rate of $1mm^3/s$. The bottom side of bone domain is the outlet with no resistance. All the remaining boundaries are the non-slipping wall BCs (zero velocities). Two geometric configurations (slot diameters; $S_d = 0.5$ mm and 0.25mm) are studied. The cement is considered a Newtonian fluid having a constant viscosity ($\eta=1000$ Pa·s). The cement extrusion patterns are studied in addition to the delivery pressure.

RESULTS: Fig.1 (a, b) show the cement extrusion patterns resulting from S_d of 0.5 and 0.25 mm, respectively. Fig.1 (c) shows the time variation of the delivery pressure of the two slot sizes. The first segment of the pressure curve (S_1) represents the cannula conduit being filled. The transient jump denoted by (S_2) represents the required pressure to initiate the cement seepage in the bone domain. The third segment (S_3) represents the steady-state pressure for the cement seepage.
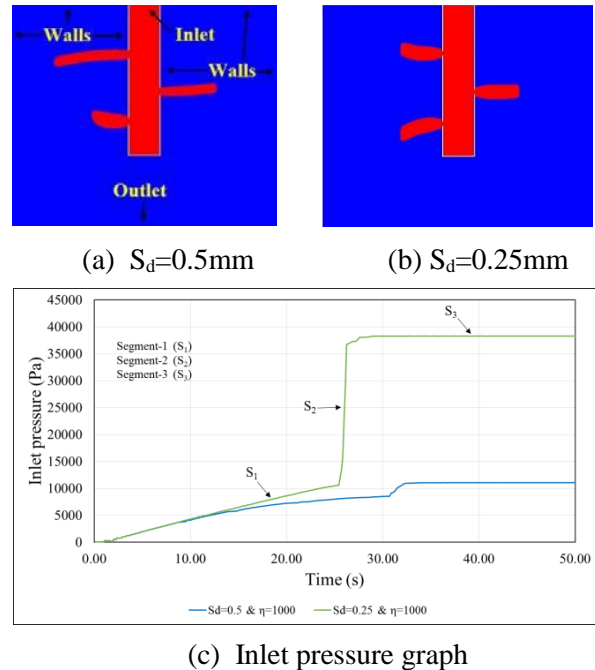

(a) S_d=0.5mm   (b) S_d=0.25mm

(c) Inlet pressure graph

Fig. 1: Flow profiles and pressure graph

DISCUSSION & CONCLUSIONS: The computational model helps design the seepage mechanism (the uniform extrusion). A small slot-conduit ratio (SSCR) resulted in a uniform extrusion pattern (Fig.1-b). Specifically, in the low SSCR, the cement seeped simultaneously from the slots for a more uniform filling pattern. This could be explained by the inverse proportionality between the required pressure for the cement seepage and the SSCR. Therefore, high attention should be given to the choice of SSCR of the perforated cannula to achieve a uniform and potentially safe augmentation procedure.

Review of poly(methyl methacrylate) bone cement

JM Yang

Department of Chemical and Materials Engineering, Chang Gung University, Kwei-Shan, Tao-Yuan, Taiwan

Poly(methyl methacrylate) PMMA was developed in 1928 and was marketed in 1933. During World War II acrylic glass was used for submarine periscopes, windshields, canopies, and gun turrets for airplanes. Dr. Harold Ridley (1906-2001) examined aviators who were unintentionally implanted in their eyes with shards of plastic from shattered canopies in fighter planes. PMMA is used in hard contact lens therefore. In 1984, Galibert and Deramond described the vertebroplasty procedure. The technique consisted of injecting bone cement, originally PMMA.

Life expectancy is around 80 years [1]. For the long life expectancy, the choices for application product to replace/substitute bone are ample [2]. PMMA with relatively cheaper price and has advantages such as low viscosity, easy to perfuse, sufficient ability to strengthen and stiffen vertebral body quickly. At present, PMMA is the most commonly used filling material in vertebral augmentation procedures. There are some medical application of PMMA such as bone cements, contact and intraocular lens, prosthetic fixation, filler for bone cavities and skull defects, spacers, vertebrae stabilization in osteoporotic patients, denture bases, and antibiotic carrier [3, 4].

The chemical composition of PMMA bone cement consists of a solid powder and a liquid component. The solid powder contained PMMA, Methyl methacrylate-styrene copolymer, $BaSO_4$, and benzoyl peroxide. The liquid component contained Methyl methacrylate monomer, N,N-dimethyl-*p*-toluidine, and hydroquinone. All bone cements on the market fulfill the basic requirements for an orthopedic implant, but there are differences in their properties because of the different powder and liquid compositions. Not all bone cements are alike, and therefore, it is the surgeon's own choice to use an appropriate material to get the optimal result for the patient [4].

When this PMMA bone cement is used for surgery, some major problems are found. These include thermal necrosis of bone, chemical necrosis due to unreacted monomer release, shrinkage of the cement during polymerization, poor cement distribution around the implant and property mismatch at the interfaces because the cement is orders of magnitude weaker than the bone or implant. Many researchers have attempted to solve these problems by incorporating additional agents into conventional ingredient of the acrylic bone cement to provide good initial fixation while allowing tissue ingrowth into the cement to maintain long-term stability.

Improvements of the cements' performance are the key aims to improving patient health. Research needs to be done to determine which material properties are clinically relevant for surgery. New filler materials, such as composite resin materials, calcium phosphate, or calcium sulfate cements, in addition to new PMMA formulations are now available for clinical use [5, 6].

Polymerization or the curing interval can be manipulated by changing the handling temperature. Basically, it depends on the mechanism of free radical polymerization of acrylic bone cement [7, 8]. The order of the polymerization reaction and the reaction rate constant for understanding the thermal necrosis of bone cement can be investigated by differential scanning calorimetry.

CHARACTERIZING ACCESSIBILITY OF POROUS CALCIUM PHOSPHATE SCAFFOLDS

S Jerban[1], G Baroud[1], M Bohner[2]

[1]*Laboratoire de Biomécanique, Université de Sherbrooke, Canada.* [2]*RMS Foundation, Switzerland*

INTRODUCTION: Porous bone substitutes (BSs) are used to promote bone repair process in critical size defects. Biological responses to BSs are always associated with cells migration and growth of blood vessels from host bone to inner pores. BSs with better accessibility are hypothesized to enhance the rate of biological responses. For example, the calcium phosphate BSs with higher accessible surface and porosity demonstrate faster scaffold resorption. From accessibility point of view, interconnections closer to peripheries are more influential to cells migration. Consequently, the queuing orders of pores and interconnections along paths from periphery to BS center are quite important. The pore accessibility is dominated by the largest penetrating diameter (LPD) to it. LPD of each pore indicates the size of largest sphere, i.e. growing vessel that can reach it (Fig. 1a). Total BSs accessible surface and volume by different sphere sizes can be used to predict biological responses. Specifically, the scaffolds with higher accessible surface are hypothesized to be more resorbable. This study focuses on calculating the accessibility parameters in four groups of β-TCP scaffolds (A, B, C and D with mean pore size of 150, 250, 500 and 1000 µm respectively) [1].

METHODS: After segmenting the µCT data of β-TCP scaffolds, local parameters are characterized using the isolating algorithm [2] combined with fuzzy distance transform. Subsequently, pore and interconnection coordinates in addition to local sizes are used to extract the pores network data in BSs. Thereafter, the accessibility parameters are calculated by analyzing the extracted data of all pores and interconnections (*i.e.* size, volume, surface, coordinate and connection labels). The algorithm calculates the accessibility parameters hierarchically from first penetration level i.e. peripheral pores, toward the pores at BS center. Specifically, the LPD of each pore is equal to the minimum value between entering interconnection size and LPD of preceding pore in hierarchy. Afterward, total accessible surface and volume by various penetrating sphere sizes are calculated. Specifically, for sphere size "*dia*", the accessible surface is equal to summation of pore surfaces where LPD $\geq$ *dia*. Finally, the axial projected maps of accessible surface and volume fractions are calculated to predict the regional variations of biological responses.

RESULTS: Fig. 1b shows total accessible surface by different range of penetrating sphere sizes. Fig. 2 shows the projected maps of accessible surface in group B and C by penetrating sphere sizes of 100 and 150 µm.
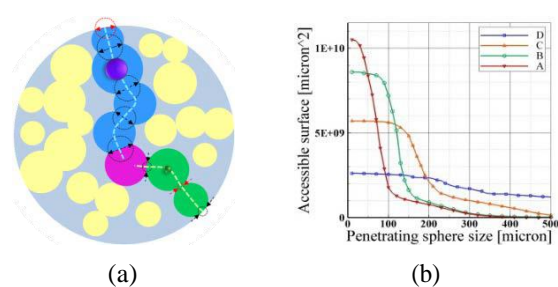

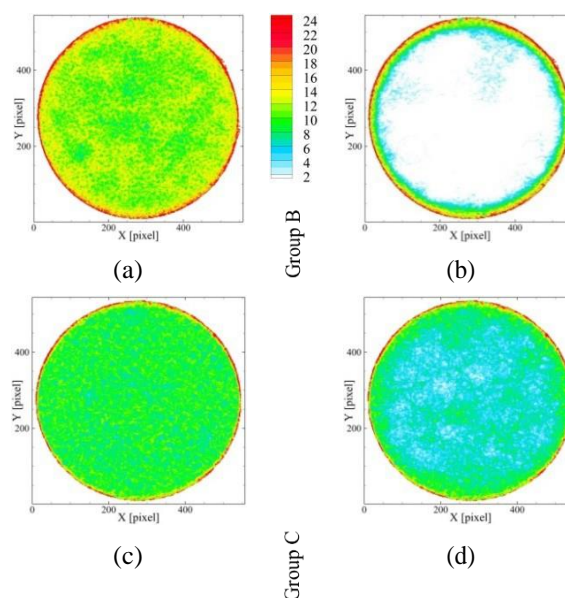Fig. 1: (a) LPD of a pore via two paths. (b) Total accessible surface versus penetrating sphere sizes.

Fig. 2: Projected maps of accessible surface in B and C by (a, c) 100 and (b, d) 150 µm spheres.

DISCUSSION & CONCLUSIONS: Accessible surface by the sizes of penetrating spheres can be used for prediction the scaffold resorption. Such specific sizes can be found by evaluating the in vivo results with respect to the geometric data of scaffolds. Due to different sizes of cells, specific sizes are different for bone deposition compared with scaffold resorption.

Biomechanical analysis of spinal instrumentation systems for thoracolumbar fractures: standard open surgical instrumentation *vs* percutaneous vertebral expansion and hybrid techniques

A Germaneau[1], T Vendeuvre[2], M Saget[2], P Doumalin[1], JC Dupré[1], F Brémand[1], F Hesser[1], C Brèque[1,3], P Maxy[4], M Roulaud[5], O Monlezun[5], P Rigoard[5]

[1] Institut Pprime UPR 3346, CNRS – University of Poitiers – ENSMA, France. [2] Department of Orthopaedic Surgery and Traumatology, University Hospital, Poitiers France. [3] Laboratory of Anatomy, University of Poitiers, France. [4] Medtronic International Trading Sarl, Tolochenaz, Switzerland. [5] Department of Neurosurgery, N3 Lab, University Hospital, Poitiers, France

INTRODUCTION: Thoracolumbar burst fractures are usually caused by dynamic axial compression of spine segments. A surgical treatment is needed for most of the cases to restore bone stability, prevent neurological deterioration and provide pain relief. The purpose of this study was to compare mechanical behaviour under physiological loadings of four types of stabilizations devices, including 2 open instrumentations and 2 percutaneous techniques: classical Posterior Fixation standalone (PF); Posterior Fixation associated with anterior screwed Cage-Plate, following a corpectomy of the fractured vertebra (PF-CP); percutaneous Kyphoplasty standalone (K); percutaneous Kyphoplasty and Posterior Fixation (K-PF).

METHODS: Twenty four anatomical fresh frozen human spine specimens (T11-L3) were prepared. Soft tissues were removed but discs and ligaments were carefully preserved. For each spine specimen, a burst fracture has been generated on L1 by dynamic compression by using of a Charpy pendulum [1]. Then each fracture has been stabilized by one specific type of fixation consisting in 4 groups of 6 specimens. Generation of the burst fracture and positioning of implants and fixations have been verified and validated by X-ray tomography. Physiological loadings were reproduced on specimens from a specific spinal loading simulator imposing pure moments according to physiological axis. The ranges of motion (ROM) between two adjacent units were measured from an optical method by 3D mark tracking technique. Cyclic moments on intact specimen before burst fracture and after stabilization have been imposed.

RESULTS: Fig. 1 shows evolution of ROM between intact segments before fracture and after stabilisation according to the spinal unit and for a pure moment in flexion equal to 5 N.m. Stabilization by kyphoplasty standalone (K) involves a higher mobility after stabilization compared to values observed before fracture.

Stabilizations by kyphoplasty – posterior fixation (K-PF) and by posterior fixation – cage-plate (PF-CP) provide higher stiffness. For segments stabilized by posterior fixation standalone (PF), mobility is increased in the fixed vertebra. An optimized consolidation of the fracture by cement or cage can explain these results. Similar observations can be made for lateral bending or axial rotation movements.
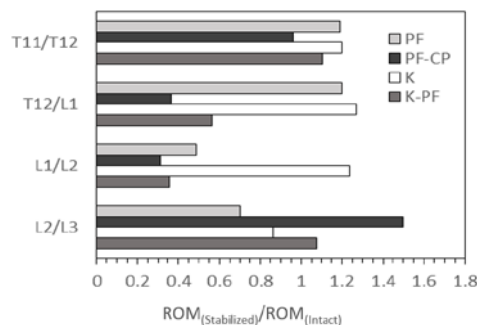

Fig. 1: Ratio between ROMs of stabilized and intact segments for flexion moment of 5N.m

DISCUSSION & CONCLUSIONS: Results obtained with anterior or posterior fixations (PF-CP and PF) are in accordance with previous investigations of Bence et al. [2] who studied the biomechanical behaviour of human thoracolumbar spines with anterior or posterior instrumentation. Our results also suggest that percutaneous surgical technique could be an interesting alternative after a burst fracture by providing a good compromise between biomechanical stabilization and invasiveness. Although kyphoplasty standalone is responsible for a higher segmental mobility, its association with a percutaneous posterior fixation provides an efficient stability.

Review of core decompression treatment in patients with Osteonecrosis of the Hip.

JC Villa[1], S Husain[1], A Gianakos[1], JM Lane[1]

[1]*Hospital for Special Surgery, New York, NY 10021*

INTRODUCTION: There are approximately 20,000 new cases of osteonecrosis (ON) of the femoral head every year [1, 2]. This comprises 5-18% of the more than 500,000 total hip replacements performed each year to diagnose and treat the ON [2]. Altered bone remodelling may be responsible for the pathogenesis of ON leading to the appearance of osteonecrosis itself, insufficient bone repair, and the evolution to subchondral fracture [2]. Current treatments include pharmacologic agents such as bisphosphonates, femoral head sparing procedures such as coring with or without the use of stem cells, and arthroplasty procedures including resurfacing and total hip arthroplasty. Although there has been clinical evidence to support these different therapeutic strategies, there has been no established treatment of choice demonstrating superiority in the treatment of ON. Many factors such as patient age, patient health, lesion size, and lesion stage must all be considered when determining a treatment plan [3]. This study attempts to review the clinical evidence of preservative surgical procedures to halt the progression of and treat ON in the femoral head and to hypothesise that coring with stem cells is better than coring alone.

METHODS: The PubMed/MEDLINE and EMBASE databases were screened using the following search criteria: "(avn OR avascular necrosis OR osteonecrosis OR osteonecrosis of femoral head OR onfh) AND (femoral head OR hip OR femur) AND (bisphosphonates OR forteo OR pth OR parathyroid hormone OR teriparatide OR coring OR core decompression OR stem cells OR drilling OR free vascularized fibular graft OR bone graft)". Only humans randomized control trials (RCT) studies comparing different treatments for AVN were included. Data was then extracted with a standardized table and grouped by type of treatment and outcomes.

RESULTS: RCT's of coring alone versus conservative treatment of ON of the hip (Fig. 1) demonstrate no significant superiority of coring. However, RCT's comparing coring plus bone marrow stem cells versus coring alone (Fig. 2), show a statistically significant difference in the odds ratio of femoral head collapse that favors coring + bone marrow stem cell treatment (P=0.04).
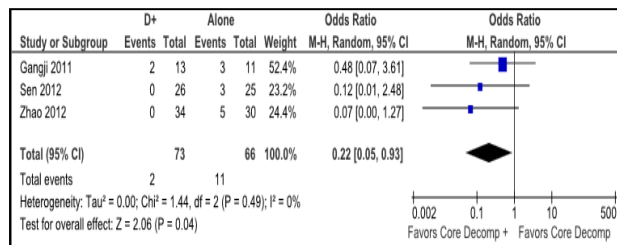

Fig. 1: Odds ratio of collapse for core decompression alone vs. conservative treatment.
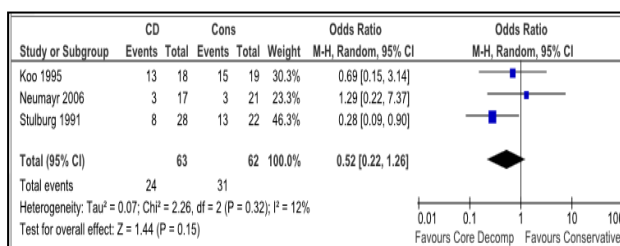

Fig. 2: Odds ratio of collapse between core decompression with bone marrow stem cells vs. core decompression alone.

DISCUSSION & CONCLUSIONS: Coring was reported to be the most commoly offered intervention for symptomatic, precollapse ON in the Unites States [3]. It has been performed with and without stem cells. Stem cells can potentially augment the biologic repair by differentiating in osteoprogenitor cells and resulting in bone formation. This systematic review of RCT's supports the observation that coring + stem cells is a procedure that result in better outcomes when compared with coring alone. Coring alone does not appear to provide improvement over conservative treatment.

Comparison between standard and augmented vertebroplasty in extreme vertebral fractures: when cement is not enough

DK Filippiadis, M Tsitskari, L Reppas, C Kostantos, E Brountzos, N Kelekis, A Kelekis

2nd Radiology Dpt, University General Hospital "ATTIKON", Athens/Greece

INTRODUCTION: Extended studies in the literature have proved the safety and efficacy of percutaneous vertebroplasty for endplate fractures or wedge impaction – vertebral body collapse. Vertebroplasty seems to be effective concerning pain reduction in patients with extreme vertebral fractures (split or incomplete burst fractures and in large osteonecrotic cavities). However, preliminary results of the same technique upon cement stability, widening of the fracture line and subsequent fracture in this setting, seem to be moderate. Furthermore, displacement of the fractured segment seems to be a potential complication of percutaneous vertebroplasty post cement injection.

METHODS: During the last 42 months, we retrospectively compared 2 groups (15 patients each) suffering from painful extreme vertebral fracture treated with standard (Group A) or augmented (Group B) vertebroplasty. Standard x rays and CT scans were performed during follow-up. Pain prior, the morning after and at the last follow-up (average follow-up 12 months) were compared by means of a numeric visual scale (NVS) questionnaire. Cement or implant migration were recorded.

RESULTS: Group A: mean pain value of 8.87 ± 0.99 prior and 2.27 ± 3.35 NVS units post treatment, with a mean decrease of 6.60 ± 3.07 NVS units ($p<0.001$); progress of vertebral body damage, widening of fracture line or PMMA migration, subsequent vertebral fracture) in 3/15 patients (20%) with 2/15 being surgically operated (13.3%). Group B: mean pain value of 8.73 ± 1.03 prior and 1.40 ± 1.40 NVS units post treatment, with a mean decrease of 7.33 ± 1.45 NVS units ($p<0.001$); no implant change or migration. Pain reduction difference between two Groups was not statistically significant ($p=0.72$). PMMA versus implant migration between two groups was marginally insignificant ($p=0.068$). Overall mobility improved in 13/15 patients in Group A and 15/15 patients in Group B.
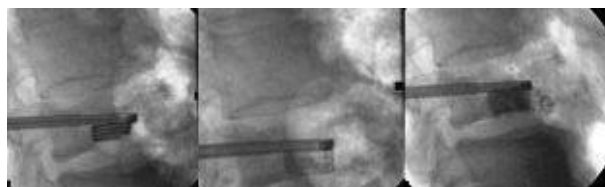

Fig. 1: Through the working cannula a nitinol coil is deployed (left image); Over the nitinol coil a PEEK polymer Cage is deployed inside the vertebral body and the nitinol coil is removed (middle image); Peek polymer cage is filled with PMMA under fluoroscopy (right image).

DISCUSSION & CONCLUSIONS: Concerning extreme vertebral fractures (split or incomplete burst fractures and large osteonecrotic cavities), the relatively high incidence of fracture relapse, or new fracture appearance in an adjacent vertebral body post to vertebroplasty or kyphoplasty created a great interest in the introduction of new, minimal invasive techniques reducing these complications [1, 2]. Both standard and augmented vertebroplasty seem to reduce pain in patients with extreme vertebral fractures. Preliminary results show potential tendency for widening of fracture line or PMMA migration and subsequent vertebral fracture in the vertebroplasty Group. Augmented vertebroplasty aims in providing improved mechanical stabilisation of the vertebral body, reduced complication rates and equal or better results in pain reduction comparing to standard vertebroplasty and kyphoplasty. This very promising technique could create new data in percutaneous treatment of extreme vertebral fractures (split or incomplete burst fractures and large osteonecrotic cavities). Augmented vertebroplasty could be established as an alternative treatment to surgical options or as a first line therapy for this kind of fractures.

Osteoporotic vertebral compression fractures (OVCF): kyphoplasty or conservative treatment?

JF Cazeneuve

Clinique Victor Pauchet, Amiens, France

INTRODUCTION: The purpose of this prospective study between January 2009 and January 2013 was to assess clinical and radiological outcomes 24 months after kyphoplasty or conservative treatment for osteoporotic vertebral compression fractures (OVCF) which have a highly negative influence in terms of morbidity in elderly [1-4].

METHODS: Forty-eight patients (mean age of 74 years, range of 55 to 92 years and 86% women) involving, according the Magerl's classification thirty-six A.1.2 and twelve A.3.1 vertebral fractures, from T 12 to L 5, were allocated to twenty-four kyphoplasties (Medtronic) and twenty-four conservative treatments consisting in a one-month bed rest principally in ventral position with physiotherapy and early mobilization in a swimming pool; then, the walking was authorized with a back brace for two months. All the patients were followed for a minimum of twenty-four months. We collected data by examining Visual Analogue Pain Scale (VAS), Oswestry score, Hospital Anxiety and Depression Scale (HADS), vertebral and kyphosis angles.

RESULTS: In the kyphoplasty group, which was free of complications, from the pre- and postoperative periods up to the twenty-four-month follow-up, VAS dropped from 8.7 to 3.9 and then to 2.9. Oswestry score dropped from 53 to 48 and then to 31. HADS score dropped from 12.0 to 10.1 and then to 9.8. The mean vertebral angle decreased from -15° to -5° and then moved to -10° and the kyphosis angle improved from - 20° to + 3° and then dropped to -5°. Asymptomatic leakage of cement was found in 6 cases (25%). In the conservative treatment group, at the twenty-four-month follow-up, the VAS, Oswestry and HADS scores were of 4.2, 41 and 12 points, respectively. The mean vertebral angle increased from 15° to 25° in 45% of the patients with a kyphosis angle remaining always negative. There were two cases of recurrent fractures in this last group.

DISCUSSION & CONCLUSIONS: For OVCF, our experience demonstrated that kyphoplasty can improve pain and functional status. This may help to correct vertebral deformity, hence these findings encourages further recruitment for kyphoplasty instead of conservative treatment.

Injectable functionalised self-assembling nano-peptides promote osteogenic differentiation of human Mesenchymal Stem Cells (hMSCs) *in vitro*

S Peggrem[1], JT Triffitt[2], Z Xia[1]

[1] *Centre for NanoHealth, Institute of Life Science, College of medicine, Swansea University.*
[2]*Botnar Research Centre, Nuffield Department of Orthopaedics, Rheumatology and Musculoskeletal Sciences, the University of Oxford, UK*

INTRODUCTION: Self-assembling nanopeptides are of great interest in the field of regenerative medicine for their unique characteristics that help support tissue repair and regeneration. The aim of this study was to assess a functionalised self-assembling nano-peptide hydrogel for its osteogenic potential when used with either Coralline Hydroxyapatite/Calcium Carbonate (CHACC) [1] or cuttlefish bone powder.

METHODS: We designed a new functionalised self-assembling nano peptide (AcN-RADARADARADARADAGGRGDARGDA-COHN2) with the functional group RGDA (The amino acid sequence for multiple calcium-binding sites were selected from the glycoprotein Thrombospondin). An additional group was created using RADA16 only (Puramatrix), the nano-fibres of which were coated in Bone Morphogenic Protein-2 (BMP-2) and the control group was composed of RADA-16 only. These self-assembling nano-peptide hydrogels were then integrated with either CHACC or cuttlefish bone particles in addition to human Mesenchymal Stem Cells (hMSCs) and cultured in α-MEM containing 10% FCS before testing for cytotoxicity and osteogenic potential.

RESULTS: The functionalized nano-fibre scaffolds exhibited no cytotoxicity in comparison to the control group (Fig. 1). hMSCs adhesion and differentiation in three-dimensional cell culture was prominent. AlamarBlue® assay confirmed cell proliferation was statistically significant within each group comparing day 7 to day 1 (Fig. 2). Confocal microscopy was used to observe cell viability and cytochemical staining of alkaline phosphatase was used to assess osteogenic potential. Alizarin Red staining confirmed calcification had occurred significantly more in the functionalized peptide groups than in the RADA16 alone group.
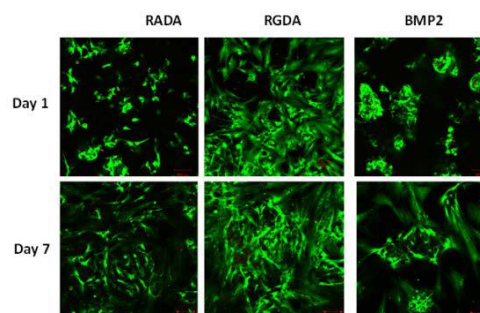

Fig.1: Live/dead staining observed using confocal microscopy at days 1 and 7 for hMSCs in self-assembling nono-peptides RADA-16, RADA with functional group RGDA and RADA coated with BMP-2 and incorporated cuttlefish particles. The results indicate an abundance of cells forming around the cuttlefish particles in the BMP-2 group throughout the 3-D gel structure.
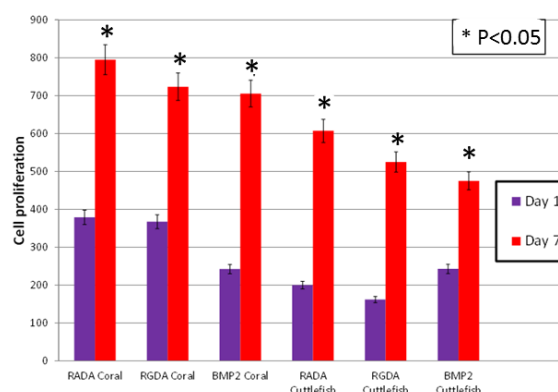

Fig. 2: AlamarBlue® assay showed cell number increases in 7 days.

DISCUSSION & CONCLUSIONS: The functionalised nano-fibre scaffolds had excellent biocompatibility in vitro and showed improved osteogenic potential with hMSCs. These scaffolds could be extremely valuable for future use in the field of bone regeneration.

"Tuberoplasty": A new minimally invasive bone augmentation procedure for tibial plateau fractures. First results of a prospective feasibility study.

T Vendeuvre[1,3], L Collet[1], S Teyssedou[3], M Saget[3], JP Richer[1], P Pries[3], LE Gayet[3], P Rigoard[4], C Breque[1,2]

[1] Laboratory of Anatomy, Faculty of Medicine and Pharmacy, University of Poitiers, France.

[2] P' institute, CNRS 3346, Futuroscope Chasseneuil, France. [3] Department of Orthopaedic Surgery and Traumatology, CHU of Poitiers, France. [4] N3 Lab, Poitiers, France.

INTRODUCTION: Tibial plateau fractures account for 1.2% of all fractures. The classical open osteosynthesis techniques or those using a bone tamp present several problems, such as a risk for infection, bone and skin devascularization, deferred weight-bearing or scarring issues. In addition, conventional surgery prohibits the making of a diagnosis and the treatment of the associated lesions simultaneously, unlike the arthroscopy. To address deficiencies, we developed a new technique. We performed on cadavers a stabilization procedure with a minimally invasive bone augmentation [1] for tibial plateau fractures. This technique called "Tuberoplasty" requires a balloon expansion and two percutaneous fixation screws+/-plate associated with Poly-Methyl-Meth-Acrylate (PMMA) cement filling. Our goal was to provide optimal anatomical reduction of the fracture, minimal aggressive osteosynthesis, offering to the patient a strong and instantaneous mechanical stability allowing early rehabilitation and rapid weight-bearing. We present in this abstract the first results of a prospective feasibility study performed on 30 operated patients. The aim of this study was to demonstrate the efficacy of tuberoplasty on initial stabilization and its potential interest in early post-operative mobilization.

METHODS: A number of 30 consecutive patients diagnosed with a fracture of the tibial plateau were operated with tuberoplasty. They were watched in a prospective way while the epidemiologists data such as Schatzker classification, observation of the presence of posterior depression; osteosynthesis by plate or screw, potential complications, weight-bearing, were collected during September 2011 and July 2014.

RESULTS: Our study included 16 males and 14 females of the average age of 48.6 (from 29.8 to 67.4). We counted in the study 3 fractures of medial tibial plateau. Within the fractures of the lateral tibial plateau, we counted 19 Schatzker 2, 2 Schatzker 6, 5 Schatzker 5, and 1 Schatzker 3. Six fractures showed a posterior depression which represented 20% of the whole study group. We realized 24 synthesis by screw, 5 Mini invasive surgery plates, one filing without synthesis. Every patient was filled by PMMA cement. The delay of recovery support was between 3 and 6 weeks, with an average of 4 weeks.

DISCUSSION & CONCLUSIONS: This study highlights the role of a bone augmentation compared to conventional techniques for the surgical treatment of tibial plateau fractures. The anterior point of introduction under the fracture site is made by an avascular window, decreasing the risk of infection and scaring issues. It also preserves the blood supply to the periosteum and bone union, and fills the newly formed residual cavity with PMMA cement. Associated with a cement-screw assembly, it provides an excellent stability in direct loading and therefore reduces postoperative immobilization and weight bearing. As we said before, patients were able to walk after 4 weeks. Finally, the balloon allows access to the posterior compression while eliminating the neurological and vascular risks of a conventional posterior approach. In conclusion, this new minimally invasive tuberoplasty technique could represent an interesting alternative to the conventional bone tamp technique for the reduction and stabilization of tibial plateau fracture.

Fig1: Ex. Tuberoplasty by screw and by plate

Sustained release of strontium from injectable calcium polyphosphate-derived brushite cement enhanced bone healing

WP Ren[1,2], W Song[2], DC Markel[3]

[1] Wayne State University, Detroit, MI, USA. [2] Virotech Biomaterials Inc., Detroit, MI, USA.
[3]Department of Orthopaedic, Providence Hospital, Southfield, MI, USA

INTRODUCTION: Many efforts have made to use bioceramic cements as local drug delivery systems. The present work aims to evaluate the in vitro release profiles and in vivo bone healing efficiency of strontium (Sr)-loaded calcium polyphosphate (CPP)-derived brushite cement.

METHODS: We developed method to prepare CPP gel. CPP-derived brushite cements were prepared by incorporation of tetracalcium phosphate (TTCP). Strontium carbonate (SrCO3) was introduced into CPP-cements via two methods, calcination [1] and simple mixing with CPP before reacting with TTCP for setting (final SrCO3 concentration 8%, v/v). Sr release was measured by ICP-OES. The bone healing efficacy was tested in a rat tibia defect model.

RESULTS: Sr was continuously released over 140 days (~ 5 months) from CPP-derived brushite cements (Fig. 1). The zero-order release of Sr is mainly due to the ionic interaction between Sr and the polyphosphate backbone of CPP. No major difference of Sr release pattern was found between calcination and simple mixing of SrCO3 into the CPP brushite cements. We believe that the Sr release is closely linked with the degradation rate of CPP- brushite cements. A trans-cortical tibia bone defect was created in the rats and the bone defects were filled with CPP-brushite cements with (n=3) and without (n=3) Sr doping. Bone defect healing was evaluated by Micro-CT. As shown in Fig. 2, CPP-brushite cements filled the bone defect area fully and evenly right after injection. 16 weeks after injection, Sr-doped brushite cements significantly enhanced new bone formation, as manifested by the integration with surrounding bone matrix without visible gap at the interface. The new bone formation was further confirmed by hard tissue histomorphometry. The degradation of CPP-brushite cement in the soft tissue was measured by injection of 0.2 ml of CPP-brushite cement in the muscle tissue near the tibia bone. We found that around 40% of CPP-brushite cements in the soft tissue were remained 16 weeks after injection.
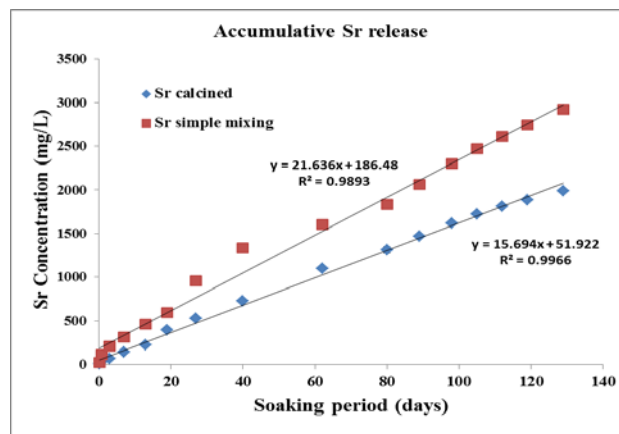

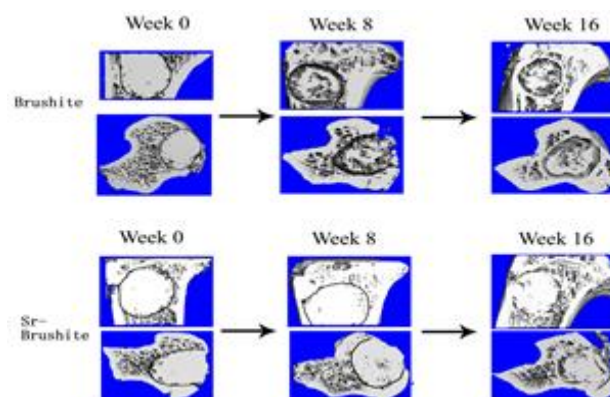Fig. 1: Release of Sr from CPP-derived brushite cements (n=3 per setting)

Fig. 2: Representative MicroCT images of the bone defects with CPP-derived brushite cements for 16 weeks of implantation (n=3 per group)

DISCUSSION & CONCLUSIONS: This study presented a simple way to prepare Sr-doped CPP-brushite cements. Our data demonstrated that a sustained release of Sr enhanced new bone formation in vivo. Our current studies strongly support that CPP-brushite cements represent one of the most promising local drug delivery device for the delivery of other molecules, such as growth factors and antibiotics. Additional beauties of CPP-brushite cements include safety, constant viscosity, controllable setting, low curing temperature, controllable slow degradation and strong mechanical strength.

Study on calcium silicate/magnesium phosphate composite bone cement

WJ Liu[1], ZG Huan[1], D Zhai[1], CT Wu[1], J Chang[1]

[1] *Shanghai Institute of Ceramics, Chinese Academy of Sciences, 1295 Dingxi Road, Shanghai 200050, P. R.China.*

INTRODUCTION: Our previous studies revealed that C3S was bioactive and biodegradable [1]. It could induce bone-like apatite mineralization in vitro and its ionic extract solution could promote proliferation and osteogenic differentiation of bone-related cells [2]. Despite the advantages of bioactivity and degradability, the compressive strength of C3S is relatively low and its setting time is too long for clinical application. Magnesium phosphate cement (MPC) is a kind of inorganic cements developed in recent years [3]. The main characteristics of MPC are its fast-setting ability and high compressive strength. Both in vitro and in vivo evaluations have revealed that MPC had good biocompatibility and moderate degradation rate. However, it is noticed that MPC failed to promote the differentiation of osteoblast cells and there is no evidence that MPC could stimulate bone regeneration. It is therefore assumed that bioactive cements may be obtained if C3S and MPC are reasonably combined.

METHODS: Then C3S and MPC powders were mixed at different mass ratios as follows: 25% C3S and 75% MPC (C25M75), 50% C3S and 50% MPC (C50M50), 75% C3S and 25% MPC (C75M25). The cement pastes were prepared by mixing the powders with de-ionized water. The composition and cross-section of the samples were then investigated by using the X-ray diffractometer and scanning electron microscope equipped with X-ray energy dispersive spectrum (EDS), respectively. The setting time of the cements was tested with Vicat apparatus according to ISO-9597-1989E. In vitro bioactivity of the composite cements was evaluated by soaking them in simulated body fluid (SBF). In vitro cytocompatibility of the materials was evaluated by the MTT method according to the international standard (ISO/EN10993-5). The data were denoted as means $\pm$ standard deviation (SD), and analysed with the Student t-test. If the $P < 0.05$, the results were considered statistically significant.

RESULTS: Composite cements were successfully prepared. The compressive strength of all the specimens increased with time proceeding during the curing. The setting time of the composite cements was shorter than that of the pure C3S cements. In vitro bioactivity evaluation showed that the composite cements were able to induce apatite formation. From the cell culture results, it can be seen that for all the cements, MC3T3-E1 cells had good viability in culture medium conditioned with different concentrations of ionic extracts, compared with the blank control group, suggesting their good in vitro cytocompatibility.

DISCUSSION & CONCLUSIONS: Our results confirmed our assumption that the addition of MPC into C3S resulted in cements with high mechanical strength. The compressive strength and setting time of the composite cements could be modulated by the weight ratio of C3S and MPC. Among the composite cements, C25M75 showed the highest compressive strength of which is 86 MPa, which is close to the lower limit of human cortical bone (90-209 MPa) and much higher than C3S and MPC. The composite cement has good apatite mineralization ability in SBF solution and degraded gradually with a moderate degradation rate in vitro. Moreover, the composite cement showed good in vitro cytocompatibility and stimulated the proliferation of MC3T3-E1 osteoblast cells. These results suggest that, through combination of C3S and MPC, it is possible to obtain composite cements which keep or even surpass the advantages of high compressive strength and bioactivity of its individual components. The bioactive high-strength C3S/MPC composite cement in the present study might have potential for orthopaedic applications.

Production of a thoracolumbar burst fracture model for biomechanical testing, including bone vertebral augmentation and posterior fusion procedures

A Germaneau[1], T Vendeuvre[2], M Saget[2], P Doumalin[1], JC Dupré[1], F Brémand[1], F Hesser[1],

C Brèque[1,3], P Maxy[4], M Roulaud[5], O Monlezun[5], P Rigoard[5]

[1] Institut Pprime UPR 3346, CNRS – University of Poitiers – ENSMA, France. [2] Department of Orthopaedic Surgery and Traumatology, University Hospital, Poitiers France. [3] Laboratory of Anatomy, University of Poitiers, France. [4] Medtronic International Trading Sarl, Tolochenaz, Switzerland. [5] Department of Neurosurgery, N3 Lab, University Hospital, Poitiers, France

INTRODUCTION: Spinal injury constitutes a current and devastating pathology in traumatology (10%). Thoracolumbar burst fractures are the most frequent associated lesions and concern generally young patients. Burst fractures are characterized by compression loadings involving lesion of the vertebrae endplate between the anterior and the posterior wall [1]. Choice of the optimal treatment can be delicate since only few biomechanical studies have been performed to establish mechanical response for each option. To bridge this gap, a reliable cadaveric model of burst fracture would be helpful to improve our knowledge of fracture mechanisms. The present work concerns the development of experiments to generate reproducible burst fractures and to perform biomechanical studies on the stabilization of damaged spinal segments, including vertebral bone augmentation.

METHODS: 24 human specimens (T11-L3) were used for the purpose of this study. At harvest, the spines were dissected and soft tissues carefully removed to preserve bony parts and spinal ligaments. A slight embrittlement was performed on the central vertebral body (L1) by drilling random holes of 0.8mm diameter. The upper half of cranial (T11) and the lower half of the caudal (L3) vertebra were fixed in rigid polyurethane resin to apply correctly boundary conditions. To produce burst fracture, dynamic impact tests were performed on spinal samples by using a modified Charpy pendulum to preserve an axial collision of the hammer on the spine specimen (Fig. 1). During impact, the biomechanical behaviour on specimen, including displacement and strain fields, were measured on vertebral bodies and disks by an optical method, based on mark tracking, coupled with a high speed camera (2000fps).

RESULTS: Fig. 2 shows evolution of strain values measured on vertebral bodies and disks during an impact on one specimen. Adjacent vertebral bodies are not deformed or damaged. Strain values in disks increase with impact but remain lower than strain measured in L1 at the level of the fracture.

We observed that all the specimens have a similar mechanical behavior during the impact and that compression strain value has to be higher that 0.05 to produce burst fracture.
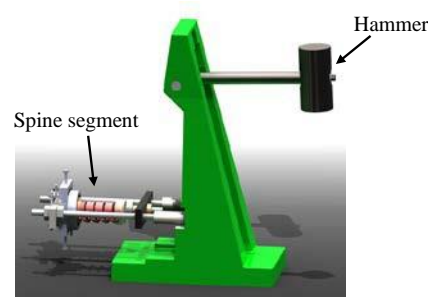

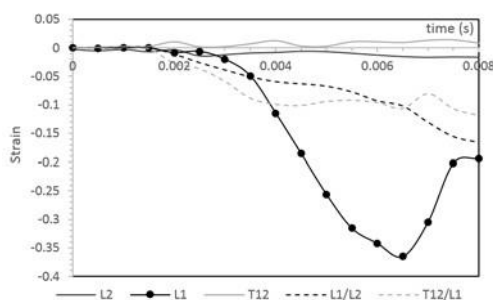*Fig. 1: Representation of our modified "Charpy pendulum"*

Fig. 2: Evolution of strain on vertebral bodies and disks during impact

DISCUSSION & CONCLUSIONS: An experimental protocol was developed to produce in vitro burst fracture of spine segments at the closest conditions of real trauma. X-ray tomography was used in parallel to characterize the initial morphology of the spine and to analyze the burst fracture consequences. Strain measurements and angular observations made on all the fractured specimens validate this novel method as a reproducible model to generate burst fractures for the purpose of high quality biomechanical studies.

Biomechanical analysis of vertebral bone augmentation by kyphoplasty to stabilize thoracolumbar Burst fractures

A Germaneau[1], T Vendeuvre[2], M Saget[2], P Doumalin[1], JC Dupré[1], F Brémand[1], F Hesser[1], C Brèque[1, 3], P Maxy[4], M Roulaud[5], O Monlezun[5], P Rigoard[5]

[1] Institut Pprime UPR 3346, CNRS – University of Poitiers – ENSMA, France. [2] Department of Orthopaedic Surgery and Traumatology, University Hospital, Poitiers France. [3] Laboratory of Anatomy, University of Poitiers, France. [4] Medtronic International Trading Sarl, Tolochenaz, Switzerland. [5] Department of Neurosurgery, N3 Lab, University Hospital, Poitiers, France

INTRODUCTION: Thoracolumbar burst fractures represent an important part of spine injuries. A surgical treatment is needed for most of the cases to restore bone stability, prevent neurological deterioration and provide pain relief. A percutaneous surgical technique involving a balloon vertebral expansion followed by an injection of cement (kyphoplasty) provides a vertebral bone augmentation with a reduction of morbidity. However some key points need to be clarified about this technique with a focus on its biomechanical effectiveness. This work presents a biomechanical analysis of kyphoplasty in its main indication represented by burst fractures stabilization.

METHODS: 6 human specimens of 5 vertebrae (T11-L3) were used for this study. At harvest, the spines were dissected and soft tissues carefully removed to preserve bony parts and spinal ligaments. To reproduce cyclic physiological loadings, a specific spinal loading simulator has been used to impose pure moments. First, specimen were tested intact by imposing loads of flexion/extension, lateral bending and axial rotation. Second, a burst fracture was generated on L1 on each specimen from a specific experimental protocol by using of a Charpy pendulum [1]. Third, each fracture was stabilised by percutaneous balloon Kyphoplasty. In the last step, stabilised specimens were tested in movements of flexion/extension, lateral bending and axial rotation. Two principal effects linked to the stabilisation with cement were measured by using a stereoscopic optical method (3D mark tracking technique): the primary stability of stabilised vertebra and the angular mobility (ROM) of stabilised specimen compared to the initial one.

RESULTS: Fig. 1 shows evolution of strain measured on vertebral bodies of L1 after stabilisation during flexion/extension loading. Strain values remain low (up to 3%) except for one specimen presenting a global deterioration of the quality of bone tissue due to major osteoporosis. Fig. 2 shows ROM values measured on intact and stabilized specimens for flexion/extension loading. Mobility is slightly increased in intervertebral disks around the fractured vertebra but there is no significant difference compared to the mobility measured before fracture.
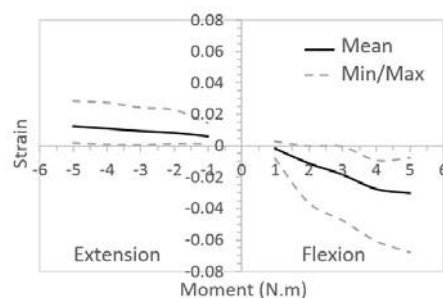

Fig. 1: Evolution of strain of vertebral body of stabilized vertebra (L1) during flexion/extension
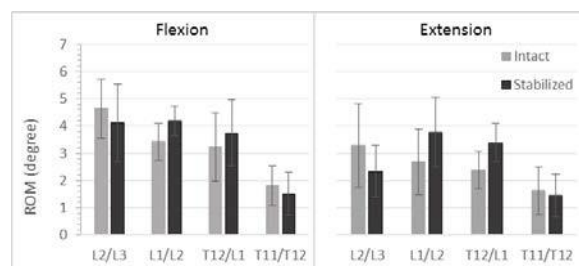

Fig. 2: ROM Values measured on intact and stabilized specimens for flexion/extension loading

DISCUSSION & CONCLUSIONS: Our results suggest that a percutaneous kyphoplasty offers a good primary stability in case of burst fracture. Interestingly, kinematics analysis during physiological movements showed that this stabilization solution preserved disk mobility in each adjacent spinal unit. Further biomechanical studies comparing kyphoplasty alone vs combining kyphoplasty with posterior fusion in this indication would be helpful to find the best compromise in terms of efficacy/invasiveness for our patients.

Segmenting μCT data of in vivo β-TCP scaffolds using active contours algorithm

A Sweedy[1], M Bohner[2], GH van Lenthe[3], G Baroud[1]

[1]Laboratoire de Biomécanique, Université de Sherbrooke, Canada.[2]RMS Foundation, Switzerland

[3]Division of Biomechanics, Mechanical Engineering, K.U. Leuven, Belgium

INTRODUCTION: The focus of this abstract is on accurate segmentation of μCT data of porous β-TCP scaffolds, explanted from sheep. These μCT data have three phases: scaffold remains, bone, and soft tissue. Otsu's algorithm [1] is one of the most commonly used segmentation methods which analyses the gray level histograms to segment the three phases. Segmentation is not evident because these three phases are not always distinguishable. Specifically, the grey level in scaffold remains and new bone exhibit statistical variations, yet locally homogeneous within objects. Consequently, contouring-based methods are hypothesized to be more accurate in segmenting the post-implantation μCT data. We develop a new contouring-based method to accurately segment the three phases and compare the results to histological sections.

METHODS: The Otsu's method [1] uses statistical information from histogram to find the thresholds that maximize inter-class variance defined by Eq.1 [1], to segment and label phases globally.

$$\sigma_B^2 = P_1 P_2 (m_1 - m_2)^2 \qquad (1)$$

Where P_1, m_1 and P_2, m_2 are the probability and intensity mean of classes 1 and 2 respectively. Active contour method uses localized information for segmentation [2]. We start the segmentation process by constructing the initial contour from seeds. The seeds are chosen from the pixels with high gradient values. Using initial contour, we use iterative process to evolve energy-based active contour [2] and find the contour enclosing the objects of the phase of interest, e.g. soft tissue. Such a contour is determined by minimizing the sum energy functions inside and outside the contour, F_1 and F_2 in Eq. 2. Finally, we label the pixels of this phase. In the presented 3 phase case, the segmentation starts by labelling the soft tissue.

$$F_1(C) + F_2(C) = \qquad (2)$$
$$\int_{in} |u_0(x,y) - c_1| dxdy + \int_{out} |u_0(x,y) - c_2| dxdy$$

Where C is the variable curve, $u_0(x, y)$ is the intensity value at (x, y) and c_1, c_2 denote the average energy inside (in) and outside (out) the curve, respectively. The Otsu's and contouring-based methods have been implemented in 3D and applied to 2 samples, each consisting of 600 slices. In addition to visual inspection, the results have been compared to histology sections of the samples.

RESULTS: Fig.1 shows the distinguishable segmented phases resulting from the active contour method (Fig.1 (c)) in comparison with the ones of Otsu's method (Fig.1 (b)).
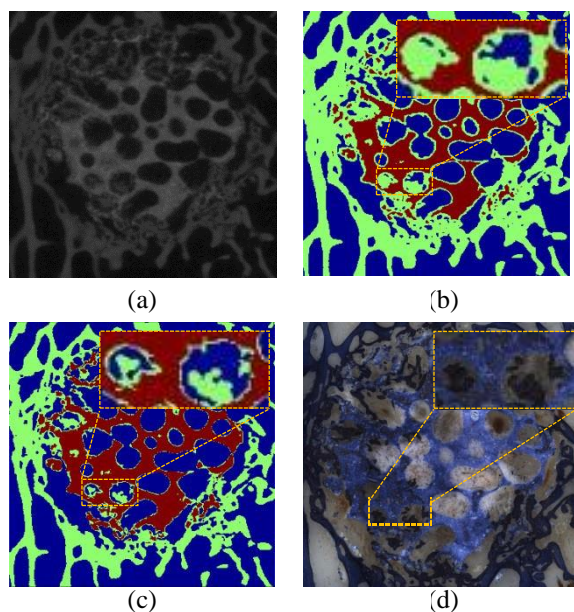

Fig. 1: Slices of (a) original μCT scan, (b) segmentation of same slice using Otsu's method (soft tissue is in blue, bone in light green and scaffold remains in red) (c) segmentation using active contours method and (d) corresponding histological section.

DISCUSSION & CONCLUSIONS: Visual inspection and comparison to histology section show more accurate segmentation using active contours. Compared with Otsu's method, the new approach uses localized information for segmentation. Therefore, it results in an overall better distinguishable phases. Future work will focus on the validation using manual segmentation and integrating the proposed method with other techniques to form a workflow for analysis of in vivo μCT of resorbable β-TCP scaffolds.

Validation of segmentation and alignment algorithm for μCT data of bone substitutes

A Sweedy[1], M Bohner[2], GH van Lenthe[3], G Baroud[1]

[1]Laboratoire de Biomécanique, Université de Sherbrooke, Canada.[2]RMS Foundation, Switzerland,

[3]Division of Biomechanics, Mechanical Engineering, K.U. Leuven, Belgium.

INTRODUCTION: Understanding the biological behavior of porous structured substitutes is of relevance for the design of substitutes and bone healing process. The use of μCT became the norm in studying the explanted bone substitutes [1-2]. However, the μCT data are huge and require an algorithm-based segmentation to differentiate phases found in the substitute. We combine alignment of pre- and post-implantation with contours-based segmentation for accurate algorithm-based segmentation. Little attention in the literature was paid to validating the algorithm-based segmentation, partially because of the labor-intensive validation process. This study is first to validate the μCT segmentation algorithm in resorbable bone substitutes by comparing to operator-based manual segmentation.

METHODS: We use one μCT dataset of explanted β-TCP sample, which consists of 600 slice. Five slices were randomly selected out of the 600 slices. Each slice consists of 445, 440 pixels. For effectiveness, one quarter per slice has been evaluated, 111, 360 pixels per each quarter. This resulted in total of 556, 800 evaluated pixels that were individually and manually inspected for the phases. Specifically, a well-skilled researcher in image processing has segmented them into either bone, scaffold or soft tissue. For comparison, we use the similarity matrix theory (Table 1), in which the diagonal represents the image surface that is in agreement between operator-based and algorithm-based segmentation. In addition, the *dis*-similar surface fraction between phases and methods are shown in corresponding intersection cells (Table 1). Afterwards, we calculate the Dice's similarity coefficient (DSC) for each of the 3 phases (Eq. 1).

$$D_p(P_{0p00}, P_{aaa}) = \frac{2\|P_{oooo} \cap P_{aaa}\|}{\|P_{oooo} + P_{aaa}\|} \qquad (1)$$

Where D_p is the DSC comparing operator P_{op00} and algorithm-based P_{aaa} segmentation results of phase P, *i.e.* bone, scaffold or soft tissue.

RESULTS: Fig. 1 (a) shows a quarter of a μCT slice segmented by the researcher or the algorithm (Fig.1 (b) and (c), respectively). The similarity matrix is in Table. 1. The total similar surface fraction is 94.02 ± 0.79 %, sum of the matrix

diagonal. Dice's similarity coefficients are 92.54 ± 1.08 %, 89.3 ± 2.98 % and 96.31 ± 0.75 % for bone, scaffold and soft tissue, respectively.
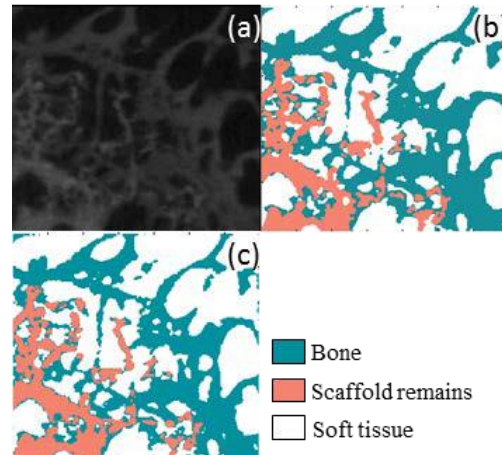

Fig.1: (a) μCT data (b) operator vs. (c) algorithm.

Table 1. Similarity matrix where BSF = bone surface/total surface, SSF=scaffold remains surface/total surface and STSF = soft tissue surface/total surface.

		Algorithm-based			
		BSF (%)	SSF (%)	STSF (%)	Total
Operator-based	BSF (%)	35.49 ±2.80	0.97 ±0.27	1.88 ±0.35	38.33 ±2.38
	SSF (%)	1.43 ±0.25	11.77 ±2.79	0.14 ±0.09	13.34 ±2.89
	STSF (%)	1.42 ±0.91	0.15 ±0.18	46.76 ±4.16	48.33 ±4.30
	Total	38.34 ±3.08	12.89 ±2.53	48.78 ±4.31	

DISCUSSION & CONCLUSIONS: The validation has been laborious and extended over 4 months, yet essential when complex structures and processes are being evaluated. The evaluation showed that the novel segmentation algorithm, based on combining gradient-based segmentation and alignment of pre- and post-implantation μCT data, is sufficiently accurate for use to understand the biological processes and interactions.

Detection of bosonic phase in β-TCP scaffolds based on µCT data

A Sweedy[1], S Jerban[1], M Bohner[2], GH van Lenthe[3], G Baroud[1]

[1]Laboratoire de Biomécanique, Université de Sherbrooke, Canada.[2]RMS Foundation, Switzerland,

[3]Division of Biomechanics, Mechanical Engineering, K.U. Leuven, Belgium

INTRODUCTION: Understanding the new bone deposition in resorbable CaP with high percentage of porosity is of high relevance in orthopaedic procedures. Histological sections of explanted β-TCP scaffolds show a structured deposition of collagen that is likely mineralized in the microporous space of scaffold remains [1]. This structure forms a network in connectivity with new bone deposition. If this structure, to which we refer as bosonic, is mineralized and is new bone we expect that it should be detectable in µCT scans. Complementary to histology, µCT data will provide access to the 3D structure of the bosonic phase. Therefore, the aim of this study is to examine the existence and detectability of high grey level class in µCT, corresponding to the bosonic phase, and its agreement with histology.

METHODS: We use human assisted method to register histological section to the µCT images stack of the same sample. The method comprises the following steps. First, the µCT stack is segmented to the well-known three phases: bone, scaffold remains and soft tissue. Second, visual search is applied to the µCT to determine the approximate location of the histological section. We use the distinctive features including pore structure, bone morphology and geometries in both histology and µCT to match them. Third, the µCT sections that includes the histological one, are subjected to further alignment procedure. Such a procedure includes 3D rotation and affine transformation of µCT combined with visual inspection to verify the section that matches the histological one. The determined scaffold section, that matches the histology section, is subjected to image processing algorithm to find the bosonic phase in it. First, the scaffold remains segmented binary mask $B_{ss}(x.y)$ is weighted using the original µCT scan grey levels $g(x,y)$ (Eq. 1).

$$g_{ss}(x, y) = B_{ss}(x.y) \cdot g(x,y) \qquad (1)$$

Second, Spatial Gaussian filtration and mathematical operations [2] are applied to the resultant grey level image $g_{ss}(x, y)$ to obtain higher contrast. Third, the high contrast slice of scaffold remains is subjected to thresholding operation to be segmented into two sub-phases: scaffold remains and bosonic phase. The connected regions [2] of the bosonic phase are labelled.

Finally, a refinement step is used to the labelled bosonic phase using the statistical mean value within connected regions.

RESULTS: Fig. 1 (a) shows the histological section and Fig. 1 (c) shows the resultant four phases in µCT corresponding to the same phases in histological section: soft tissue, scaffold remains, bone and bosonic phase.
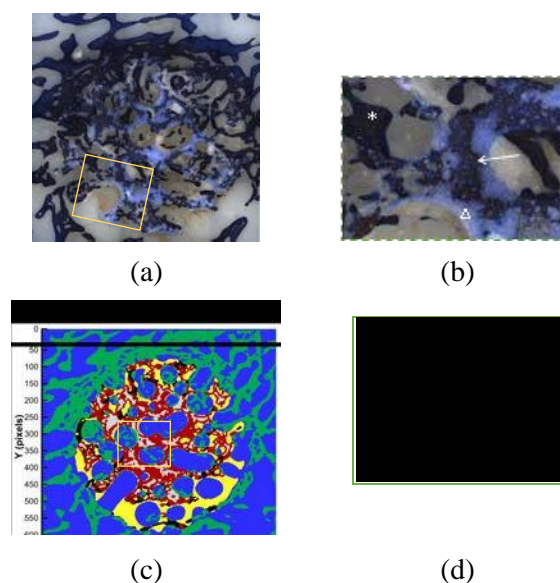

Fig. 1: (a) Histological section after toluidine blue staining (b) magnified part indicated by rectangle in (a) where (Δ) scaffold remains (*) bone and (arrow) bosonic phase, (c) matched segmented µCT slice and magnified in (d) where (blue) soft tissue, (green and black) bone, (red) scaffold remains and (light grey) bosonic phase .

DISCUSSION & CONCLUSIONS: There is a fourth phase (bosonic phase) in µCT. Visual inspection and assessment shows that the detected bosonic phase in both µCT and histological section are in good correlation. The future work will include improvement to the accuracy of the bosonic phase detection. It will also include morphological and quantitative 3D analysis of the bosonic phase.

www.ecmconferences.org

Refining algorithm to better segment edges in low-resolutions scans of resorbable substitutes

A Sweedy[1], S Jerban[1], M Bohner[2], GH van Lenthe[3], G Baroud[1]

[1]Laboratoire de Biomécanique, Université de Sherbrooke, Canada.[2]RMS Foundation, Switzerland,

[3]Division of Biomechanics, Mechanical Engineering, K.U. Leuven, Belgium

INTRODUCTION: Due to the nature of μCT images, they exhibit different level of fuzziness depending on a number of factors [1]. Such factors include scanning resolution, material response to x-ray and voxel size to feature size ratio. Moreover, this level increases dramatically in the case of μCT images of β-TCP in vivo implants. Such implants have a response to x-ray that is similar to bone which results in overlap between grey level histograms of both bone and implant remains. Moreover, the fuzzy edge transition between implant remains and soft tissue results in pixels of grey levels similar to bone. Hence, ordinary segmentation methods label these fuzzy edge transitions as bone. Consequently, the transitions between phases in μCT scans of β-TCP implant should be treated before segmentation to avoid errors in evaluation of in vivo implants. To evaluate a pixel at the transition from one phase to another in μCT images, both grey level of the pixel and position should be considered in the decision process [1]. For example, considering the transition from scaffold to soft tissue, pixels of higher grey level and proximal to scaffold have higher likelihood to be part of the scaffold rather than soft tissue. The aim of this study is to develop a special algorithm to treat the transition between phases in μCT images of β-TCP implant.

METHODS: The algorithm uses two sigmoidal weight functions, one for distance (W_d) and one for grey level values (W_g) (Eq. 1). We use windows to scan the images in the x and y directions. The window size is 1×w and w×1 for x and y-directions, respectively. The w is chosen based on the fuzziness level of the edges. Through scanning, the window are considered to be at the transition from one phase to another if it satisfies following conditions; having pixels of grey level below arbitrary threshold of phase 1 (TH_1) and one pixel that has grey level value greater than arbitrary threshold of phase 2 (TH_2). Afterward, the weighting procedure is applied to the pixels of the window using the distance weight function followed by grey level weight function. The new window is then subjected to thresholding.

$$W_g(p) = A + \begin{cases} 1 & \rightarrow f(p) \geq TH_1 \\ 1 - 2(f(p) - TH_1)^2/(TH_2 - TH_1)^2 & \rightarrow TH_1 \geq f(p) \geq (TH_1 + TH_2)/2 \\ 2(f(p) - TH_2)^2/(TH_2 - TH_1)^2 & \rightarrow (TH_1 + TH_2)/2 \geq f(p) \geq TH_2 \\ 0 & \rightarrow TH_2 \geq f(p) \end{cases} \quad (1)$$

Where *A* is a weighting constant and *f(p)* is the grey value of pixel *p*.

RESULTS: Fig.1 shows segmentation of one of the β-TCP in vivo slices without and with edge treatment.
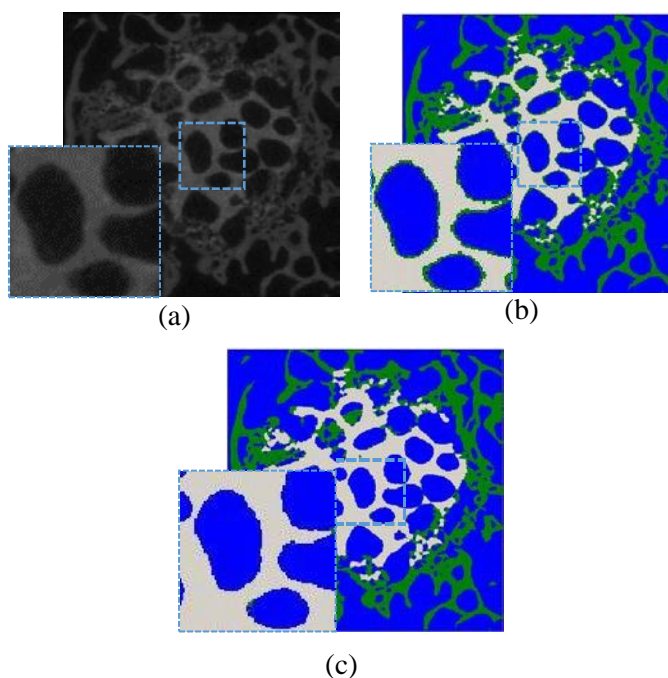

(a) (b)

(c)

Fig. 1: (a) μCT in vivo slice, (b) segmentation without edge treatment and (c) with edge treatment where blue, green and light grey are soft tissue, bone and scaffold remains, respectively.

DISCUSSION & CONCLUSIONS: Visual inspection of the results shows that edge treatment improves the accuracy of segmentation of the transition between phases. Specifically, the segmented image without edge treatment exhibited an erroneous layer of bone deposition at the transitional interface between scaffold and soft tissue. Future work includes verification of results using manually segmented images.

Edge-preserving anisotropic diffusion versus Gaussian filtering for noise reduction in medical images

A Sweedy[1], S Jerban[1], M Bohner[2], GH van Lenthe[3], G Baroud[1]

[1]*Laboratoire de Biomécanique, Université de Sherbrooke, Canada.*[2]*RMS Foundation, Switzerland,*
[3]*Division of Biomechanics, Mechanical Engineering, K.U. Leuven, Belgium.*

INTRODUCTION: Noise is one of the most challenging problems affecting the quality of medical images. Post-acquisition noise reduction methods are commonly used for compensation and reduction of noise levels in medical images. However, most commonly used methods for noise reduction are isotropic statistical-based methods (e.g. mean and Gaussian filtration methods) [1]. Such methods can result in blurring the entire image regardless of the nature or location of the blurred pixels, i.e. edge pixels. The blurring of this critical information can affect the morphometric measurements of structures and objects. Edge-preserving anisotropic diffusion (EPAD) uses the local information (e.g. the gradient) to control the direction and values of pixels blurring [2]. Thus, it introduces a solution for noise reduction while preserving the edge information. Therefore, the aim of this study is to compare the widely used Gaussian filtration and the anisotropic diffusion in terms of accuracy.

METHODS: To compare both algorithms, a synthetic image (199×173 pixels) is used, which consists of white object on black background, mimicking the bone morphology (Fig. 1a). To simulate the scanning noise, Gaussian noise with different variances (0 to 1) is added to the image followed by a fading process. Afterwards, the image is subjected to noise reduction using two methods, Gaussian filtering (size = 3×3 and σ = 0.8) and EPAD. The discrete implementation of the anisotropic diffusion is shown in Fig. 1b where the iterative value of intensity $I_{i,j}^{t+1}$ of pixel (i,j) is calculated by Eq. 1.

$$I_{i,j}^{t+1} = I_{i,j}^t + \lambda[c_N \cdot D_N I + c_S \cdot D_S I + c_E \cdot D_E I + c_W \cdot D_W I]_{i,j}^t \quad (1)$$

Where $D_N I$, $D_S I$, $D_E I$ and $D_W I$ are the difference operators for north, south, east and west, respectively (e.g. $D_N I \equiv I_{i-1,j} - I_{i,j}$). The conduction operators c_N, c_S, c_E and c_W are updated every iteration using the formula (e.g. $c_{N_{i,j}}^t = g(\|(\nabla I)_{i+1/2,j}^t\|))$ where $g(|\nabla I|) = e^{-(\|\nabla I/K\|)^2}$.

Afterwards, the two images are segmented using active contours [3]. The final segmented images are compared with the original synthetic one and the pixel error ratio (PER), which is the ratio of number of erroneous pixels to the total number of pixels in object, is calculated.
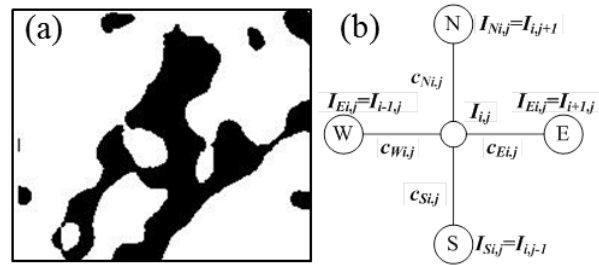

Fig. 1: (a) Synthetic image (b) Numeric representation for EPAD.

RESULTS: Fig. 2 shows a comparison graph of the PER resulting from Gaussian filtering and edge-preserving anisotropic diffusion methods.
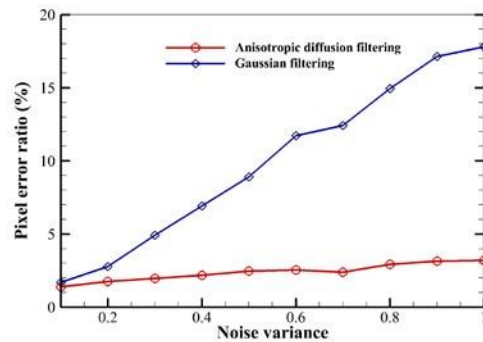

Fig. 2: Comparison of PER results of Gaussian filtering (blue) and EPAD (red) methods.

DISCUSSION & CONCLUSIONS: EPAD showed higher accuracy to isotropic Gaussian filtering in trabeculae analysis. The difference in PER at noise variance of 0.6, which is relevant for trabecular imaging, was 10 % in favor of EPAD. The 10 % error implies a significant error for the microsize analyses. Therefore, we recommend the use of EPAD in the X-ray based scanning techniques applied in trabecular bone and bone substitutes, where edges are crucial for accurate size measurements.

2

The new microconcrete type bone implant materials on the basis of calcium phosphates and chitosan

A Zima, J Czechowska, D Siek, A Ślósarczyk

Faculty of Materials Science and Ceramics, AGH-UST University of Science and Technology, Krakow, Poland

INTRODUCTION: During recent studies in the field of bone substitution, the main attention has been focused on the materials on the basis of inorganic calcium phosphates and organic-biodegradable chitosan (CTS) [1-3]. The aim of our study was to obtain the new microconcrete type implant materials using $\alpha Ca_3(PO_4)_2$ (αTCP) as a binder and hybrid granules: hydroxyapatite (HAp) - chitosan (CTS). The main attention has been focused on determination of factors influencing the physicochemical properties of these materials.

METHODS: The highly reactive α-tricalcium phosphate powder and hybrid HAp/CST composites were synthesized by the wet chemical method. As the liquid phases methylcellulose or chitosan solutions were used. The physicochemical properties of the obtained composite hybrid materials such as: phase composition (XRD, D-2 Phaser, Bruker), FTIR analysis (Vertex 70&70v, Bruker), porosity (MIP, Auto Pore IV, Micromeritics), microstructure (SEM) and compressive strength (Universal testing machine, Instron) were determined. The chemical stability *in vitro* was evaluated by the measurements of changes in pH of simulated body fluid (SBF) and ionic conductivity of distilled water during the samples incubation at 37°C (Pol-Eko).

RESULTS: XRD studies confirmed that it was possible to introduce chitosan into the structure of hydroxyapatite via the wet chemical synthesis. Introduction of chitosan during the synthesis did not cause the decomposition of hydroxyapatite (Fig.1). FTIR analysis of HAp/CTS composites, confirmed the presence of functional groups characteristic for hydroxyapatite and chitosan (Fig.2).
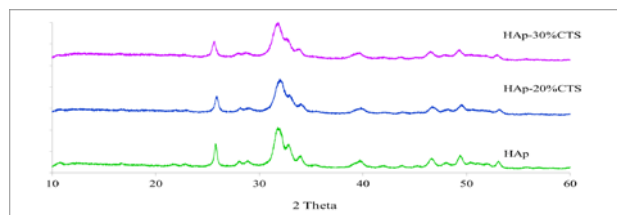

Fig. 1: *X-ray diffractograms of the undoped hydroxyapatite and chitosan doped hydroxyapatite*
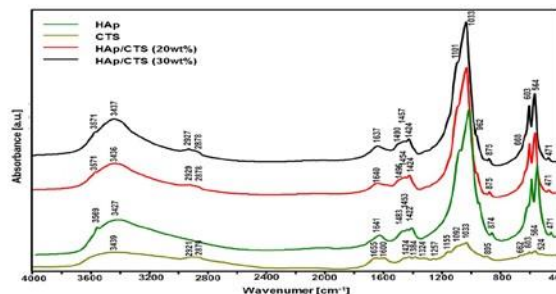

Fig. 2: *FTIR spectra of chitosan, hydroxyapatite and HAp/CTS composites*

The HAp/CTS composites with 20wt%. or 30wt% of chitosan content resulted in approximately 12-16 fold increase in the compressive strength as compared to the unmodified HAp material. Results of SEM observations demonstrated that the applied preparation method allowed obtaining composite materials with homogeneous microstructure. The open porosity of the final microconcretes was equal ~50.0 vol %. Microscopic observations after incubation in SBF confirmed the bioactive potential of the developed materials. The obtained hybrid composites had a high chemical stability. After 28 days of incubation in SBF, pH of the solution around the samples remained close to the biological conditions (7.2-7.4).

DISCUSSION & CONCLUSIONS: The coprecipitation method used to prepare the HAp/CTS granules resulted in the desired microstructure and good mechanical properties. Obtained microconcretes composed of highly reactive, monophasic αTCP powder allowed for a good adhesion of the continuous cement phase to the surface of the HAp/CTS granules. These perspective implant materials, with the qualities, which possess neither the sintered ceramics nor bone cements themselves, require further research.

Injectable hydrogels based on elastin-like recombinamers as scaffolds for regeneration of osteochondral defects

A Girotti[1], I Gonzalez de Torre[1, 2], M Alonso[1], J Arias[1], JC Rodríguez Cabello[1], J Blanco[4], D Pescador[4], F Martín Sanchez-Guijo[3], C Del Cañizo[3], S Muntión[3], S Carrancio[3]

[1] BIOFORGE, CIBER-BBN, University of Valladolid, Spain, [2] Technical Proteins NBT S.L. Valladolid, Spain [3] Servicio de Hematología clínica University of Salamanca, Spain [4] Departmento de Cirugía, University of Salamanca, Spain

INTRODUCTION: Articular cartilage is a structure with limited regenerative capacity whose lesions have a complex management. Multiple treatments have been proposed, *e.g.* reparative and regenerative substitutes, but none of these have achieved an adequate regeneration of hyaline cartilage [1-3]. With the emergence of cellular therapy, MSCs and their combination with highly specialized biomaterials opens a great hope to achieve a perfect regeneration. Elastin-Like Recombinamers (ELRs) are tailored recombinant polymers, totally biocompatible, elastic, with thermoresponsive behaviour. Furthermore, ELRs can be functionalized with specific sequences to achieve desired biological properties. Gel formation can be carried out *in situ* under physiological conditions with a completely cell friendly process.

METHODS: An animal xenograft model was performed in 6 rabbits. An osteochondral defect was practiced at the knees of rabbit. MSCs were embedded into an ELR solution that was injected directly in the defect area in the knees of the rabbits. A rapid gelation process drove to a total cytocompatible hydrogel. Results were evaluated by histological stain, immunohistochemistry, NMR and 3D CT (Fig. 1). The regeneration of the lesion was evaluated using the modified scale of Wakitani.

RESULTS: Radiological and NMR analysis of the experimental group, indicated a complete regeneration of articular cartilage and integration of the adjacent cartilage was observed. 3D CT revealed subchondral bone regeneration. Histological stain and immunohistochemistry showed articular cartilage regeneration in all layers and at the beginning of the subchondral bone, regardless of the human MSCs. These were not observed in the control group. Modified Wakitani scale was statistically significant between the control and the ERL group with 5.6 *vs* 13.5 points, respectively.

DISCUSSION & CONCLUSIONS: ELRs based hydrogels used in the study were easy handled, easily applied by injection in liquid form, and solidified on contact with living tissue.
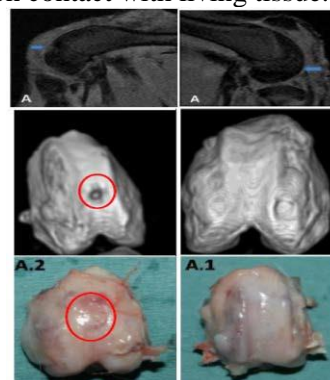

Fig. 1: Images of NMR, 3D CT and macroscopic observation (top, medium and bottom row respectively) of left knees treated with ELR hydrogel (left column) and right knees treated with hydrogel with hMSCs (right column).

hMSCs were embedded in the hydrogel and delivered at the site of the lesion. Radiological evaluation revealed that the knees treated with hydrogel and cells exhibit a more like uninjured image than the knees treated without cells. Histology indicated obvious signs of tissue regeneration for cartilage and bone for knees treated with the ELR-hydrogel and cells. The use of MSCs with an ELR based hydrogel was able to regenerate osteochondral lesions in animal models.

Modification of chitosan hydrogel structure after mineralization by sorption for application as a scaffold for bone regeneration

AL Skwarczynska[1], Z Modrzejewska[2], TEL Douglas[3]

[1] Department of Civil Environmental Engineering and Architecture, Rzeszow University of Technology, Powstancow Warszawy 6, 35-959 Rzeszow, Poland. [2] Department of Environmental Systems Engineering, Faculty of Process and Environmental Engineering, Technical University of Lodz, Wolczanska 213, 90-924 Łodz, Poland. [3] Nano and Biophotonics group, Department of Molecular Biotechnology, Ghent University, Coupure Links 653, 9000 Gent, Belgium.

INTRODUCTION: Here, structural studies of modification chitosan hydrogels produced by using sodium beta-glycerophosphate (Na-β-GP) as a neutralizing agent [1-4] (their sol-gel transition occurs at physiological) after mineralization by sorption. The mineralization was conducted due to the fact that phosphorus is present in the structure of chitosan hydrogels, which alters the nature and properties of the adsorbent. In order to obtain - in the structure of gels - compounds similar to the hydroxyapatites present naturally in bone tissue, gels were modified in pH 7 phosphate buffer after sorption.

METHODS: Thermosensitive chitosan gels were prepared according to the method described by Chenite.[1] Shrimp chitosan (Sigma Aldrich) of degree of deacetylation SD ~ 79.5%, and molecular weight 86 kD was used. In the first stage, the hydrogels were incubated in $CaCl_2$ solutions of different Ca concentrations. In the second stage, to produce the compounds of calcium and phosphorus in the chitosan gel structure, after adsorption the gels were modified by placing them in pH 7 buffer.

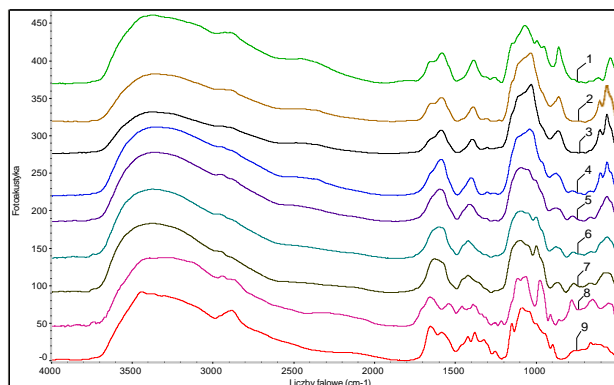**RESULTS:** Post-adsorption changes in structure of gels were seen by FTIR and XRD (Fig. 1 and 2).

Fig. 1: FTIR spectra after adsorption in: 1 - 2.5; 2 – 10; 3 – 20; 4 – 50; 5 – 70; 6 – 80; 7 - 90 g_{Ca}/dm^3 and modification at pH 7, 8 - hydrogel after preparation, 9 - chitosan.
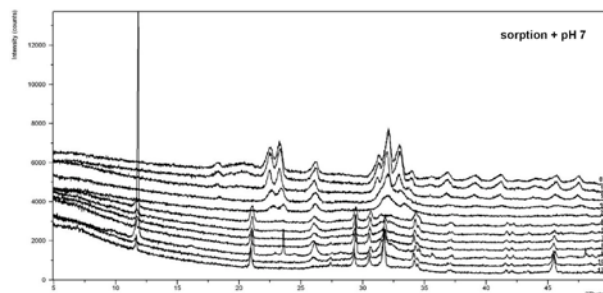

Fig. 2: XRD of gels after sorption of Ca at 0-120 g_{Ca}/dm^3 and modification in pH 7.

DISCUSSION & CONCLUSIONS: After the modification in pH 7 buffer maxima were observed at wavenumbers of approximately 1000 cm^{-1} and 980 cm^{-1}. A band was clearly seen at 860 cm^{-1} which is most likely related to orthophosphates (PO_4^{3-}), because they correspond to the stretching vibrations (ν_{PO_2}). It may also indicate the presence of carbonates (CO_3^{2-}) and hydrogen orthophosphates (HPO_4^{2-}). In both cases wide bands 550-700 cm^{-1} are also present which confirms the presence of orthophosphates (PO_4^{3-}). The identification of the peaks in diffractograms indicates that compounds of calcium and phosphorus are present in the structure. In the case of sorption from the concentrations up to $20 g_{Ca}/dm^3$, clear peaks are present at 2θ 30-35°. In the case of sorption from high concentrations of the adsorbed substance, this peak was shifted towards lower angles $2\theta = 29$-32°, typical for hydroxyapatite.

.

Study of thermomechanical bone fillers during polymerization and loading

C Brèque[1, 2], A. Planty[1], S Teyssédou1[3], F. Hesser[2], JC Dupré[2], T. Vendeuvre[1, 3]

[1] *Laboratory of Anatomy, Faculty of Medicine and Pharmacy, University of Poitiers, France.*

[2] *P'institute, CNRS 3346, Futuroscope Chasseneuil, France .*[3] *Department of Orthopaedic Surgery and Traumatology, CHU of Poitiers, France.*

INTRODUCTION: Bone fillers are numerous in the clinical area. We therefore investigated the thermomechanical behavior of polymethyl methacrylate (PMMA) and calcium phosphate (CaP) cements with no conflict of interest. The aim is thus to determine their peak temperatures during their polymerization, their thermal expansion coefficients as well as their mechanical properties: tensile strength (σ_{rupt}) and elasticity module (*E*). All these mechanical parameters should be able to guide the surgeons in their operative procedure.

METHODS: We have established seven groups of 4 specimens each. Each group corresponds to a type sold cements. We tested four PMMA and two CaP cements. The test pieces were conducted by injecting cement into 4 cm^3 glass tubes of 8 mm of internal diameter. The temperature was measured using an infrared camera. The thermal expansion coefficient was determined by using an optical extensometer and by placing the tubes in a heating chamber applying a temperature rise from 30° to 100°. The mechanical characteristics were determined by a compression test performed using a machine coupled to an optical extensometer.

RESULTS: The parameters of the study are presented in Tables 1, 2 and 3.

Table 1. Average temperature peaks.

	temperature peaks (°C)	peaks time (min)
Zimmer	62.3	25.6
Biomet	64.5	23.6
Synthes	51.1	61.4
XPede	62.7	25.8
HVR	56.5	26
Kyphos	no peaks	no peaks
Inflate	no peaks	no peaks

DISCUSSION & CONCLUSIONS: Temperature peaks due to the polymerization can reach 65°C between 23.6 min and 61.4 min. This may, in some cases, injured adjacent tissues. The coefficient of expansion is negligible for an injected volume of 4 cm3 (Ø 9.8 mm), the maximum shrinkage due to cooling would be 0.6 µm on the diameter. PMMA

cement is 4 times stronger than calcium phosphate, but has less elasticity. We also observed a higher standard deviation on calcium and phosphate, which can lead us to assume that the cement structure depends of the method of injection. The calcium phosphate cement has the advantage of promoting bone growth with a lesser load, unlike the PMMA. Nevertheless, for a revision surgery, the breaking stress for PMMA still remains lower in cortical bone (84±7 N/mm²) [1].

Table 2. Average thermal expansion coefficient.

	(°C^{-1})
Zimmer	3.41e-5
Biomet	7.05e-5
Synthes	4.47e-5
XPede	4.08e-5
HVR	7.73e-5
Kyphos	6.85e-6
Inflate	4.37e-5

Table 3. Average mechanical properties.

	σ_{rupt} (N/mm²)	*E* (N/mm²)
Zimmer	79 ± 7%	2011 ± 10%
Biomet	75 ± 8%	2163 ± 5%
Synthes	54 ± 10%	2162 ± 27%
XPed	65 ± 7%	2146 ± 3%
HVR	60 ± 10	1853 ± 6
Kyphos	15 ± 42%	3139 ± 50%
Inflate	15 ± 20%	3184 ± 49

Cement injection control improvement with simultaneous aspiration to improve safety

C Lambert [1], S Becker[2], G Baroud[1]

[1]Laboratoire de Biomécanique, Université de Sherbrooke, Canada. [2]IMSART, Austria.

INTRODUCTION: Extravertebral cement leakage and the displaced soft tissue from within the trabecular bone are reported to cause cascade of ischemic crisis related to the pulmonary emboli [1-3]. A novel delivery device is designed integrating aspiration in order to help exert control on the cement filling, and evacuate the displaced tissues.

METHODS: The cannula features a double conduit: the inner tube for the cement delivery, and the outer tube to connect the aspiration device through a lateral port. The mechatronically assisted aspiration is triggered by the physician, and delivers slight vacuum pressure, which is recorded and acquired on a software interface. The effectiveness of the aspiration is controlled with the vacuum pressure and the aspirate volume compared with the simultaneously injected cement volume.

RESULTS: The use of a 30mL syringe to generate negative pressure in a variable closed volume (depending on plastic pressure line connection length) containing air is shown in Fig.1. Considering a previous study wherein 90 kPa vacuum pressure resulted in a significant control of the cement filling [3], we confidently foresee the syringe as an efficient device for the aspiration.
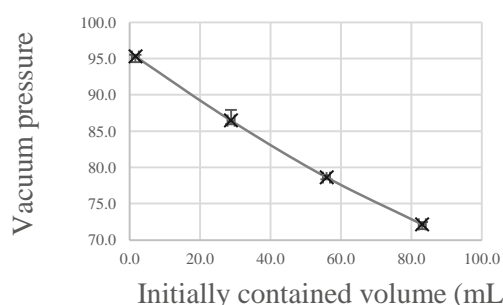

Figure 1 - Vacuum pressure created within a syringe with a pressure line extension.

DISCUSSION & CONCLUSIONS: An experimental setting is to be built in order to verify the following mandatory requirements for the process evolution acceptance as a new standard in the bone augmentation field: The physician-driven device must require no additional staff, nor additional training for the surgeon. The device with integrated aspiration should not modify the current injection process. And, the aspiration control must be instinctive. The additional apparatus must integrate well, be miniature, not bulky, and be consistent with a sterile environment. It should be compatible with FDA requirements.
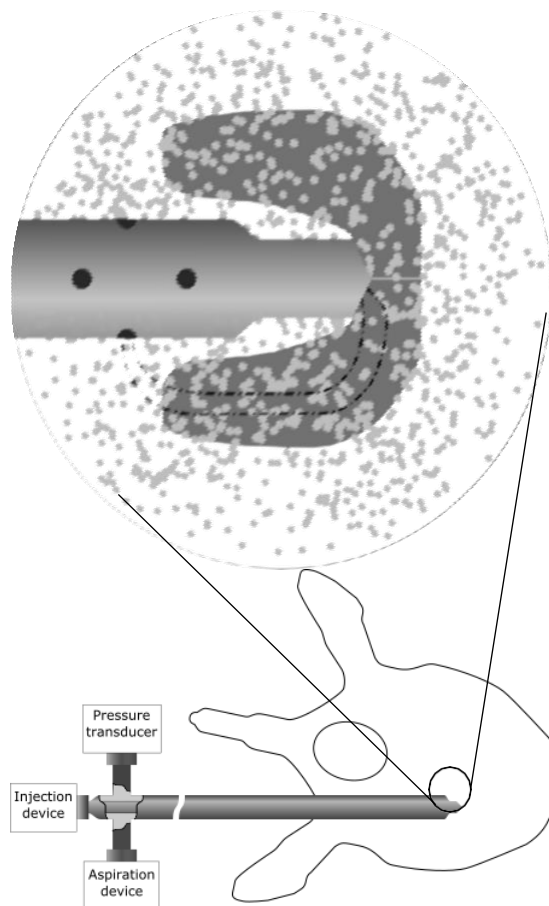

Figure 2 - Cement spreading pattern within the vertebral trabecular bone under the influence of a gradient of pressure (dash line) applied thanks to the aspiration

al (2007) *Anesthesiology* **107(1)**:75-81. [3] R. Mohamed, C. Silbermann, A. Ahmari et al (2010) *Spine* **35(3)**:353-60.

Energy dispersive compositional analyses of newly formed bone in micro- and macroporous resorbable bone substitutes

G Baroud[1], S Jerban[1], A Sweedy[1], L Galea[2], M Bohner[2]

[1]*Laboratoire de Biomécanique, Université de Sherbrooke, Canada.* [2]*RMS Foundation, Switzerland.*

INTRODUCTION: Calcium-phosphate bone substitutes (BS) with a high percentage of both micro- and macro-porosity are used to promote bone formation in critical size defects in bone. BS biopsies, at 6 weeks, for histology [1], regular and back-scattered scanning electron microscope (SEM) images, and Energy Dispersive X-ray (EDX) analyses revealed a new growth to the surface of macro-pores and into the micro-pores of the scaffolds. The measurements of 2D biopsy are used and the findings are integrated to determine the nature of the new tissue growths.

METHODS: To segment the biopsy image after Toluidine blue staining, $C_{15}H_{16}ClN_3S$ (Fig.1a), we developed a segmentation algorithm that uses color-segmentation combined with a decision criterion based on corresponding regular and back-scattered SEM images (Fig.1b,c). Firstly, a human-assisted algorithm is used to register the SEM images to the image biopsy section. Secondly, based on the color, luminosity and the SEM observations in biopsy section, five different phases are classified; (i) the densified, referred to as bosonic region (Blue and dark in biopsy and observable in regular SEM), (ii) bone (Blue and dark in biopsy while not observable in regular SEM), (iii) BS remains (Blue and bright in biopsy and observable in both regular and back-scattered SEMs), (iv) resorbed BS (Blue and bright in biopsy and observable in regular SEM despite the back-scattered SEM), and (v) soft tissue (Not blue in biopsy). Afterwards, the EDX image is registered to the segmentation results using the same human-assisted algorithm to study the mineral compositions of the described phases. Particularly, calcium, phosphorus, sulfur and nitrogen contents are analyzed in the stained biopsy section.

RESULTS: Aligning the Toluidine blue staining $C_{15}H_{16}ClN_3S$ image of biopsy section (Fig. 1a) and SEM (Fig. 1b,c) images allowed segmentation into defined five phases (Fig. 1d). Both the back-scattered SEM (Fig.1c) and EDX analyses (Fig. 1e, f) showed higher mineralization degree in the bosonic phases. EDX indicates collagen deposition into the bosonic zones and the bone mineralization front, as indicated on the sulfur and nitrogen maps (Fig.1g, h).
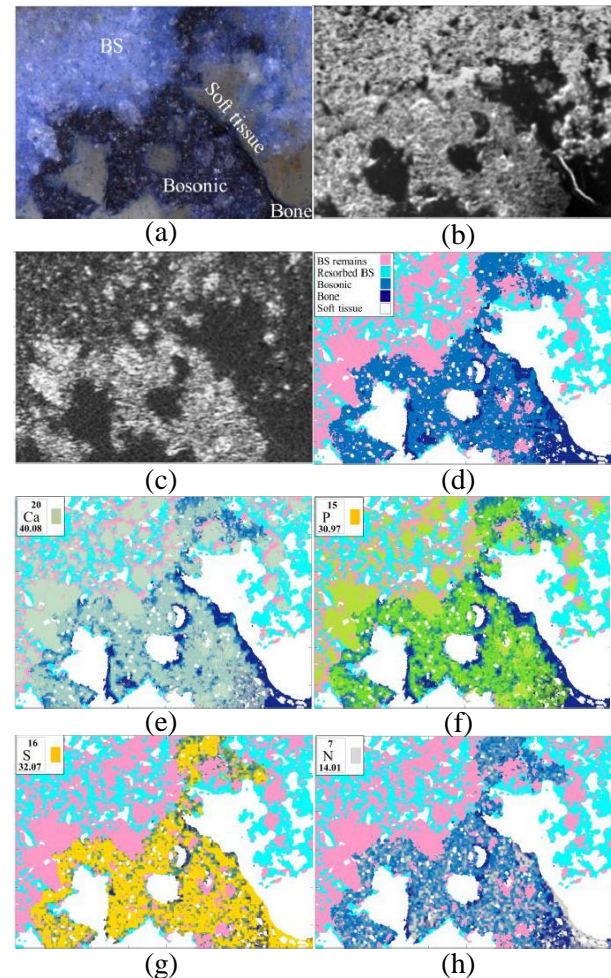

Fig. 1: (a) Biopsy section stained with Toluidine blue and corresponding (b) regular and (c) back-scattered SEMs, (d) Segmented biopsy image. (e) Calcium, (f) phosphorus, (g) sulfur and (h) nitrogen traces from EDX on segmented biopsy.

DISCUSSION & CONCLUSIONS: Toluidine blue attaches to polyanionic group of collagen found in the mineralized bosonic phase and in the unmineralized, apparently organic portion of an osteoid front that forms prior to the bone tissue maturation. The bosonic zones appear globally to form a well-defined microstructure that connects to host bone. This combined finding suggests that the bosonic zones and osteoid are a part of the new bone maturation process.

Production of β-TCP platelets with controllable geometry in organic media

J Thüring[1,2], C Stähli[1], L Galea[1], N Döbelin[1], M Bohner[1]

[1]*RMS Foundation, Bettlach, Switzerland.* [2]*ETHZ, Department of Materials, Zürich, Switzerland.*

INTRODUCTION: Sub-micrometric bioceramic particles are of great interest for injectable bone cements, for 3D printing applications and as fillers of composite materials. Nano-structured composites can potentially combine high tensile strength and toughness and may thus offer bone substitute materials for load bearing sites. Hexagonal non-agglomerated β-tricalcium phosphate (TCP) platelets with a thickness of ~ 150 nm and aspect ratios of up to 15 were recently produced through precipitation in ethylene glycol [1]. However, the ideal platelet geometry for maximum mechanical properties is close to 28 as shown by theoretical calculations (for platelets with thickness < 350 nm embedded in a chitosan matrix) [1]. Therefore, the aim of the present study is to investigate reaction conditions allowing obtaining aspect ratios close or superior to 28.

METHODS: Based on a recent observation that the aspect ratio can be controlled through the reagent pH a systematic study was performed by varying the NaOH concentration [2]. In order to increase the sample production rate, a continuous reactor was designed where a $CaCl_2$-ethylene glycol solution and a H_3PO_4-NaOH-ethylene glycol solution were pumped through separate tubes at 90°C and subsequently mixed and kept at 150° to allow for precipitation and particle growth. The geometry and composition of the resulting particles were analysed by scanning electron microscopy (SEM) and x-ray diffraction (XRD) and the latter results were quantified by Rietveld refinement analysis.

RESULTS: Lowering the NaOH concentration in the reactor from 32 to 24 mM resulted in an increase in diameter of β-TCP platelets from 0.8 to 1.9 µm and an increase in aspect ratio from 6 to 26 (Fig. 1), with a size dispersion between 0.1 and 0.3. However, the precipitated material contained other phases including anhydrous dicalcium phosphate (DCPA, $CaHPO_4$) and hydroxyapatite (HA, $Ca_5(PO_4)_3OH$), as demonstrated by XRD analysis. Moreover, the amount of phases other than β-TCP increased with lower NaOH concentration. Specifically, at 24.2 mM NaOH, the sample was composed of approximately 80 % β-TCP and 20 % DCPA while at higher NaOH concentrations more than 96 % β-TCP was obtained.
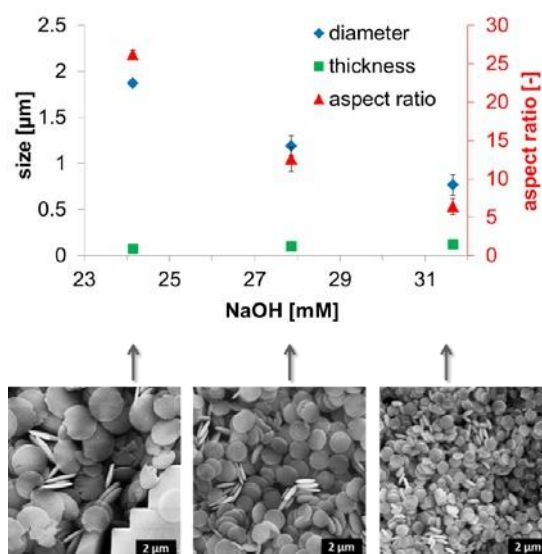

Fig. 1: Influence of NaOH on the geometry of β-TCP platelets produced in a continuous reactor.

DISCUSSION & CONCLUSIONS: By reducing the NaOH concentration, β-TCP platelets with a promising aspect ratio for composite mechanical properties could be synthesized. However, the same parameters led to the precipitation of other phases. In comparison to a batch reactor, where larger volumes of solution were mixed at once, much higher aspect ratios and lower undesired phases were obtained at the same conditions in the present continuous reactor. In order to obtain more pure β-TCP platelets, future work will focus on examining the effect of the reactor type, or mixing conditions, on platelet composition and geometry. In particular, additional experiments will be carried out in order to elucidate the sequence of precipitation of the different phases.

In conclusion, non-agglomerated sub-micrometric β-TCP particles were produced with controllable geometries and a narrow size distribution. These properties may be beneficial for load-bearing composite materials as well as to improve the mechanical properties or the flowability of calcium phosphate pastes.

Salvage Solution for Intractable Distal Femoral Non-union after 12 Surgeries in the Setting of Osteosarcoma Resection

JC Villa, J Moya-Angeler, L Zambrana, A Gianakos, JM Lane

Hospital for Special Surgery, New York, NY 10021

INTRODUCTION: Localized osteosarcoma of the distal femur in young patients treated with a combination of chemotherapy and tumor resection has been associated with long term survival and cure rates between 60% and 80% [1]. After resection, prosthetic or allograft reconstruction has become the standard of care achieving a viable and functional extremity. Allografts however have a high incidence of delayed union or nonunion that predisposes patients to subsequent fracture, infection, and hardware failure at the allograft-host bone junction. This report illustrates the unique case of a young patient who presented with a distal femoral nonunion resistant to multiple previous standard surgeries ultimately requiring a distal femoral replacement TKA.

CASE DESCRIPTION: A 54 year old male presented with persistent left knee pain (5/10) and severe functional limitation. He presented with an extensive past medical and surgical history significant for osteosarcoma of the left distal femur, treated with chemotherapy, surgical resection, and an intercalary graft in 1991. This was complicated by a nonunion treated with a vascularized fibula graft in 1993 followed by a nail change and angled blade plating in 1994. During the next five consecutive years, he underwent two bone grafts and three stem cell implantations. In 2008, he underwent a Hernigou (bone concentrated demineralized bone matrix) procedure for the same previous non-union. The lateral plate broke in 2009, which required a new intramedullary nail and an autogenous bone graft. This was complicated with slow healing and knee pain that required another Hernigou procedure. In 2013, the patient presented with a left tibial plateau fracture Schatzker VI that was treated with ORIF. He has been on pain until this visit. The most recent X-rays and MRI confirmed a nonunion of the distal femur with a broken intramedullary nail and the patient was requested definitive treatment. Subsequently we removed all the hardware material (broken femoral nail, wires and plates in the femur and tibia) and implanted a cemented total distal femoral prosthesis with long intramedullary stem along with a tibial component (Fig. 1). Patient regained alignment and restored equal length. Four weeks after the surgery patient denies pain, is walking with the aid of crutches and
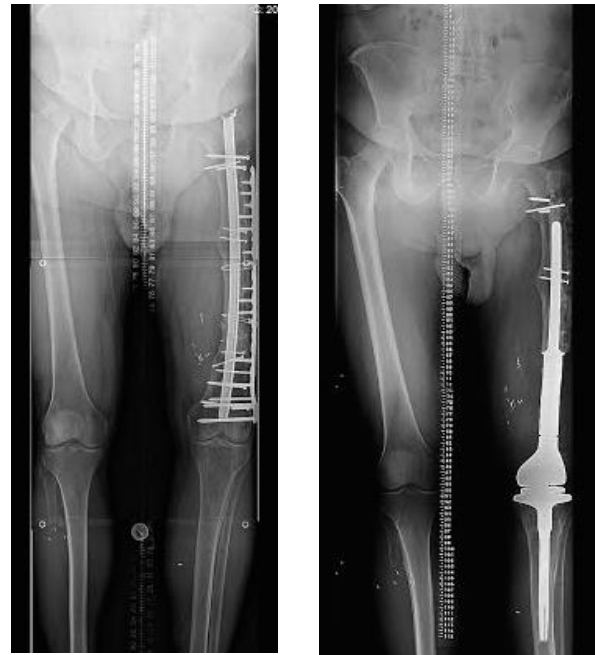
has a ROM of 90° in flexion and 0° in extension.

Fig. 1: X-Ray image of the patient showing the lateral plate (left) and the total distal femoral prosthesis *(right).*

DISCUSSION & CONCLUSIONS: Despite many options to treat nonunion, absolute indications for each have not been established. Distal femoral endoprosthesis or megaprosthesis has been used to treat persistent non-union of distal femoral fractures in elderly and as limb salvage for tumors but there are not reported cases of its used in younger patients after osteosarcoma resection and multiple surgeries [2]. It has the advantage of being expeditious, allowing rapid weight bearing and immediate functional restoration, but carry limited revision options when a prosthetic failure occurs. Long-term durability is a concern.

Verification of the image-based deformation measurement method, Digital Image Correlation (DIC) for rigid body rotation

J Zhang, G Baroud

Laboratoire de Biomécanique, Faculté de Génie, Université de Sherbrooke, Canada

INTRODUCTION: The accurate image-based mechanical properties measurement of PMMA bone cement is of great importance for the bone augmentation procedures. The DIC [1-2] is an image-based method for accurate deformation measurement. It has great advantages including contactless, simple setup, high accuracy and non-limited repeatability in subjectively selected regions of interest. In DIC algorithm, a pair of images is captured before and after deformation and correlated to determine the displacement. Then a set of pixels of interest (POI) in 1st image is identified. In the 2nd image, the approximate location of the second set of pixels containing the POI is determined using neighbourhood-based search algorithm. A correlation coefficient of the two sets of pixels is calculated. An iterative process is applied to find the accurate location of the POI by maximizing the calculated correlation coefficients. Accordingly, the displacement and subsequently deformations at the POI can be calculated. The aim of this study is to examine the accuracy of the DIC algorithm for rigid body rotation using computer-generated images.

METHODS: Ten pairs of images (256×256 pixels) are generated using the algorithm based on Zhou's study [3]. Rotation angles ranging from $0.5°$ to $5°$ (the increment is $0.5°$) are applied to 2nd image of each pair. Each pair (e.g. Fig.1) is used as the input of DIC algorithm. For the sake of computation cost, a total number of POIs (N=9) are selected in the 1st image of each pair. The displacement vector (u, v) and its gradients $(\partial u/\partial x, \partial u/\partial y, \partial v/\partial x, \partial v/\partial y)$ are then calculated using the DIC algorithm. Thereafter, the rotation angle is calculated using Eq.1. Afterwards, the accuracy of algorithm is evaluated using the mean angle θ and errors of calculated rotation angle of all POIs.

$$\theta = (\partial u/\partial y - \partial v/\partial x)/2 \qquad (1)$$

RESULTS: Fig. 2 shows the comparison between calculated angles (y axis) from DIC algorithm and originally imposed angles (x axis). The small chart indicates relative error.
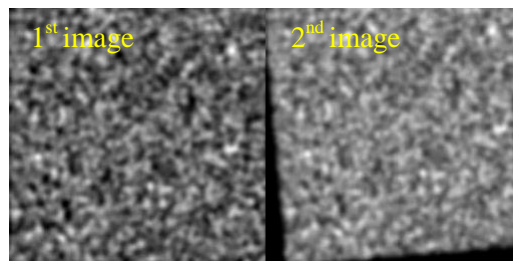

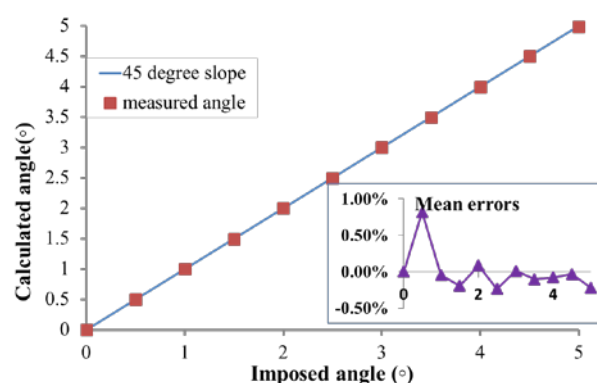*Fig. 1: A pair of generated images (at $5°$).*

Fig. 2: Rotation angles and errors (small graph) of calculated and imposed values.

DISCUSSION & CONCLUSIONS: All of calculated angles perfectly fell on the $45°$ fitting line. Precisely, the error of the calculated angles was within a range of 0.0084 % ~ 0.81 %. This resulted from the convergence criterion of the algorithm to control the absolute error under a certain value (1 %). The only outlier error point had the highest relative error of 0.81 % at $0.5°$. Yet, it was very low and acceptable. In conclusion, the accuracy and robustness of our DIC code has been verified. Moreover, higher accuracy is achieved with more POIs computed and lower convergence limit.

Comparison between subpixel displacement and integer displacement estimation in the DIC algorithm

J Zhang, G Baroud

Laboratoire de Biomécanique, Faculté de Génie, Université de Sherbrooke, Canada

INTRODUCTION: Image-based methods are efficient in engineering and medical fields. In medical field, it greatly facilitated the diagnosis of the objects of interest in a more quantitative way. Precisely monitoring the relative location change of specific organ or objects from medical images is often necessary in pathological analysis (e.g. breast tumour analysis [1]). Currently, algorithms for obtaining the deformation are limited by the pixel size as it is the smallest measuring unit in images. Thus the size of pixel determines the accuracy of the deformation measurement [2]. Deformation takes, however, place at the subpixel scale. The information of these locations cannot be known because of the nature of discrete images. Therefore, a method that enables sub-pixel displacement detection became of quite necessity. Thus, this study compares the accuracy of measuring the displacement using the integer discrete pixel field versus a sub-pixel continuous interpolation.

METHODS: A pair of computer-generated image (256×256 pixels) is used as the input images. To simulate the deformation, a rotation angle of $1°$ is applied to 2nd image. A region of interest (ROI) is selected and 961 uniformly distributed POIs with a step of 5 pixels are tracked to represent the deformed field. An algorithm using the basic full-field search is applied to calculate the integer displacement field of the ROI. Another advanced algorithm using Newton's method combined with the bicubic spline interpolation is used to find the sub-pixel displacement field. Afterwards, the two displacement fields are compared for accuracy.

RESULTS: The two displacement fields of the ROI from two algorithms using integer pixel level versus sub-pixel level are demonstrated in Fig.1a and b, respectively. The mean error in displacements (u, v) is -0.0358 pixels, 0.0229 pixels for the discrete algorithm in the u and v directions, respectively. Further, the subpixel level algorithm (Fig.1b) provides a rotation field with mean error of -8.5551e-04 and -5.1109e-04 pixels in u and v, respectively.

DISCUSSION & CONCLUSIONS: The integer level algorithm determines displacement vectors with same rotation direction as applied, yet it did exhibit neither continuity nor uniformity of the displacement field. The comparison demonstrated the advantage of sub-pixel interpolation for images even with a small rotation angle of $1°$. The sub-pixel level algorithm has a remarkably low error as low as 0.00086 pixel while integer pixel level one has 40 times bigger error with the same input. Evidently, the subpixel algorithm is preferable in accurate deformation detections especially in medical image processing.
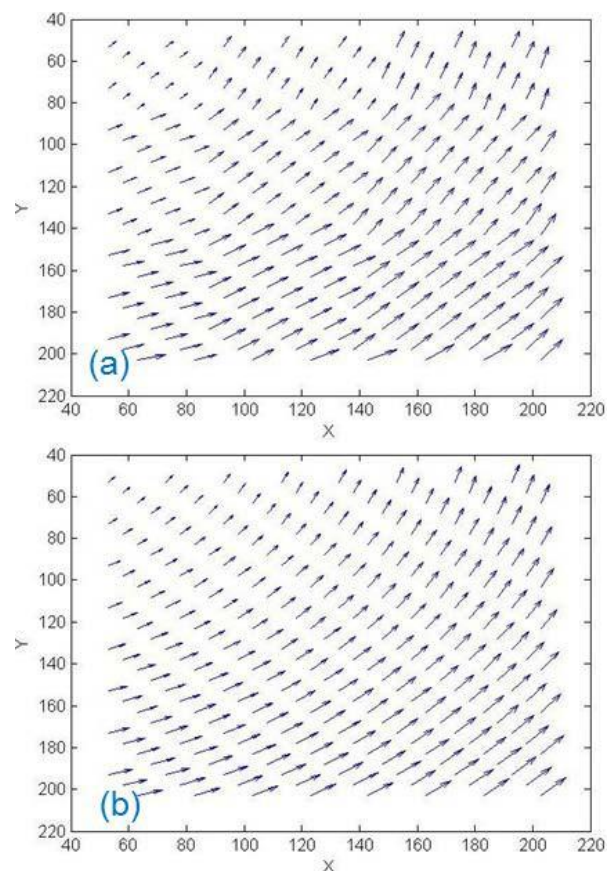

Fig. 1: Obtained displacement fields from two algorithms: (a) integer level; (b) subpixel level.

www.ecmconferences.org

The effect of speckle patterns on the accuracy of deformation measurement in DIC method

J Zhang, G Baroud

Laboratoire de Biomécanique, Faculté de Génie, Université de Sherbrooke, Canada

INTRODUCTION: In deformation measurement of PMMA bone cement using image-based Digital Image Correlation (DIC), many factors can affect the accuracy. Speckle pattern was found to be an important factor for the efficiency and accuracy of DIC [1]. Such a pattern could be the surface appearance of natural or artificial objects. From the DIC calculation point of view, an optimum speckle pattern should satisfy high accuracy and reproducibility. In related studies, speckle patterns were characterized using speckle size, grey level histogram and gradients and so forth [1]. For instance, optimum speckle size of 2~5 pixels and a histogram with good contrast resulted in high accuracy [1]. In addition, post-acquisition methods were also proposed, such as increasing the image sharpness [2]. Therefore, this study investigates the effect of five speckle patterns on the accuracy of DIC measurement.

METHODS: Three speckle patterns are created experimentally by spraying two layers of white and black paint on three PMMA specimens surface. The painted area (347×347 pixels, pixel size=15 micron) is then photographed by high resolution camera (Imitech 1394, 1200×1600 pixels). The obtained speckle images are shown in Fig. 1 (A, B and C). Then sharpening process is used to generate images *B** and *C** from images *B* and *C*, respectively. Histograms of all five images are plotted. Next, all five images are artificially rotated by 5° counter-clockwise to form deformed images. For computational economy, 5 pixels of interests (POIs) in each of the five original images are selected and calculated for rotation angles using the in-house DIC algorithm. Mean values and errors are used to examine the effect of different patterns on the accuracy.

RESULTS: Fig.1 shows that image C has a type of histogram with two peaks at grey levels of 50 and 225 and all other four images have another type of histogram with two sharp peaks only at grey levels of 0 and 255. Table 1 lists the imposed and calculated rotation angles, errors and average speckle size of five images. Mean errors are in a range of -0.031°~0.637° (-0.62%~ 12.73%) for all images. Image C has the least error of -0.003° (-0.05%) while its sharpened image C* has the

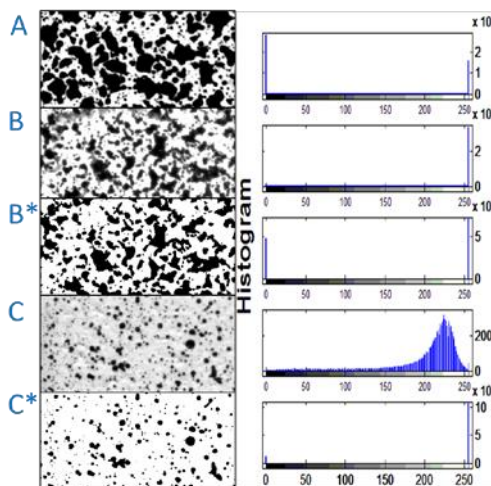largest error of 0.637° (12.73 %). Overall, the mean error of all images is in an order: C<B<A<B*<C*.

Fig. 1: Histograms and patterns A, B and C; B: sharpened B; C*: sharpened C.*

Table 1. Calculated rotation angles and errors.

Im.	Im p. θ	Calcul. θ	Mean error	Rel. error	Speck. size
A	5°	4.9688°	-0.031°	-0.62%	3.162
B	5°	4.9836°	-0.016°	-0.33%	3.184
B*	5°	5.0445°	0.044°	0.89%	3.184
C	5°	4.9973°	-0.003°	-0.05%	1.686
C*	5°	5.6367°	0.637°	12.73%	1.686

DISCUSSION & CONCLUSIONS: The calculated angles from DIC algorithm are all close to the real values. Overall, there are three key points concluded from this study: 1) Image C has the best pattern and histogram from accuracy point of view, 2) The sharpened images B* and C* have larger errors than their original unsharpened ones, B and C. This indicates that the sharpening process introduces error and 3) Speckle size of all images ranges in 1.6~20 pixels. Speckle C seems to have the smallest average size and the better grey value distribution leading to the smallest error.

Grey-level interpolation for image-resolution improvement and reconstruction at any desired sub-pixel position

J Zhang, G Baroud

Laboratoire de Biomécanique, Faculté de Génie, Université de Sherbrooke, Canada

INTRODUCTION: In the clinical diagnosis and surgeries, good visualization of objects is of rather importance for the success of subsequent treatments. Therefore, diversity of modern imaging techniques have been developed (*e.g.* X-ray, MRI, medical micro lens) and greatly facilitated the medical progress. However, on one hand, the resolution of medical images is limited by hardware, in many cases, cannot provide a good visualization. On the other hand, quantitatively monitoring pathological changes of objects often take place at sub-pixel level. To meet the growing accuracy requirements, processing methods (e.g. interpolation and subvoxelization) are applied to images to improve image resolution. Interpolation and subvoxelization are commonly used to calculate the grey level of those subpixels [1, 2]. These subpixels originally do not exist because of the discrete nature of digital images. Comparing the two methods, interpolation process can formulate a continuous function of grey level based on up to 16 neighbouring pixels (e.g. bicubic interpolation). Thus, the grey level of subpixels at any location can be obtained without running amounts of subvoxelization. In addition, the continuous function can also prompt the displacement measurement of interesting object using Newton-Raphson iteration in image-based methods, *i.e.* Digital Image Correlation (DIC). This study aims at demonstrating firstly the image resolution improvement for visualization and secondly for deformation computation accuracy by two commonly used grey level interpolants.

METHODS: Step 1): the improvement in image resolution and visualization. A small image (*left* in Fig. 1) of size 21×21 pixels is cropped from an experimental speckle image. This image is then interpolated using bilinear and bicubic spline interpolants. Two images (*middle* and *right* in Fig.1) which have a size of 5 times larger (105×105 pixels) than the original image are generated. Then the features in resolution and visualization of these three images are compared. Step 2): the accuracy in DIC displacement measurement using two interpolants, bilinear and bicubic spline. In this step, the original image (*left* in Fig. 1) is artificially imposed with known displacements $(u_0 = 2, v_0 = 2)$ in x and y

directions to form the deformed image. Then two mentioned interpolants are used in the DIC algorithm to provide the continuous functions of grey level of subpixels. The original and deformed image is used as input and the accurate displacement (u, v) of deformed image at subpixel level is calculated. In total, N = 81 pixels are computed in terms of displacement (u, v). Mean errors between the originally imposed and the measured values are used to evaluate the accuracy of both interpolants.

RESULTS: Fig. 1 shows the fuzzy low resolution image, where the crescent shape feature is not easily recognizable. The interpolated images using bilinear (*middle* in Fig.1) and bicubic spline (*right* in Fig.1) interpolants have a significantly higher resolution with higher precision over the features.
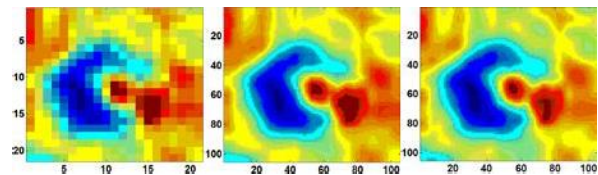

Fig. 1: Images before (left) and after bilinear (middle) and bicubic (right) interpolation.

Secondly, bilinear interpolation function resulted in errors of 2.12 % in u and 0.84 % in v from DIC algorithm. The bicubic interpolant resulted in errors of -0.05 % in u and -0.38 % in v using same setup.

DISCUSSION & CONCLUSIONS: Both of bilinear and bicubic interpolants had significant improvement in image visualization. Yet the bicubic spline interpolant produced a much smoother transition between original pixels and thus more valid. In displacement result, bicubic function had 2~40 times higher accuracy over bilinear one. The advantage of bicubic interpolant can be more remarkable in more complicated conditions yet on average it would have higher computation cost compared with the bilinear one.

Experimental characterization of mechanical properties of PMMA bone cement using three-element rectangular strain gauge rosette

J Zhang, G Baroud

Laboratoire de Biomécanique, Faculté de Génie, Université de Sherbrooke, Canada

INTRODUCTION: PMMA cement injection is a widely used procedure for treating vertebral fractures related to osteoporosis and pathological diseases. Yet adjacent fracture (new fractures at the vertebrae levels adjacent to the cemented one) is one of the most significant complications [1]. This complication is attributed to mechanical properties mismatches between injected PMMA and surrounding cancellous bone [2]. For example, Young's modulus (E) of cancellous bone is in the range of 20~500 MPa while that of PMMA is 4~160 times higher, ranging from 2 to 3.24GPa [2]. As a result, stress concentration and asynchronous deformation level of bone and cement induces adjacent fractures and cracks along the bone-cement interface [3]. Therefore, mechanical properties of PMMA cement should be improved to be closer to cancellous bone. Accurate characterization of PMMA properties is essential for improvements. However, in standard methods (*e.g.* ASTM/ISO), the strain is measured by dividing the elongation by the defined distance (D) between grips. This is neither a correct nor an accurate methodology since D consists of two different cross-section areas. Three-element strain gauge rosette is very precise instrument to provide accurate strain measurement for stress-strain characterization. Thus, this study focuses on mechanically characterize PMMA cement using rectangular three-element strain gauge rosette.

METHODS: Four standard PMMA (DP-Pour) specimens are fabricated according to the manufacturer's guidance with a dimension of 110×6×3 mm. Afterwards, two rectangular strain gauge rosettes (C2A-06-062WW-350, Micro-Measurements of VPG, USA) are bonded to each specimen. Each rosette is bonded on one side of specimen at the cross point of axial and transversal centerlines with the three elements exactly aligned (small graph on the right of Fig.2). Subsequently, the specimens are tested using MTS machine (858 Mini Bionix II) under axial tensile load according to ASTM-638. Bridge amplifier and Labview are used to collect the data from gauge rosettes. Labview recording is triggered by MTS loading starts signal. After tests, data are processed and gauge-resulted (GR) and ASTM standard-resulted (SR) principal strains, stress, young's modulus (E) and poison's ratio (ν) is obtained, respectively.

RESULTS: Fig.1 shows the GR axial and transversal principal strains versus time. The averaged GR ultimate strains axially and transversally of all specimens are 1.6 ± 0.26 % and -0.58 ± 0.12 %, respectively. Whereas, SR averaged axial ultimate strain is 1.3 ± 0.16 %. Fig. 2 shows the GR axial stress-strain. The GR averaged E and ν of four specimens are 3140.1 ± 532.4 MPa and 0.375 ± 0.032, respectively. Whereas, SR averaged E is 4377.4 ± 512.4 MPa.
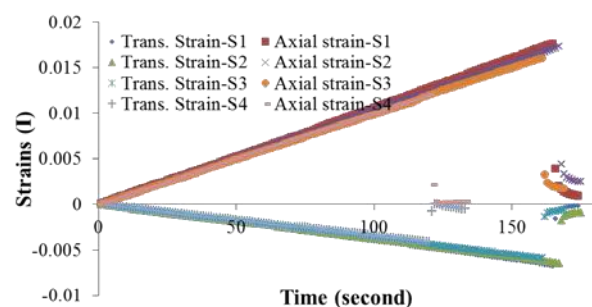

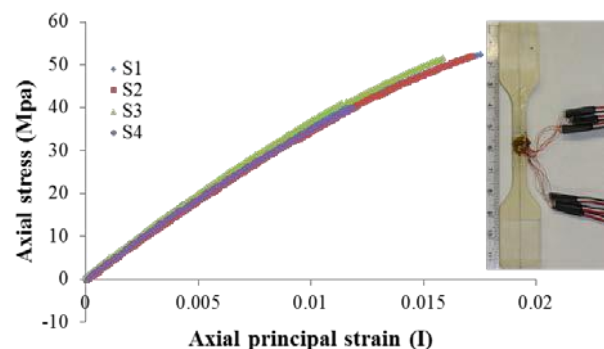*Fig. 1: The curve of axial-transversal strains (GR).*

Fig. 2: The curve of axially principal stress- strain.

DISCUSSION & CONCLUSIONS: High differences between the ASTM standard and gauge-based methods have been recorded. Specifically, the standard method produced on average 18.8 % less axial strain and 39.4 % more Young's modulus than gauge measurement. High attention should be paid to measurement methods accuracy in characterization of biomaterials.

The effect of subset size and number of pixels of interest on errors in the DIC measurement

J Zhang, G Baroud

Laboratoire de Biomécanique, Faculté de Génie, Université de Sherbrooke, Canada

INTRODUCTION: Several error sources are found to affect the DIC measurement. The subset size and number of calculated pixels of interest (POIs) are two important ones [1-2]. Proper selection of these two parameters can also help reduce the errors caused by improper image speckle pattern and noises. Thus, the accuracy of the DIC measurements can be increased by increasing the subset size. In the DIC measurements, a grid of POIs in input image is identified to track the deformation of the test object under the consideration of the computational cost. Moreover, a neighbourhood (subset) of each POI is selected for accurately identifying the POI in the deformed state. The identity information of a subset is proportional to its size. This abstract consists of two studies: investigations in the effect of the POI number and subset size on errors in DIC measurement.

METHODS: An experimental image of a tensile PMMA specimen (347×347 pixels, resolution = 17.3 micron) is used as reference image and its rotated version ($5°$) is used as the deformed image (Fig. 1). A region of interest (ROI) (the grid in Fig. 1) is then selected. Afterwards, for the study of POI numbers, four grid steps (GS, orange mark in Fig. 1) are selected; 2, 4, 6, 8 and 10 pixels. Correspondingly, 81, 121, 196, 441 and 1681 POIs (grid nodes in Fig. 1) are calculated (subset size is 41×41 pixels). For the study of subset size (green box in Fig. 1), seven groups (11×11 to 71×71 pixels with an increment of 10 pixels) are selected (121 POIs is calculated). The above two studies are separately performed. Mean and standard deviation (SD) errors in percentage of imposed rotation angle are calculated using the in-house DIC algorithm.
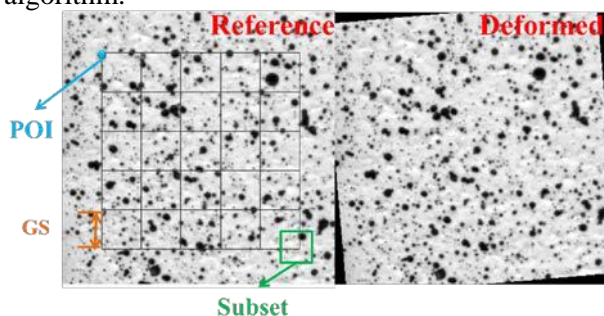

Fig. 1: Input images and studying parameters.

RESULTS: Fig. 2 and Fig. 3 show the mean and SD error bar between the real and DIC calculated rotation angles of two studies, respectively. Exact values are shown in the tables inside. The mean and SD errors in the study of POI numbers ranged from -0.108 % to -0.112 % and -0.141 % to -0.148 %, respectively. Meantime, mean and SD errors in the study of subset size ranged from -0.101 % to 2.36 % and 0.050 % to 48.25 %, respectively.
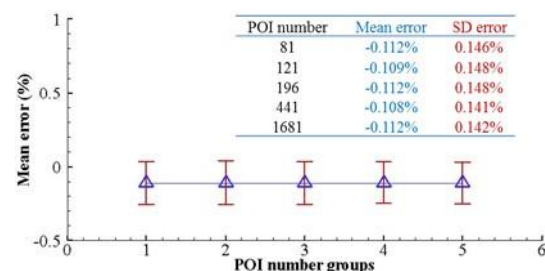

POI number	Mean error	SD error
81	-0.112%	0.146%
121	-0.109%	0.148%
196	-0.112%	0.148%
441	-0.108%	0.141%
1681	-0.112%	0.142%

Fig. 2: Errors in rotation angles vs. POI numbers.

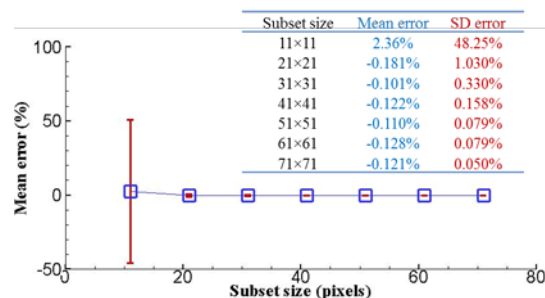| Subset size	Mean error	SD error
11×11	2.36%	48.25%
21×21	-0.181%	1.030%
31×31	-0.101%	0.330%
41×41	-0.122%	0.158%
51×51	-0.110%	0.079%
61×61	-0.128%	0.079%
71×71	-0.121%	0.050%

Fig. 3: Errors in rotation angle vs. subset sizes.

DISCUSSION & CONCLUSIONS: The study of POI numbers indicated that mean and SD errors seem to be not affected significantly by the selected POI number groups. This may be because of the homogenous deformation imposed to the image. The study of subset size indicated that the mean and SD errors decreased as the subset size increased. Especially, the subset size of 11×11 pixels had the largest percentage of both errors comparing with the rotation angle imposed to the deformed image. However, no significant improvement happens to mean error when subset size is larger than 31×31 pixels and to both errors when subset size is larger than 51×51 pixels.

Comparison of two synthetic bone grafts in a rabbit posterolateral fusion model

JE Brunelle

BioStructures, LLC, Newport Beach, CA, USA.

INTRODUCTION: Although iliac crest autograft (ICBG) is the "gold standard" bone graft in spinal fusion procedures, its use has limitations. Synthetic materials have been touted as viable alternatives, but their efficacy as stand-alone replacements for ICBG remains uncertain. In attempt to impart bio-stimulative properties and enhance bone healing capacity, modifications to traditional calcium phosphate materials have been introduced (*e.g.* silicate-substitution, addition of bioglass). Further, these materials have also been combined with resorbable polymer carriers to improve surgical handling properties. This study compares the fusion performance of two synthetic bone grafts in a validated posterolateral spine fusion (PLF) rabbit model [1]: Signafuse® Bioactive Putty, comprising biphasic HA/βTCP granules and 45S5 bioactive glass suspended in an alkylene oxide polymer carrier; and Actifuse® ABX, comprising silicate-substituted-HA granules suspended in an alkylene oxide copolymer carrier.

METHODS: Two test groups of 17 rabbits each had uninstrumented, bilateral intertransverse fusion at L5-L6 treated with either Signafuse or Actifuse. Bone remodeling and fusion status were assessed at 6 and 12 weeks using radiographic, histological and biomechanical endpoints.

RESULTS: MicroCT and histomorphometric analyses (sagittal plane) showed greater new bone formation ($p < 0.05$) with Signafuse at 6 weeks. Histological evaluation of the Signafuse treatment group revealed a progressive remodeling response characterized primarily by the formation of mature structural bone and marrow spaces bridging across the fusion bed from 6 to 12 weeks (Figure 1). The bioactive glass was largely replaced with new host bone (NB), and the apparent loss of distinction at the HA/βTCP granule interface indicates a normal, continuous resorption process (Figure 2). The Actifuse group revealed increased new bone formation over time, characterized by a mixture of woven and mature bone distending from the transverse processes (TP), with limited remodeling at the granule interface. Biomechanical fusion via flexion-extension motion data ($<5°$ ROM = fused) revealed an 80% fusion rate (8/10 rabbits) for Signafuse versus 44% (4/9) for Actifuse [1].
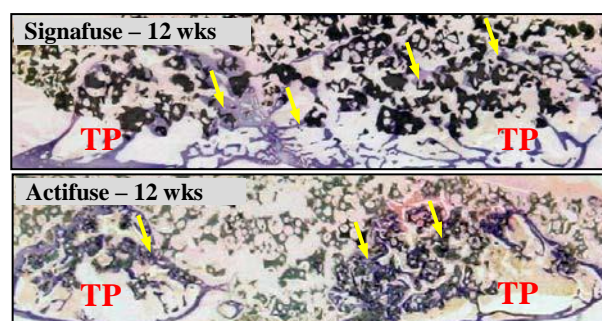

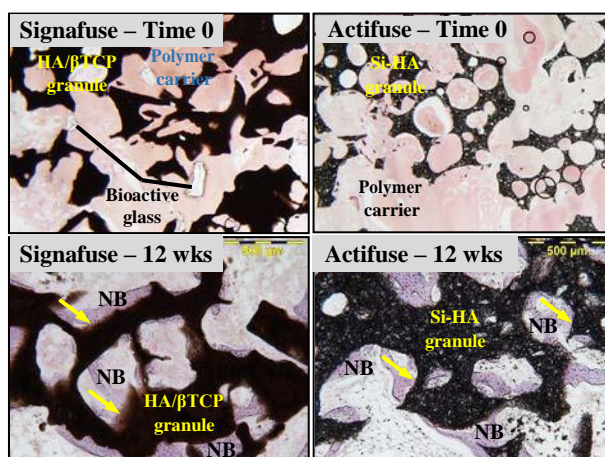*Fig. 1: Typical histology at 12 weeks (1X) showing a bridged fusion bed with Signafuse (arrows).*

Fig. 2: Histology of the test groups at time 0 (1.25X) and 12 weeks (5X). Remodeling (NB) appears more prominent with HA/βTCP (arrows).

DISCUSSION & CONCLUSIONS: Signafuse demonstrated greater capacity for successful spinal fusion remodeling compared to Actifuse ABX in a validated PLF animal model. The enhanced response of Signafuse is likely due to the biostimulative properties of 45S5 bioactive glass combined with the gradual resorption profile of the HA/βTCP granules, in contrast to the silicate-substituted HA material of Actifuse ABX [2,3].
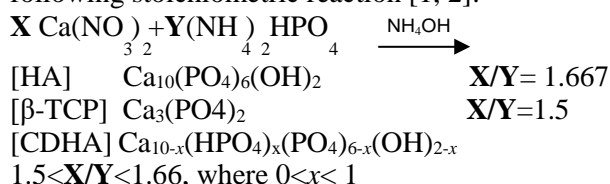
Correlation between stoichiometry and pH in the wet-chemical synthesis of calcium orthophosphates

M Habib[1], K Hussein[1], G Baroud[2], N Fatahalla[1]

[1]*Mechanical Engineering Department, Al-Azhar University, Cairo, Egypt.* [2]*Laboratoire de Biomécanique, Université de Sherbrooke, Canada.*

INTRODUCTION: Wet process is normally used for the synthesis of HA, β-TCP or biphasic calcium-phosphate ceramics HA/TCP through the following stoichiometric reaction [1, 2]:

$$\mathbf{X}\ Ca(NO_3)_2 + \mathbf{Y}(NH_4)_2 HPO_4 \xrightarrow{NH_4OH}$$

[HA] $Ca_{10}(PO_4)_6(OH)_2$ **X/Y**= 1.667
[β-TCP] $Ca_3(PO4)_2$ **X/Y**=1.5
[CDHA] $Ca_{10-x}(HPO_4)_x(PO_4)_{6-x}(OH)_{2-x}$
$1.5 < \mathbf{X/Y} < 1.66$, where $0 < x < 1$

However, the wet process was reported to be less reproducible on fabrication of pure apatitic TCP in comparison to other synthesis processes [2]. In this study, it is hypothesised that a specific apatitic phase that is normally obtained from stoichometirc reaction can be synthesised by using non-stoichometric based reactants in a reproducible way by controlling the pH value during the synthesis process.

METHODS: $(NH_4)_2HPO_4$ (Sigma Aldrich, Germany) and $Ca(NO_3)_2$ (Sigma Aldrich, India), as a starting reactants, were used to produce different calcium-phosphate phases. The chemical reaction took place between calcium and phosphorus ions under controlled temperature (80˚C), stirring time (2 h) and speed (1450 rpm). The alkalinity of the reaction was controlled by adding NH_4OH (EDWIC, Egypt). A factorial design with two factors, three levels and three repeats was implemented [A: Ca/P (1.5, 1.55, and 1.667) and B: pH (7.5, 8.5, and 9.5)]. All precipitated powders were dried and aged overnight and then sintered for 2 hours at 800 °C. The powders were analysed for phase, group and elemental analysis by X-Ray Diffraction (XRD), FTIR, and EDS, respectively.

RESULTS: HA was synthesized at room temperature, without sintering, from the sotichometric reaction (Ca/P=1.667) at a controlled pH of 9.5. Sintering increased the HA crystal size from 27.28 ± 14.54 nm to 73.35 ± 10.11 nm. β-TCP is synthesized stoichiometrically (**X/Y**=1.5) and from non-stoichometric based reactants (**X/Y**=1.55) at pH of 7.5 (Fig.1). Biphasic Ca/P with 65% HA and 35% β-TCP can be produced from stoichometric (**X/Y**=1.55). Biphasic 45% HA and 55% β-TCP from non-stoichometric (X/Y=1.5) based reactants at a controlled pH of 9.5

(Fig.2). FTIR shows that apatitic phase is formed with the observed fundamental vibrational modes of PO_4 group at 574 and 1020-1120 cm^{-1}. No impurities were detected in the EDS elemental analysis (Fig. 1).
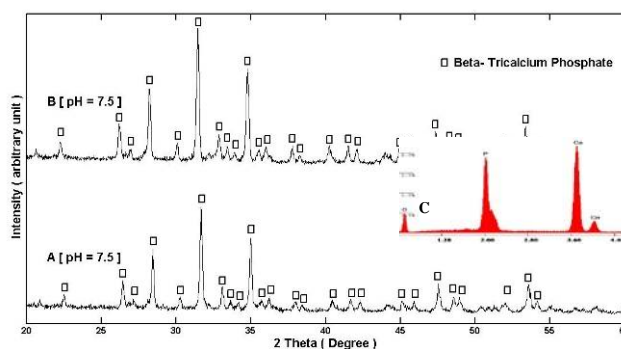

Fig. 1 XRD of pure β-TCP using A) 1.5, B) 1.55 Ca/P molar ratio and C) EDS elemental analysis
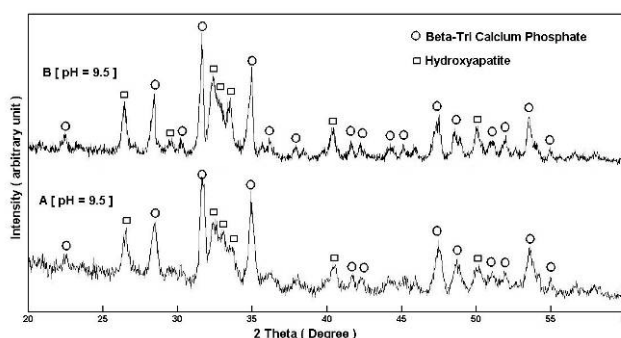

Fig. 2 XRD of biphasic Ca/P using A) 1.5 & B) 1.55 Ca/P molar ratio

DISCUSSION & CONCLUSIONS: The combined effect of both the reactants Ca/P molar ratio and pH value was studied. Slight difference in the reactant molar ratio can affect the synthesised phases dramatically. However, this slight difference can be reduced by exactly controlling the pH value. Sintering temperature is important to control the crystal size and the phase percentage when biphasic Ca/P is anticipated.

Computational leakage model for the bone augmentation procedure

S Alenezi[1], F Benyahia[2], F Gitzhofer[1], S Elkoun[1], M Bohner[3], G Baroud[1]

[1]*Laboratoire de Biomécanique,* Université de Sherbrooke*, Canada.* [2] *King Saud University, Kingdom of Saudi Arabia.* [3]*RMS Foundation, Switzerland.*

INTRODUCTION: Medical cements, such as Polymethylmethacrylate (PMMA), are used to augment weakened (*i.e.* osteoporotic) bones and reestablish the mechanical strength once hardened in-situ. In spite of the benefits of bone augmentation, the cement leakage is a serious event that can cause pulmonary embolism and spinal cord compression [1-3]. Thus, it is vital to study the leakage phenomenon and related physical and geometric interactions. Experimental leakage models have been reported in the literature [1]. Nevertheless, a well-defined computational leakage model is highly required to efficiently study the complex physical and geometrical interactions of the cement flow. This model can be used to examine the relevance of the viscous versus the elastic properties to the filling pattern. Thus, the objective is to present the first computational leakage model for bone augmentation.

METHODS: ANSYS-Polyflow was used to create a 2D computational leakage model that simulates the PMMA infiltration inside the osteoporotic bone with a leakage path. The 2D planar model was implemented with representative geometrical and physical parameters [1, 4]. The cement flows from the inlet of the model (representing an 8 gauge cannula), through a porous domain toward the outlet side (bottom side) (Fig.1). A representative porous domain was designed as a set of circular obstacles spaced-apart representing a converging and diverging flow in the trabecular bone. These obstacles are distributed in a regular pattern with specific porosity of 90% and permeability of $1.4 \times 10^{-8} m^2$ [5]. Inside the porous media a 3-mm channel was created in the flow direction to simulate a path of least resistance to trigger the cement leakage. The FE mesh was refined between the obstacles to control the accuracy of the solution while keeping a minimum computational time. The 15mm x 15mm porous domain was meshed with 124200 elements. The model requires two sets of boundary conditions covering the fluid flow and the volume of fraction (VOF) solver tracking the evolution of the front surface of the fluid. Consequently, three different boundary conditions are created; 1) "inlet" at entrance with a constant flow rate of $1mm^3/s$, 2) "outlet" at output with no external resistance and 3) "walls" with zero

velocity assigned to the rest of domain borders and the obstacle surfaces. The cement was modeled by Maxwell viscoelastic model (Eq.1)

$$\boldsymbol{T}_1 + \lambda \overset{\triangledown}{\boldsymbol{T}_1} = 2\eta \boldsymbol{D} \qquad (1)$$

Where T_1 is the stress tensor, λ is the relaxation time, $\overset{\triangledown}{T_1}$ is the upper-convected time derivative of T_1, η is the viscosity and D is the deformation rate tensor. The material behavior is governed by the two parameters λ and η determined using an oscillatory rheometer. Two experimental levels, low (L) and high (H), of the rheological properties λ (0.01 and 1.3s) and η (10 and 1000Pa·s) were considered in this study. The factorial levels were used to evaluate the effect of λ and η on the flow and pressure profile evolution.

RESULTS: Fig.1 shows the cement flow and pressure profiles for different sets of λ and η values after 30s. High λ results in a considerable reduction of the leakage (27% less penetration into the leakage path). In opposition to high λ values, high η increase considerably the augmentation pressure.
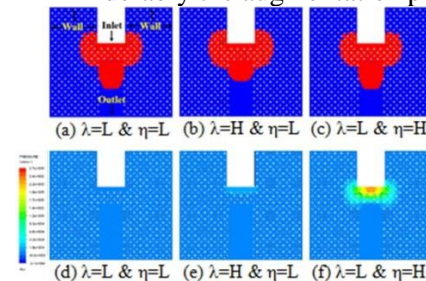

Fig. 1: Flow and pressure profiles of PMMA.

DISCUSSION & CONCLUSIONS: The cement with high λ uniformly distributes around the tip of the cannula with two potential advantages: low pressure and reduced leaks. Contrarily, increasing the viscosity η increases the delivery pressure drastically, yet the cement profile stays unchanged. In conclusion, the cement elastic behavior plays an important role in extrusion uniformity, control of delivery pressure and increase of leakage safety.

Fuzzy distance transform (FDT) versus distance transform (DT) applied to different range of pore sizes

S Jerban[1], A Sweedy[1], G Baroud[1], M Bohner[2]

[1]*Laboratoire de Biomécanique, Université de* Sherbrooke*, Canada.* [2]*RMS Foundation, Switzerland*

INTRODUCTION: Pore sizes in bone grafts (BGs) are crucial parameters promoting bone repair process. The μCT images are used commonly to characterize the microstructure of BGs. To calculate the pore sizes of BGs, the widely used distance transform algorithm (DT) is applied to segmented μCT images [1]. Specifically, DT algorithm calculates the Euclidean distance of each voxel within pores to the background, i.e. material phase. Consequently, the size of each pore is determined as twice the maximum DT value [1]. Due to the μCT nature, a fuzzy transition region is always observed in void/material interfaces (Fig. 1a). Physically, the voxels in fuzzy region partially belongs to pores even though they are not considered by DT algorithm (Fig. 1b). In last decade, fuzzy distance transform (FDT) was developed to improve the calculated sizes by coupling the Euclidean distance with fuzzy logic [2-3]. Specifically, before calculating the Euclidean distance, a fuzzy membership value (from 0 to 1) is assigned to each voxel depending on its void volume fraction. In earlier studies, FDT was presented as more accurate approach versus DT [2-3] even though the FDT is always slower and computationally more demanding. This study focuses on determining the improvements by FDT in pore size calculations compared with DT.

METHODS: Synthetic 2D and 3D images were used to compare FDT and DT. In 2D synthetic images (Fig. 1), a set of circular pores were defined with different diameter/pixel size ratios (DPRs) varied from 5 to 22. Then, the μCT scanning were simulated by assigning a gray level to each pixel depending on its pore volume fraction. Thereafter, the algorithms of both DT [4] and FDT [3] were traced manually to calculate the pore sizes by finding the maximum distance values in pores. In 3D synthetic images, a set of spherical pores were defined and subsequently scanned artificially with different diameter/voxel size ratios (DVRs) varied from 5 to 100. Then, Matlab software and an in-house code [1-2] were used to calculate the DT and FDT maps, respectively. Finally, the calculated pore sizes by FDT and DT were compared with defined sizes to estimate the errors.

RESULTS: Fig. 1 shows the FDT and DT maps of defined 2D circular pores (dashed red line). For DPR=10 the FDT produced higher maximum value (Fig. 1). The errors in pore sizes are shown in Fig. 2 for 2D and 3D synthetic images. For DVRs≤30, FDT was more accurate compared with DT. For 30<DVRs<50, the FDT and DT resulted in similar pore sizes. For 50<DVRs, DT was found more accurate.
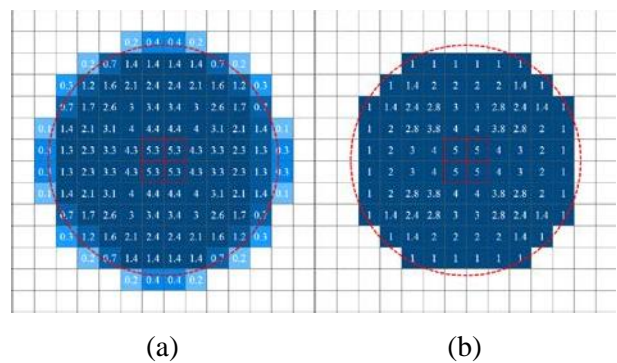

(a)   (b)

Fig. 1: (a) FDT and (b) DT of defined circular pore for DPR≈10.
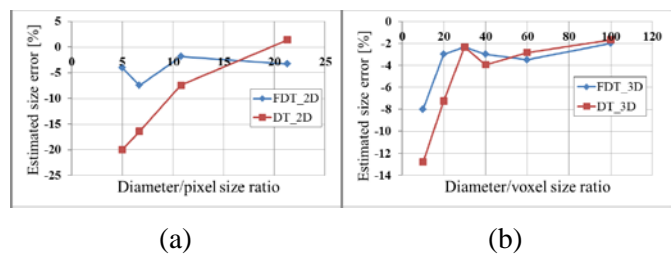

(a)   (b)

Fig. 2: Pore size errors by FDT versus DT in synthetic (a) 2D pores and (b) 3D pores.

DISCUSSION & CONCLUSIONS: The decision to use the FDT or DT in pore size calculation should be based on the mean DVR in BGs. For low DVRs (<20), the FDT is highly recommended and results in more accurate pore sizes compared with DT. Nevertheless, for high DVRs (>30) DT is recommended which is always faster and often more accurate.

Pore size sensitivity to gray level thresholding in the segmentation of µCT images

S Jerban[1], A Sweedy[1], G Baroud[1], M Bohner[2]

[1]Laboratoire de Biomécanique, Université de Sherbrooke, Canada. [2]RMS Foundation, Switzerland

INTRODUCTION: Pore diameter is a key geometrical parameter of bone substitute that correlates with bone repair rate. In µCT, average pore diameter to voxel size ratio (DVR) is an influential parameter on bone substitute microstructural characterizations. Low scanning DVR resulted in higher fraction of fuzzy transition regions on void/material interfaces [1]. In the last decade, Fuzzy distance transform (FDT) has been developed to improve the accuracy of feature size calculation in µCT data with relatively low DVRs [1-3]. In FDT, two initial thresholding values are chosen, one for void (Th_V) and one for material (Th_M). By using a fuzzification function (*i.e.* sigmoidal), a membership value ($0<\mu<1$) is assigned to each voxel with a gray level between the two thresholds. For example, the membership value of a voxel with a gray level equal to $(Th_V+Th_M)/2$ is assigned as 0.5 which means half of the voxel is occupied by material. This study examines the effects of the chosen gray level thresholding values on the pore size calculation.

METHODS: We used two groups of β-TCP scaffolds (C, 0.5 mm pores and D, 1 mm pores) in two different scanning resolutions which result in four sets of DVRs. In each set of scans, thresholding values (*e.g.* Th_V=40 and Th_M=110 in Fig. 1a) were chosen based on the gray level histograms and visual inspections of void/material interfaces. Then the thresholds were varied through the histograms in three patterns: 1) both thresholds moved toward the center of the histogram valley 2) Th_V was fixed and Th_M moved toward Th_V 3) Th_M was fixed and Th_V moved toward Th_M. Afterward, for each set of the chosen thresholds (60 sets), the pore size characterization was performed using Max-Min algorithm [1]. In Max-Min algorithm, the pore diameter is calculated as twice the maximum FDT.

RESULTS: Fig. 1a shows gray level histogram of scans with mean DVR close to 13. Fig.1b illustrates the differences between reconstructed pores by initial thresholding pair values, Th_V=40 and Th_M=110, and fully converged thresholding pair values (*i.e.* Th_V=75 and Th_M=75). Converging pattern of thresholding values in histogram resulted in reduced mean pore sizes (Fig. 1c) and

shifted size distributions to the left (Fig. 1d). Fig.1e and f show the sensitivity of pore size calculations to variation of Th_M and Th_V, respectively.
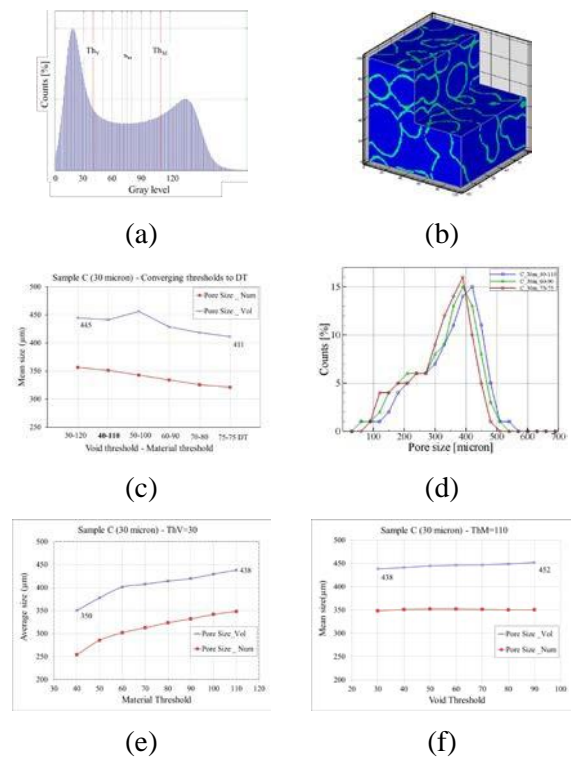

Fig. 1: (a) Gray level histogram. (b) Removed region via converging the thresholds. (c) Mean size and (d) size distributions of pores. Pore size sensitivity to variation of Th_M(e) and Th_V(f).

DISCUSSION & CONCLUSIONS: Groups with lower DVRs were found to be more sensitive to variations in thresholding values. Material thresholding value, *i.e.* Th_M, was found to be more determinative on size calculation in FDT approach. Specifically, pore size calculations exhibited higher sensitivity to variation of Th_M versus Th_V. It should be noted, to characterize the material phase of bone graft, Th_V would be more influential one.

Integrated segmentation of histology images to study the microstructural effect of bone substitutes on the biological responses

S Jerban[1], A Sweedy[1], L Galea[2], M Bohner[2], G Baroud[1]

[1]*Laboratoire de Biomécanique, Université de Sherbrooke, Canada.* [2]*RMS Foundation, Switzerland.*

INTRODUCTION: Resorbable bone substitutes (BS) promote the bone repair in critical size defects. Biological responses to BS, i.e. scaffold resorption and bone deposition, are assumed to be affected by BS microstructure. In earlier study, four Groups of cylindrical β-TCP scaffolds with different macro-porous structure (A, B, C and D), yet with similar porosities (25 % micro-porosity and 55 % macro-porosity) were implanted in sheep to study the biological response to the BS microstructure [1]. Specifically, the average macro-pore sizes were 150, 260, 510 and 1220 μm in Group A, B, C and D, respectively [1]. Histology images help distinguish different phases in the explanted BS. Yet, the histology coloring can render inaccurate results in particular for new growth in the micro-porous space. In this novel approach, we integrate the morphometric and mineralization data in the SEM images for accurate differentiation of tissue phases in the BS. In addition, we evaluate the biological response of the four Groups after 6 and 12 weeks of implantation.

METHODS: To accurately segment the histology images (toluidine blue staining, Fig. 1a), a color-based algorithm, that integrates the morphometric and mineralization information in SEM images (Fig. 1b SEM and Fig. 1c back-scattered SEM (BS-SEM)), was used. A human-assisted spatial registration was used to align the histology and SEM images. Using the blue-index (BI) and brightness of the histology images, and integrating both the geometric and mineralization information in the SEMs, five different phases in the explanted scaffolds are identified: (1) bone (high BI and dark in histology and dark in SEM), (2) BS remains (high BI and bright in histology and bright in both SEMs), (3) bosonic regions that have the highest mineralization (high BI and dark in histology and bright in SEM), (4) partially-resorbed BS (high BI and bright in histology, bright in SEM and dark in BS-SEM), and (5) soft tissue (low BI in histology). We segmented and analyzed the histology sections of explanted samples at 6 and 12 weeks (4.5 and 3 sections in average per group, respectively) [1]. Once segmented, the mean area fractions (AFs) were calculated in each group for 6 and 12 weeks.

RESULTS: Fig. 1a-d show histology, SEM, back-scattered SEM and the segmented images of a BS in Group A after 6 weeks of implantation. Fig. 1e-

h show the mean bone, bosonic region, BS remain and soft tissue AFs in all Groups, respectively.
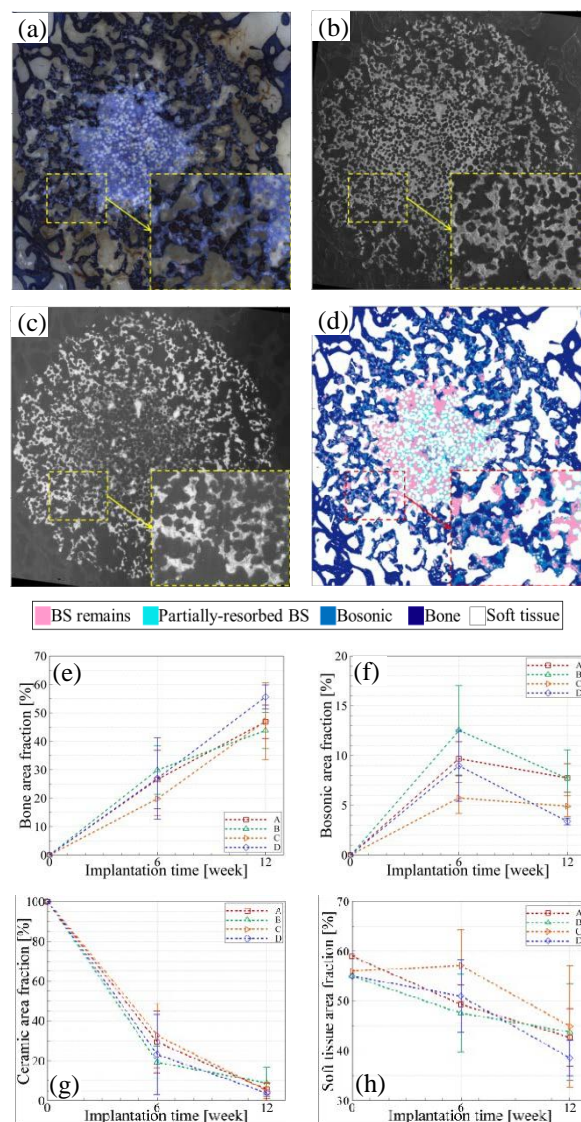

Fig.1: (a) histology, (b) SEM, (c) BS-SEM and (d) segmented images; (e), (f), (g) and (h) mean AF.

DISCUSSION & CONCLUSIONS: Integrating the SEM with histology images helped accurately segment phases in the explanted BS. Group B exhibited highest rate of bone deposition, bosonic phase formation as well as BS resorption in 6 weeks histology data. After 12 weeks, the mineralized bosonic regions reduced and are apparently remodeled into bone.

The effect of even/odd correction algorithm on porous space characterization

S Jerban[1], G Baroud[1], M Bohner[2]

[1]*Laboratoire de Biomécanique, Université de* Sherbrooke*, Canada.* [2]*RMS Foundation, Switzerland*

INTRODUCTION: The µCT scanning technique is commonly used to characterize the size of macro- and micro-pores in bone substitutes. Distance transform (DT) as an image processing algorithm is regularly used to determine the feature sizes in segmented µCT images. Theoretically, the size of any feature in scans equals twice the maximum DT value. Furthermore, the center points (CPs) of macro-pores are defined by coordinates of maxima in DT maps. However, the centerlines (CLs) in micro-pores (snake-like shape) are determined using the ridge points [1-2]. Nevertheless, the addressed theories encounter errors when they are applied to digital images. Finding the CPs or CLs requires odd number of voxels along the width of the features. However, odd number of voxels always results in one voxel overestimation error in size and thickness. For instance, CLs cannot be obtained in bars of two pixels thickness (Fig. 1a) whereas the thickness in bars of three pixels thickness is estimated by 4 (2×2) pixels (Fig. 1c). In previous studies [2-3], even/odd correction algorithm was developed by subvoxelizing the images leading to odd number of voxels in width of features [2-3]. This algorithm results in accurate determination of CPs and CLs (Fig. 1b and d). This study examines the even/odd correction algorithm and highlights its limitations encountering practical geometries in porous space.

METHODS: The even/odd correction algorithm was applied to the segmented images before DT algorithm. For simplicity, this 3D algorithm is described in 2D space as follows by mapping initial gray level image G(x,y) to the corrected one, $G_1(x,y)$:

i. For all pixels of G; $G_1(2i+1, 2j+1)$ is set equal to G(i,j). These pixels are primary points.
ii. For all non-primary points of G_1, $G_1(i_1,j_1)$ is set equal to 0 if $G_1(i_1,j_1)$ is adjacent to a primary non-object point; otherwise, is set equal to mean value of adjacent primary object points.

The developed algorithm was applied first to a synthetic 2D image that contains two connected objects with a neck between them (Fig. 1e). Thereafter, the surface fraction and geometries of corrected objects were compared with original ones. Secondly, the algorithm was applied to a set of synthetic 3D images including two scaffolds, i.e. scaffold I and II that comprised of 700 and 1700 pores, respectively. Subsequently, the porosity is used for comparison between corrected scaffolds and original ones.

RESULTS: Fig.1f shows the determined CL in synthetic 2D image. The object geometries in corrected 2D image were distorted and the surface fraction was decreased from 41 to 31 %. In corrected 3D images, porosity of both scaffolds was decreased however scaffold II experienced higher variation in porosity (Table.1).
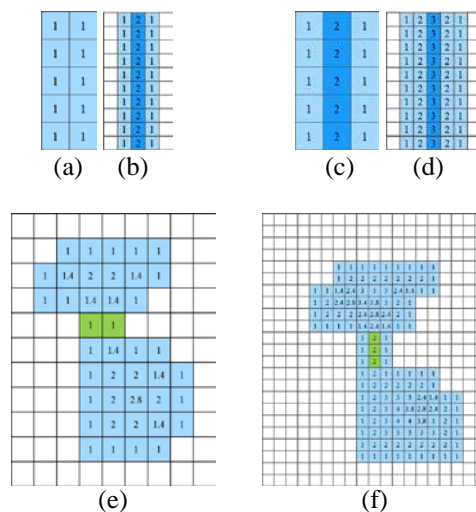

Fig. 1: Even/odd correction in bars of (a, b) two and (c, d) three pixels thickness. (e) Synthetic 2D image and (f) its corresponding corrected image.

Table 1. Summarized characterization results

	Scaffold I	Scaffold II
Size of pores [voxel]	40	30
Initial porosity [%]	61.64	64.05
Final porosity [%]	58.21	59.68
Error [%]	3.43	4.37

DISCUSSION & CONCLUSIONS: The even/odd correction algorithm enables accurately determining CPs and CLs in porous space. Therefore, the pore and interconnection size calculation becomes more accurate. Contrarily, this algorithm results in volume underestimation error that is inversely proportional to average pore size or specific surface.

www.ecmconferences.org

Isolating connected pores of highly porous β-TCP scaffolds

S Jerban[1], G Baroud[1], M Bohner[2]

[1]Laboratoire de Biomécanique, Université de Sherbrooke, Canada. [2]RMS Foundation, Switzerland

INTRODUCTION: Highly porous bone substitutes (BSs) are usually used for enhancing bone repair process in critical defects. Accurate characterization of void space in BSs is a key part in better understanding the biological responses. However, the complex geometries of connected pores arise as a challenge to accurately characterizing void space parameters, i.e. pore and interconnection sizes. Thus, isolating connected pores before size calculations was suggested yet not sufficiently described [1-3] to improve the characterization accuracy. Over-segmentation (OS) error was always the most common error in pores isolating process in highly porous BSs. Basically, to isolate each pore from the rest of void space, only one marker within the pore is required. Therefore, any extra marker in pores, i.e. idle marker, results in a new OS error. This study aims to develop an algorithm to avoid OS errors in isolating connected pores in two groups of highly porous β-TCP scaffolds [4]. Group I and II contain 1 and 0.5 mm pores, respectively.

METHODS: The algorithm comprises three complementary main steps; idle markers elimination, region growing [1-3] and merging algorithms. After calculating the FDT map of the void space, its local maxima are labeled exclusively as initial markers. Then, all markers are treated by idle markers elimination algorithm which excludes the redundant markers in pores (Fig. 2a). Specifically, excluded markers are the inscribable initial markers in virtual spheres of other markers with higher FDT values (Fig. 2a). In second step, one pore grows gradually from each correct marker which is labeled formerly (Fig. 1). Region growing algorithm is applied iteratively to voxels of each level of FDT maps descendingly from FDT_{Max} to 1. In each level of FDT maps, unlabeled voxels are added to formerly labeled markers if they are adjacent to only one label, otherwise they are labeled as connections (Fig. 1c). In third step, merging algorithm finds OS errors by examining and comparing the geometrical parameters of connected pores (Fig. 2c). Then in detected OS error, the voxels are relabeled to merge the two isolated regions. The developed algorithm was verified by inspecting

visually 10 % of 3D pores in central cubes of four scaffolds per group [4].

RESULTS: In the verification process, 11 OS errors were observed in 827 visually inspected pores (1.3 %). The average percentage of merged OS errors were 56 and 35 in group I (large pores) and II (small pores), respectively.
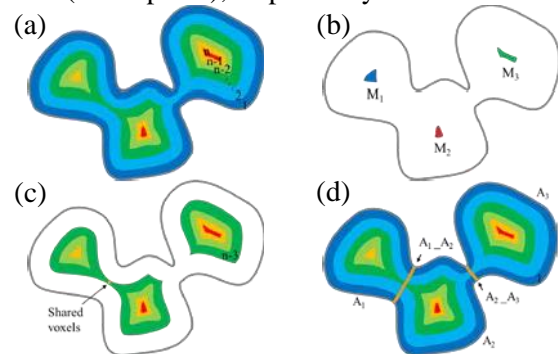

Fig. 1: Isolating process in schematic 2D pores. (a) FDT map. (b) Labelled markers. (c) Growing markers in 3rd FDT level (d) isolated pores & interconnections.
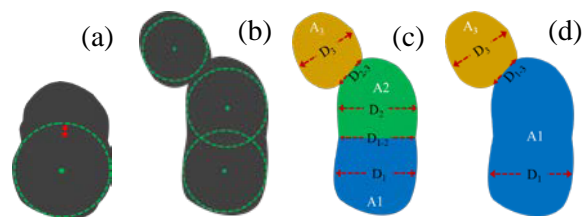

Fig. 2: (a) idle markers elimination process. (b) Right markers, (c) OS error in long pores and merging two pores in (d) one pore to solve OS.

DISCUSSION & CONCLUSIONS: This unique algorithm was found very accurate (>98 % accurate) as indicated by verification process. The merging algorithm was found as a crucial complementary step because the idle markers elimination step could not remove all redundant markers specifically in BSs with larger pores.
.

Error in interconnections of highly porous bone substitutes in low resolution µCT images

S Jerban[1], G Baroud[1], M Bohner[2]

[1]Laboratoire de Biomécanique, Université de Sherbrooke, Canada. [2]RMS Foundation, Switzerland

INTRODUCTION: Bone substitutes (BSs) were suggested to be highly porous to enhance the repair process in critical bone defects. In porous BSs, the interconnections are the most influential constraints encountering cells migration and blood vessels growth. Therefore, accurately characterizing the interconnections is a key part in understanding the interactions between BS microstructure and biological responses. High porosity, i.e. above 50 % is common in β-TCP scaffolds [1] which results in high number of interconnections and very thin separating walls. Micro tomography computed scanning (µCT) is used usually for BS microstructural characterization. However, the µCT is not capable to render the subvoxel walls between separated pores as well as the tip of convex void/material interfaces in interconnections (Fig. 1a and b). Specifically, in µCT images, the gray level of each voxel is determined proportional to its material volume fraction [2].Therefore, the µCT assigns low gray levels to the voxels that cover subvoxel walls or the tip of convex void/material interfaces (Fig. 1c and d). Consequently, the characterization process results in a wrong interconnection between mentioned separated pores (Fig. 1c). Moreover, all interconnection sizes are overestimated significantly (Fig. 1d). This study focuses on understanding the limitation of µCT scanning encountering interconnections and subvoxel separating walls.

METHODS: To study the wrong interconnection error, a set of synthetic spherical separated pores were used with different subvoxel wall thicknesses varied from 0.2 to 0.7 voxel (Fig. 1a). Similarly, to study the overestimation error of interconnection sizes, a set of synthetic spherical connected pores were used with different interconnection sizes. Specifically, the interconnection sizes are varied from 0.5 to 10 voxel. Afterward, the µCT scanning were simulated by assigning a gray level to each voxel depending on its pore volume fraction (Fig. 1a). The artificial scanning was done with different diameter/voxel ratios (DVRs), from 10 to 60. Finally, FDT [3] and isolating algorithms [4] were used to characterize the interconnection sizes.

RESULTS: The analyses show that a wrong interconnection will be revealed by µCT in the case of thin subvoxel walls (Fig. 2a). The thinner subvoxel walls ended in larger wrong interconnections. The size of wrong interconnections increased for higher DVRs in synthetic pores. Overestimation error in interconnection sizes was higher for smaller interconnections (Fig. 2b). The higher DVRs resulted in higher overestimation errors.
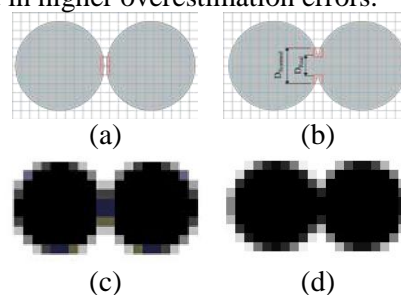

Fig. 1: Synthetic (a) separating subvoxel wall and (b) convex void/material interface. Artificially scanned (c) separated and (b) connected pores.
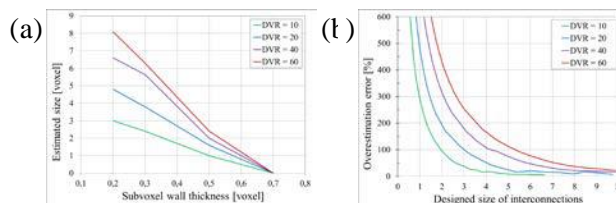

Fig. 2: (a) Estimated size of wrong connections. (b) Overestimation error of interconnections.

DISCUSSION & CONCLUSIONS: No matter what method is used to segment the scans of highly porous BSs, interconnection sizes and numbers are overestimated significantly. When resolutions increased, i.e. lower DVRs, the overestimations (number and size) were decreased. However, overestimation cannot be fully eliminated for the discrete nature of the scanning.

Accuracy of subvoxelization versus interpolation algorithms

S Jerban[1], J Zhang[1], A Sweedy[1], G Baroud[1], M Bohner[2]

[1]*Laboratoire de Biomécanique, Université de Sherbrooke, Canada.* [2]*RMS Foundation, Switzerland*

INTRODUCTION: Increasing image resolution after acquisition is commonly used to improve characterization accuracy. Several algorithms are applied in increasing image resolution such as subvoxelization [1-2] and interpolation [3]. In both algorithms, each voxel is divided into 8 subvoxels. In subvoxelization algorithm, a set of weighting values are calculated to reassign gray levels to the subvoxels. Subvoxelization is developed based on the conservation of average gray level within each original voxel. In interpolation algorithm, gray levels are calculated using a formerly chosen formula (*e.g.* bilinear and bicubic) regarding the application. Interpolation is developed based on the conservation of the original gray level in one of the subvoxels, i.e. primary subvoxel. The constants of the chosen formula are calculated in the non-primary subvoxels using the gray levels of the 6 closest primary subvoxels. This study examines and compares the effect of both algorithms on object size characterization.

METHODS: For simplicity, both algorithms are examined using a 2D synthetic ring shape object as an original image (Fig. 1a). In subvoxelization algorithm, the weighting value of each subpixel is assigned using the summation of the gray levels of the neighboring original pixels. Next, the gray level of each subpixel equals to the original gray level multiplied by the weighting value (Fig. 1b). Thereafter, a redistribution criterion is applied to subpixels if any subpixel value exceeds the maximum gray level, *i.e.* 255 [1-2]. The interpolation algorithm is comprised of the following steps. First, the original values are assigned to the primary subpixel in each original pixel (Fig. 1c). Second, the bilinear formula is chosen as given in *Eq.1* to calculate the gray level non-primary subpixels, G(x,y).

$$G(x, y) = a_{00} + a_{10}x' + a_{01}y' + a_{11}x'y' \quad (1)$$

Where x' and y' are distances from one of the primary subpixels and a_{00}, a_{10}, a_{01} and a_{11} are calculated using the gray levels of 4 closest primary subpixels.

RESULTS: Fig. 1d and e show the results obtained using subvoxelization and interpolation algorithms, respectively. In interpolation algorithm, new subpixels (red in Fig. 1e) are added to the border of the object, i.e. interpolation thickened the object. Whereas, the subvoxelization

algorithm resulted in zero gray level at the object corners (indicated in red, Fig. 1d). The calculated average thicknesses were 2.13 and 2.22 pixels after subvoxelization and interpolation, respectively.
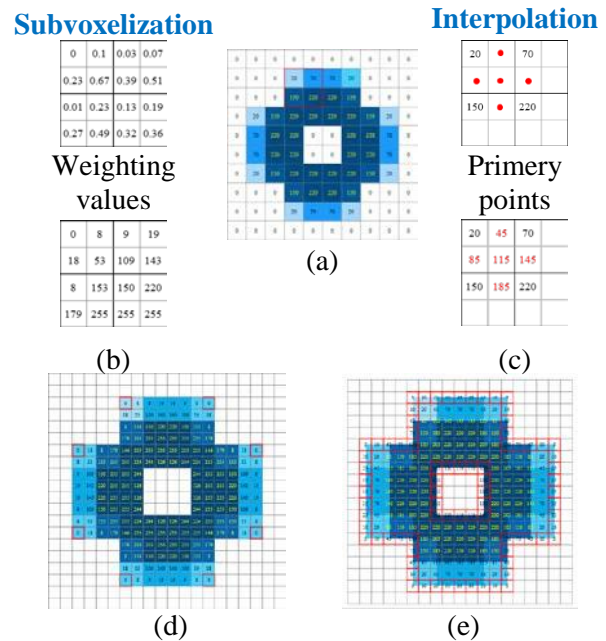

Fig. 1: (a) Original synthetic 2D object. (b) Subvoxelization and (c) interpolation steps in 4 original pixels (red in (a)). Gray levels of subpixels after (d) subvoxelization and (e) interpolation algorithms.

DISCUSSION & CONCLUSIONS: This study highlights the geometrical effects of subvoxelization and interpolation algorithms on object sizes. The interpolation resulted in thickened objects, *i.e.* 5 % higher average thickness compared with subvoxelized object. The thickening occurs by contaminating the background pixels on object border which is not physically reasonable. Therefore, the interpolation can be used for compensation of underestimation errors in size of objects with concave borders (*i.e.* pores and speckles). However, in characterizing objects with initial overestimation errors (*e.g.* interconnections) subvoxelization algorithm is a better choice to improve the accuracy.
.

Evaluation of step-of and volume of cavity during treatment of tibial plateau fracture by balloon and cement

T Vendeuvre[1, 2], F Maloubier[1], JR Richer[1], LE Gayet[2], C Brèque[1, 3]

[1] *Laboratory of Anatomy, Faculty of Medicine and Pharmacy, University of Poitiers, France.* [2] *Department of Orthopaedic Surgery and Traumatology, CHU of Poitiers, France.* [3] *P' institute, CNRS 3346, Futuroscope Chasseneuil, France*

INTRODUCTION: Tuberoplasty technique [1], for the treatment of tibial plateau fractures (Schatzker 2 type) uses a kyphoplasty balloon. Inflation of the balloon reduces the penetration of the tibial plateau fracture, whereas the conventional technique uses a bone tamp. The two techniques create a cavity within the tibia directly correlated [2] to bone regrowth time and a step-of the residual plate representing the quality of the reduction. We present a study allowing us to quantify the effects for each of these two techniques, as well as holding primary mechanical load mounting.

METHODS: With 12 tibial plateau from fresh cadaveric, we formed two groups. Each consisting of 3 men and 3 women (3 left / 3 right). The average age was 78.8 ± 6.2 years for the balloon group and 78.8 ± 5.4 years for bone tamp group. Each group underwent a simulated fracture experimentally Schatzker type 2 (compression and cleavage) and then reduced by a surgeon according to the respective technique, without cement. The 12 samples were scanned (section 0.67 mm) to obtain a 3D view, under Osirix®, of the cavity formed and of the step-of Figure 1 residual of the tibial plateau. The step-of is measured with the "length" function and the cavity with quantified functions "closed Polygon" and "repulsor" (fine determination of the contour). The charge held is obtained by compression of the tibia with a UKA knee arthroplasty and a compression machine. It is quantified by measuring the maximum force of compression admitted by each sample.

RESULTS: The step-of residual of the balloon technique is 2.9 mm (1st quartile 2.8 mm; 3rd quartile 2.9 mm), whereas for the bone tamp technique is 2.7 mm (1st quartile 3.3 mm; 3rd quartile 4.5 mm). The volume of the cavity formed by the balloon technique is 0.45 cm^3 (1st quartile 0.22 cm^3; 3rd quartile 0.74 cm^3), whereas for the bone tamp technique it's 5.12 cm^3 (1st quartile 4.98 cm^3; 3rd quartile 7.06 cm^3). Taking the two groups, we have established the relationship (Eq. 1) between the maximum compression load and the volume of the cavity, as shown thereafter:

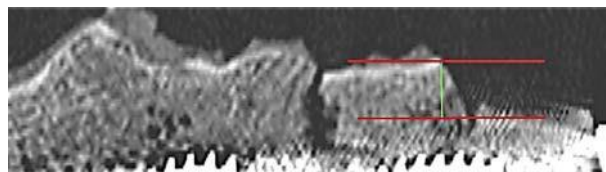$$F_{max} (N)= -114 *vol (cm^3)+1630 (R^2=0.62) \quad (1)$$
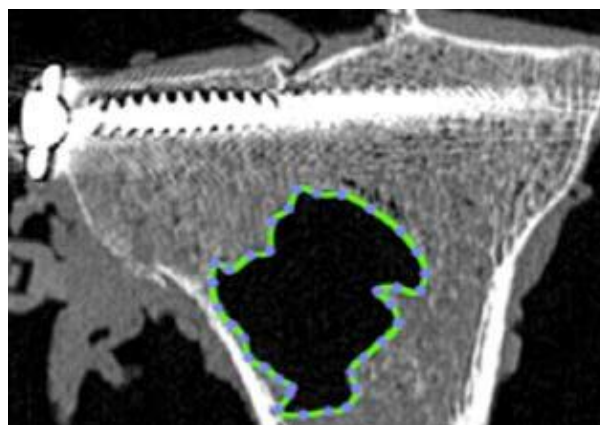

Fig. 1. Step-of residual plateau.

Fig. 2. Cavity formed by a bone tamp.

DISCUSSION & CONCLUSIONS: There is a difference between the two techniques for the volume of the cavity (p = 0.002), unlike the step-of (p = 0.06). Both techniques thus reduce the tibial plateau fracture in the same way, but the balloon's technique can reduce by 11.4 the size of the cavity. The thus injected cement volume is smaller, which may leave hope for a faster bone growth and a better mechanical strength, since we have proved the relationship between the cavity and the holding primary load.

Enhanced mechanical properties of a novel, injectable calcium polyphosphate-derived brushite bone cement

WP Ren[1,2], W Song[2], DC Markel[3]

[1] Wayne State University, Detroit, MI; [2] Virotech Biomaterials Inc., Detroit, MI; [3]Department of Orthopaedic, Providence Hospital, Southfield, MI, USA

INTRODUCTION: Commercially existing bone cements often lead to long-term graft failure due to weak mechanical strength, burst drug release and inadequate tissue-graft interactions. The present work aims to develop injectable calcium polyphosphate (CPP)-derived brushite bone cement with enhanced mechanical strength and the capability of sustained drug release.

METHODS: We developed and optimized the conditions for the preparation of CPP gels with stable viscoelasticity. CPP gel-based bone cement was prepared by reacting of CPP gel with alkali calcium source (such as tetracalcium phosphate (TTCP)). The end product of the reaction of TTCP with CPP gel is dibasic calcium phosphate dehydrate (DCPD, brushite).The advantages of CPP–derived brushite cements include constant viscosity, controllable setting, low curing temperature, slow degradation and sustained drug release.

RESULTS: Results from a longitudinal X-ray Diffraction (XRD) analysis confirmed a gradual transition from TTCP to DCPD in the presence of CPP gel (Fig.1). The % of DCPD conversion is ~90% at the time of 30 days, indicating the DCPD transition is slow and sustained. The DCPD conversion rate and velocity can be further manipulated by modifying preparation variables, such as the CPP/TTCP ratio, etc. CPP-derived brushite cements are injectable and printable. The most fascinating feature of CPP-derived brushite cements is the excellent mechanical strength. The compressive strength of CPP-derived brushite cements is in a range of 45-50 MPa. Table 1 shows a comparison of mechanical properties of CPP-derived brushite cements with Simplex® (PMMA cement) and Hydroset® (CPC cement) (all from Stryker). The results are highly reproducible and obtained using the same experimental conditions. Another unique advantage of CPP-derived brushite cements is its capability of sustained and controlled drug release. We measured in vitro release of FITC-albumin (0.2%) from CPP-derived brushite cements. The cumulative release of FITC-albumin lasted for > 4 months. The zero-order release of FITC-albumin is mainly due to the ionic interaction between water-soluble albumin and the polyphosphate backbone.

Table 1 Comparison of mechanical properties of CPP-brushite cement with Simplex ® and Hydroset® (n=5). σ_C = Compressive strength, E = Young's Modulus, P_F = Push-out force from bone

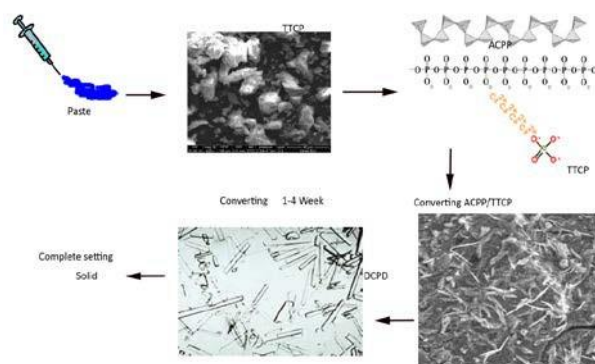|	σ_C (MPa)	E (MPa)	P_F (N)
Simplex® (PMMA)	65	730	1381
CPP-brushite cement	50	1283	930
Hydroset® (CPC)	18	442	511

Fig. 1: Transformation of DCPD by mixing of CPP and TTCP

DISCUSSION & CONCLUSIONS: CPP-derived brushite cements are mainly composed of CPP gel and TTCP and do not contain any supplementary cross-linkers and/or chemical compounds. In addition to easy handling (by simple mixing) and controllable in situ hardening, other advantages of CPP cements include cost reduction, bioactivity and safety. CPP-derived brushite cements can be used to repair both load-bearing and non-load-bearing bone defects because of its tuneable mechanical properties. CPP-derived brushite cements can also be used to repair damaged soft tissues.